ISSN 0914-9244
CODEN JSTEEW

Journal of Photopolymer Science and Technology

Volume 34 Number 4

2021

JOURNAL OF PHOTOPOLYMER SCIENCE AND TECHNOLOGY
Home Page http://www.spst-photopolymer.org
https://www.jstage.jst.go.jp/browse/photopolymer

Journal of Photopolymer Science and Technology publishes papers on the scientific progress and the technical development of photopolymers.

The Editorial Office
Assoc. Prof. Hiroyuki MAYAMA
Department of Chemistry, Asahikawa Medical University, 2-1-1-1 Midorigaoka-Higashi, Asahikawa, Hokkaido 078-8510, Japan.
FAX: +81-166-68-2782, e-mail: mayama@asahikawa-med.ac.jp

Information for Contributors

Submit Manuscripts to the SPST Homepage (Journal --> Submission of Papers --> Editorial Manager). Submission is a representation that the manuscript has not been published previously elsewhere. The manuscript should be accompanied by a statement transferring copyright from the authors (or their employers-whoever holds the copyright) to the Society of Photopolymer Science and Technology. A suitable form for copyright transfer is available from the SPST Homepage. This written transfer of copyright, which previously was assumed to be implicit in the act of submitting a manuscript, is necessary under the Japan copyright law. Further information may be obtained from the "Manual for Manuscript Writing" at the SPST Homepage.

Proofs and All Correspondence: Concerning papers in the process of publication should be addressed to the Editorial Office.

Manuscript Preparation: All the papers submitted are reproduced electronically as they were. For this reason, the manuscripts should be prepared according to the Manual for Manuscript Writings shown at the SPST Homepage.

Subscription Price (Airmail Postage included):
¥12,000 (in Japan), US$ 150.00 (for Foreign)

Subscriptions, renewals, and address changes should be addressed to the Editorial Office. For the address changes, please send both old and new addresses and, if possible, include a mailing label from the wrapper of recent issue. Requests from subscribers for missing journal issues will be honored without charge only if received within six months of the issue's actual date of publication; otherwise, the issue may be purchased at the single-copy price.

Publication Charge (Reprint Order): To support a part of the cost of publication of journal pages, the author's institution is requested to pay a page charge of ¥3,000 per page (with a one-page minimum) and an article charge of ¥12,000 per article. The page charge (if honored) entitles the author to 50 free reprints. For Errata the minimum page charge is ¥3,000, with no articles charge and no free reprints.

The cover designed by M. Tsuda and M. Morishita

JOURNAL OF PHOTOPOLYMER SCIENCE AND TECHNOLOGY

Volume 34 Number 4

2021

Published by

THE SOCIETY OF PHOTOPOLYMER SCIENCE AND TECHNOLOGY

THE SOCIETY OF PHOTOPOLYMER SCIENCE AND TECHNOLOGY (SPST)
http://www.spst-photopolymer.org

Office of the Administration
c/o Prof. Takashi KARATSU
Department of Applied Chemistry and Biotechnology,
Chiba University
1-33 Yayoicho, Inage-ku,
Chiba 263-8522, Japan
Phone: +81-43-290-3366
Fax +81-43-290-3401
e-mail:office@spst-photopolymer.org

THE SPST REPRESENTATIVES 2021

Communication

Journal of Photopolymer Science and Technology
Volume 34, Number 4 (2021) 329−334 ©2021SPST

Synthesis of Highly Ordered Si-Containing Fluorinated Block Copolymers

Jianuo Zhou, Xuemiao Li, and Hai Deng*

School of Micro-Electronics, State Key Laboratory of Molecular Engineering of Polymers
Fudan University, Shanghai 200433, China
**haideng@fudan.edu.cn*

Series of Si-containing, especially polyhedral oligomeric silsesquioxane (POSS)-containing fluorinated block copolymers (BCPs), poly(styryl polyhedral oligomeric silsesquioxane)-*block*-poly(hepatafluorobutyl methacrylate) (PStPOSS-*b*-PHFBMA) were synthesized via living polymerizations. The flory-huggins parameter (χ, at 150 ºC) of PStPOSS-*b*-PHFBMA BCP was 0.060. Highly ordered hexagonal domain with 13.2 nm *d*-spacing was observed by small-angle X-ray scattering (SAXS) after 10 h 160 ºC annealing, exhibiting rough line patterns in scanning electron microscope (SEM). $SiO_{1.5}$ residue (13.7 wt%) still remained after 700 ºC sintering in thermal gravimetric analysis (TGA).
Keywords: POSS BCP, Polyhedral oligomeric silsesquioxane, POSS, Fluorinated BCP, DSA, Hexagonal line, Organic-inorganic hybrid

1. Introduction

As a potential strategy for next-generation lithography technology (sub-10 nm), Directed Self-Assembly (DSA) with high resolution, has been attracting great attention from both academic and industrial fields. The most common materials used for DSA are block copolymers (BCPs) [1-6]. Extreme Ultraviolet lithography technology (EUVL) [7] has entered high-volume-manufacture (HVM) era with 13 nm half-pitch resolution, while patterning technologies for sub-10 nm resolution is still under defined.

Following the strategy of synthesizing BCPs with high flory-huggins parameter (χ), indicating high incompatibility between two blocks, and low degree of polymerization (*N*), various BCP systems with sub-10 nm domains were reported [8]. Our group recently reported several series of high χ fluorinated BCPs which can form 4-8 nm line-width pattern. Besides high resolution, the fluorinated block can drive BCPs to form cylindrical and lamellar line patterns at a very fast speed (~1 min) at rather low temperature (<100 ºC), showing great throughput advantage [9-17].

Besides high resolution and fast self-assembly speed, high etch contrast is also a key property for patterning materials. Si-containing BCPs, especially polyhedral oligomeric silsesquioxane (POSS)-containing BCPs, were widely studied, whose χ value ranged from 0.03 to 0.45 with max resolution of 4.4 nm [18] were reported [18-25].

In order to enhance the etch contrast for fast assembling fluorinated BCPs, high etch resistant metal-containing block and components were integrated into the BCPs [11,26]. In this study, Si-containing, especially POSS-containing BCPs, were synthesized and studied. Styryl-POSS-containing fluorinated BCPs, poly(styryl polyhedral oligomeric silsesquioxane)-*block*-poly(hepatafluorobutyl methacrylate) (PStPOSS-*b*-PHFBMA), and poly(trimethylsilylstyrene)-*block*-poly(pentadecafluorooctyl methacrylate) (PTMSS-*b*-PPDFMA) BCPs were synthesized via living polymerizations. Preliminary results of χ value and phase-separated patterns were reported in this paper.

2. Experimental

2.1. Synthesis and characterization

A newly-designed styryl polyhedral oligomeric silsesquioxane (StPOSS) monomer was used to synthesize PStPOSS-*b*-PHFBMA BCP via two-step reversible addition-fragmentation chain transfer (RAFT) polymerization. As a comparison, another Si- and F-containing BCP, PTMSS-b-PPDFMA,

Received March 31, 2021
Accepted April 30, 2021

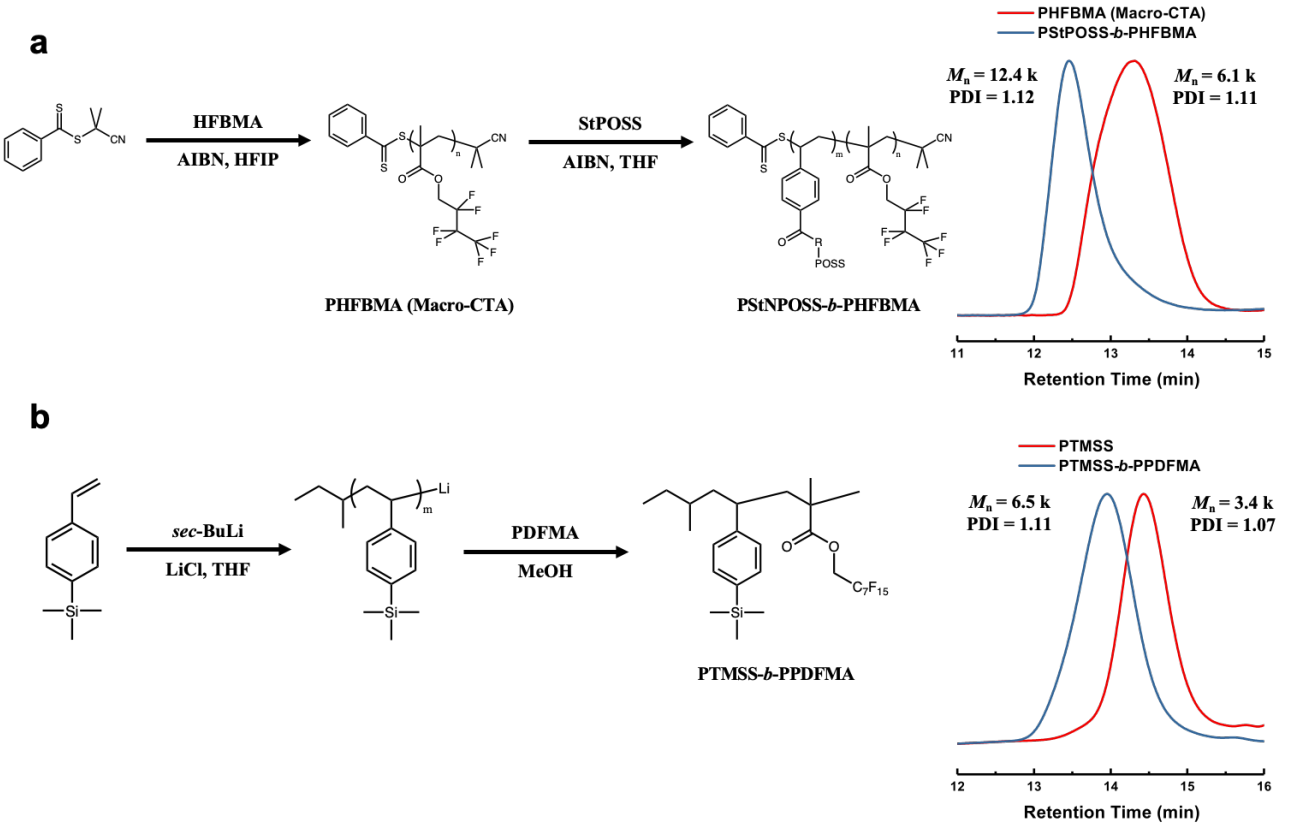

Fig. 1. Synthesis of (a) PStNPOSS-*b*-PHFBMA (M_n=12.4k, PDI=1.12) and (b) PTMSS-*b*-PPDFMA (M_n=6.5k, PDI=1.11) via living polymerizations, resulting in higher molecular weight BCPs with narrow polydispersity.

was also synthesized via living anionic polymerization. Trimethylsilylstyrene (TMSS) monomer was synthesized according to reported method [27]. All the other monomers and initiators were purchased from Energy Chemical or J&K and purified by neutral alumina column or recrystallization to remove inhibitors and impurities. Lithium chloride was obtained from Alfa Aesar. All the solvents (hexafluoroisopropanol (HFIP), tetrahyfrofuran (THF), methanol, propylene glycol monomethyl ether acetate (PGMEA)) were purchased from Titan and used as received.

All the synthesized BCPs were purified by dissolution three times and precipitation, followed by nuclear magnetic resonance (NMR) and gel permeation chromatograph (GPC) characterizations.

^{1}H NMR spectrums were recorded on a Bruker spectrometer (Advanced HD III) using $CDCl_3$ as a solvent with tetramethylsilane as an internal standard. GPC characterizations were conducted by an Agilent/Wyatt 1260 GPC eluting with THF (flow rate of 1 mL min^{-1}).

Differential scanning calorimetry (DSC) was performed on a TA Instruments Q2000. Measurements were taken from -20 ºC to 200 ºC at a heating rate of 10 ºC min^{-1} upon the second heating. Thermal gravimetric analysis (TGA) was performed on a PE Pyris 1 and measurements were taken under a nitrogen flow with a heating rate of 10 ºC min^{-1}.

The small-angle X-ray scattering (SAXS) diffraction patterns of powder polymer samples were collected on a Xenocs Xeuss 2.0 scattering system with a Pilatus 3R 200 K-A detector, which is equipped with Cu Kα radiation wavelength of 1.54 Å. Field-emission scanning electron microscopy (FESEM) images were acquired with a Zeiss Ultra 55 and a Zeiss Gemini SEM500 with an in-lens detector operated at 3 kV.

2.2. BCP bulk sample preparation

For SAXS characterizations, bulk sample of BCPs were prepared as following procedure. 0.5 mL 10 wt % BCP solution (in THF) was drop-cast on a clean Si wafer. After solvent evaporating and sample being dried in a vacuum oven, the resulted bulk samples were annealed on a hot plate at 160 ºC for 10 h and then quenched on a cold plate.

2.3. BCP thin film preparation

1.0 wt % solution of BCPs in PGMEA or THF was spin coated onto a Si wafer. After annealing

Table 1. Characterizations of PStPOSS-*b*-PHFBMA block copolymers

Sample	$M_{n,NMR}$ [a] (kg mol^{-1})	PDI [b]	DP_{StPOSS} [a]	DP_{HFBMA} [a]	Morphology [c]	*d*-spacing [d]	χ_{eff} [e]	χN [f]
S1	14.1	1.08	6.6	27	DIS	/	0.060 (150 ºC)	7.8
S2	14.6	1.07	6.3	30	DIS	/		8.1
S3	23.7	1.12	12.7	40	HEX	13.2		13.3

a) The molecular weights ($M_{n,NMR}$) and degrees of polymerization were calculated by ^{1}H NMR results. b) Polydispersity indexes (PDI) were measured by GPC in THF against PS standards. c) HEX represented hexagonal morphology, while DIS represented disordered structure was obtained after thermal annealing. d) *d*-Spacing represented the domain spacing of block copolymer and was calculated by the equation as $d = 2\pi/q^*$, while q^* was the value of the first order peak in SAXS.e) The effective χ value at certain temperature. f) *N* represented the overall degree of polymerization and was calculated by reference volume v_0 = 118 Å^3, based on the densities of PStPOSS and PHFBMA. The *N* values of S1-S3 were 130, 135 and 222, respectively.

process, reactive ion etching (RIE) was conducted in a plasma cleaner (Oxford Plasmalab System100) to enhance the image contrast between two blocks under FESEM measurement.

3. Results and discussion

3.1. Synthesis of PStPOSS-*b*-PHFBMA and PTMSS-*b*-PPDFMA BCPs

Styryl-POSS-containing fluorinated BCP, PStPOSS-*b*-PHFBMA, and PTMSS-*b*-PPDFMA BCP were synthesized via living polymerizations. The synthetic routes and GPC curves of PStPOSS-*b*-PHFBMA and PTMSS-*b*-PPDFMA were presented in Fig 1. The GPC curves completely shifted to higher molecular weight, indicating both Si-containing BCPs with PDI<1.12 were obtained.

Table 1 summarized molecular weight (M_n), χ value and morphology data. The M_n and degree of polymerization (DP) of PStPOSS-*b*-PHFBMA were measured by ^{1}H NMR. Resulted PStPOSS-*b*-PHFBMA BCPs have various M_n, ranged from 14.1 kg mol^{-1} to 23.7 kg mol^{-1}, with POSS block and fluorine methacrylate block, which also are so-called organic-inorganic hybrid material.

3.2 χ value characterization

Morphologies and domain spacings of PStPOSS-*b*-PHFBMA BCPs were determined by SAXS. All the BCP bulk samples were thermally annealed at 160 ºC for 10 h to achieve equilibrium microphase separation state. As shown in Table 1, S3 could form highly ordered 13.2 nm hexagonal domain after thermal annealing, while S1 and S2 obtained disordered structure.

The effective χ value at 150 ºC of PStPOSS-*b*-PHFBMA was calculated to be 0.060, higher than conventional PS-*b*-PMMA BCP (χ = 0.030, at 150 ºC) [28], but lower than reported POSS-containing BCPs [24]. The χN value of S1 and S2 BCP was lower than the critical value of χN = 10.5 [8], resulting that S1 and S2 could not obtain ordered structure.

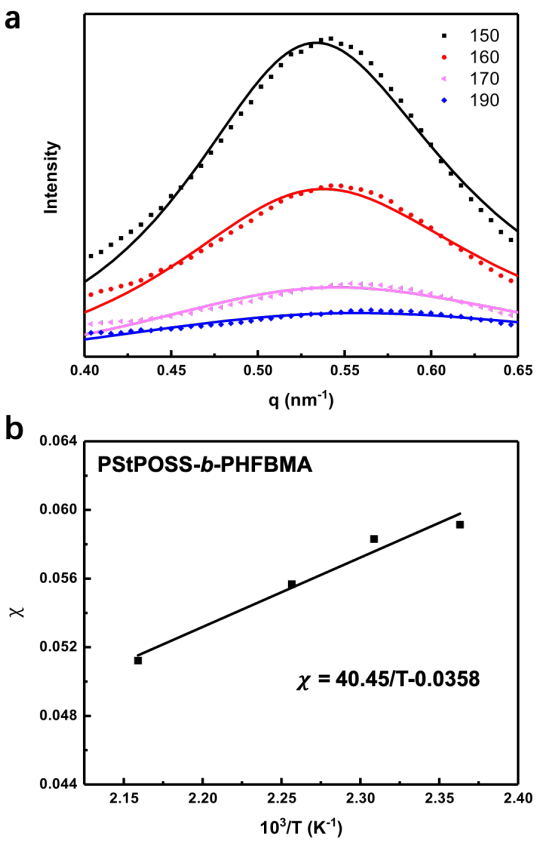

Fig. 2. (a) Fitlines of SAXS intensities of disordered PStPOSS-*b*-PHFBMA at various temperatures. (b) Temperature dependence of χ between PStPOSS block and PHFBMA block.

The χ value of PStPOSS-*b*-PHFBMA was estimated by Leibler's mean field theory using the random phase approximation of the absolute intensity from SAXS (Fig. 2a) [29-31]. Fully disordered BCPs were used to estimate χ values. The χ value of PStPOSS-*b*-PHFBMA BCP has a temperature dependence as χ = 40.45/T-0.0358 (Fig 2b).

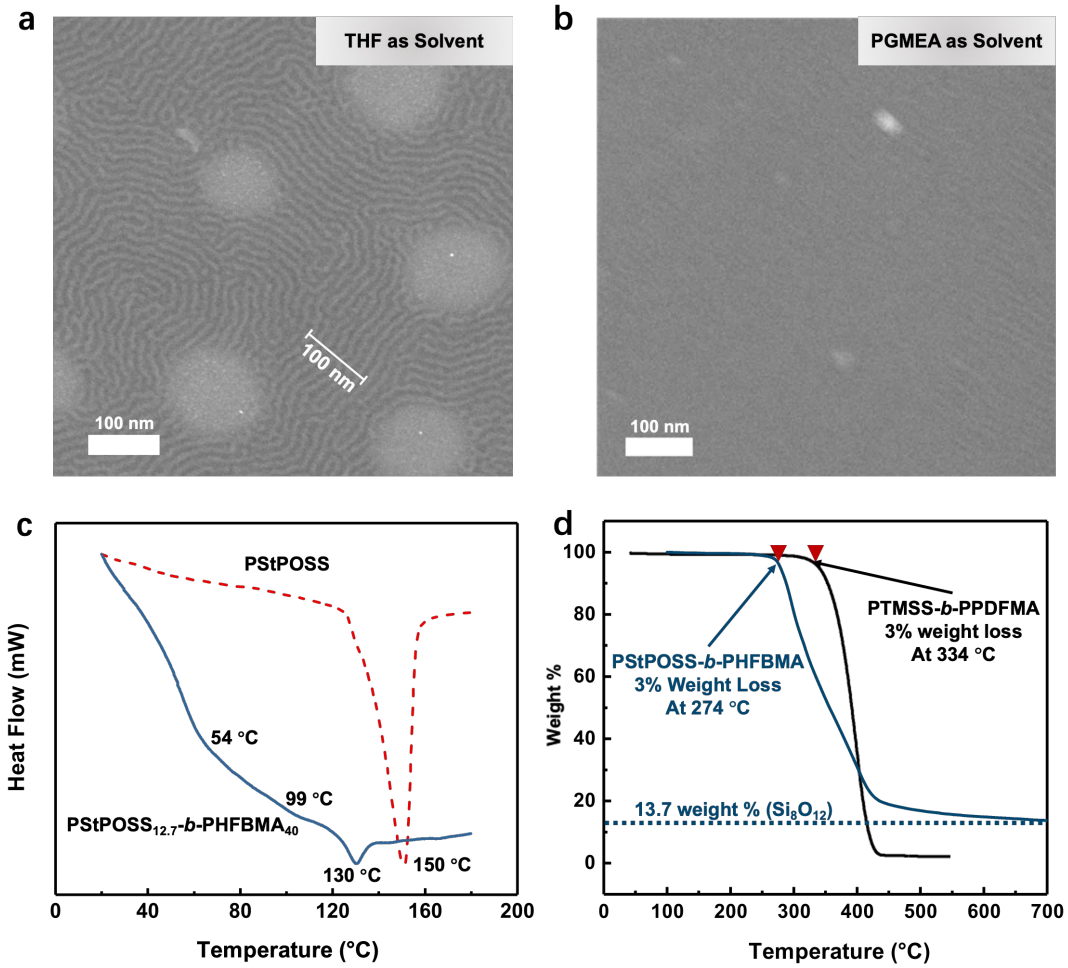

Fig. 3. The FESEM images of PStPOSS-*b*-PHFBMA (S3) thin film prepared by (a) THF and (b) PGMEA. The dark and bright lines correspond to PStNPOSS and PHFBMA microdomains, respectively. (c) DSC curves of PStPOSS-*b*-PHFBMA (T_g, 54 ºC and 99 ºC; T_m, 130 ºC) compared to PStPOSS (T_m, 150 ºC) homopolymer. (d) TGA curves of PStPOSS-*b*-PHFBMA (S3, T_d, 274 ºC) compared to PTMSS-*b*-PPDFMA (T_d, 334 ºC). Residue of PStPOSS-*b*-PHFBMA was 13.7 wt% at 700 ºC, versus 2 wt% of PTMSS-BCP at 430 ºC.

3.3 Phase separation in thin film

As well known, POSS monomer is crystallizable and can form crystalline domain when served as pendant group covalently linked to polymer backbone [32,33]. The nanostructure of PStPOSS-*b*-PHFBMA (S3) thin films prepared by various solvents, PGMEA and THF, were characterized by FESEM after CF_4 RIE treatment.

Distinct 7.7 nm line-pattern was observed in the thin film prepared by THF compared to thin film prepared by PGMEA (Fig. 3a-b). However, the line-pattern in THF-prepared thin film still had rather high roughness which might be caused by POSS crystalline.

3.4 Themal analysis of organic-inorganic hybrid BCP (PStPOSS-*b*-PHFBMA)

As the DSC curves presented in Fig. 3c, the T_m of PStPOSS homopolymer and PStPOSS-*b*-PHFBMA were 150 ºC and 130 ºC, respectively. The POSS crystalline could retard the polymer chain mobility [32,33], resulting in relatively rough line-pattern. PStPOSS-*b*-PHFBMA (S3) has two glass transition temperature (T_g), similar to previously reported PS-b-PPDFMA BCP [9]. The T_g at 54 ºC corresponded to PHFBMA, while T_g at 99 ºC was assigned to PStNPOSS block.

The thermal stability of PStPOSS-*b*-PHFBMA (S3) was further investigated by TGA comparing to PTMSS-*b*-PPDFMA (Fig. 3d). The decomposition temperatures (T_d) of PStPOSS-*b*-PHFBMA and PTMSS-*b*-PPDFMA were 274 ºC and 334 ºC, respectively. As PStPOSS-*b*-PHFBMA contained rigid inorganic POSS cage similar to SiO_2, the inorganic residue (13.7 wt%) of PStPOSS-*b*-PHFBMA was consistent with theoretical fraction of Si_8O_{12} (13.0 wt%) after 700 ºC sintering (Fig 3d),

indicating inorganic characteristics. Comparing to POSS BCPs, Si in PTMSS-*b*-PPDFMA almost vanished after heating up to 450 ºC, similar to normal organic compound.

4. Conclusion

Series of POSS-containing fluorinated BCPs, PStPOSS-*b*-PHFBMA, were synthesized via RAFT living polymerization. Resulted BCPs showed higher molecular weight compared to PHFBMA marco-CTA, and the polydispersity was lower than 1.15, which indicated PStPOSS-*b*-PHFBMA BCP was obtained. The effective χ value (150 ºC) of our BCPs is 0.060, lower than previously reported by others. Ordered hexagonal domain with 13.2 nm *d*-spacing was observed once $\chi N > 10.5$. The SEM image further confirmed the highly ordered line-pattern. Due to the POSS crystalline effect showed in DSC, the lines were quite rough. Benefit from the inorganic POSS cage, 13.7 wt% of PStPOSS-*b*-PHFBMA BCP still remained at 700 ºC, which is consistent with the theoretical inorganic composition of Si_8O_{12}.

Acknowledgement

This work was supported financially from the Shanghai Science and Technology Committee (18511104900) and Shanghai TD Advanced Material Technology Inc. (KCH1717170). The authors also acknowledge experimental support from the State Key Laboratory of Molecular Engineering of Polymers and the Nano-fabrication Laboratory of Fudan University.

References

1. R. Ruiz, H. Kang, F. A. Detcheverry, E. Dobisz, D. S. Kercher, T. R. Albrecht, J. J. de Pablo, and P. F. Nealey, *Science*, **321** (2008) 936.
2. M. Li, and C. K. Ober, *Materials Today*, **9** (2006) 30.
3. J. Bang, U. Jeong, D. Y. Ryu, T. P. Russell, and C. J. Hawker, *Adv. Mater.*, **21**(2009) 4769.
4. H.-C. Kim, S.-M. Park, and W. D. Hinsberg, *Chem. Rev.*, **110** (2010) 146.
5. C. M. Bates, M. J. Maher, D. W. Janes, C. J. Ellison, and C. G. Willson, *Macromolecules*, **47** (2014) 2.
6. C. M. Bates, and F. S. Bates, *Macromolecules*, **50** (2017) 3.
7. C. Wagner, and N. Harned, *Nat. Photonics*, **4** (2010) 24.
8. C. Sinturel, F. S. Bates and M. A. Hillmyer, *Acs Macro Lett.*, **4** (2015) 1044.
9. X. Li, J. Li, C. Wang, Y. Liu, and H. Deng, *J. Mater. Chem. C*, **7** (2019) 2535.
10. C. Wang, X. Li, and H. Deng, *ACS Macro Lett.*, **8** (2019) 368.
11. X. Li, and H. Deng, *Acs Appl. Polym. Mater.*, **2** (2020) 3601.
12. H. Cao, L. Dai, Y. Liu, X. Li, Z. Yang, and H. Deng, *Macromolecules*, **53** (2020) 8757.
13. H. Cao, X. Li, Y. Liu, and H. Deng, *J. Photopolym. Sci. Technol.*, **32** (2019) 413.
14. L. Dai, H. Cao, and H. Deng, *J. Photopolym. Sci. Technol.*, **33** (2020) 541.
15. H. Deng, X. Li, Y. Peng, and J. Zhou, *Proc. SPIE*, **10586** (2018) 105861E.
16. X. Li, Z. Li, L. Dai, H. Cao, and H. Deng, *Proc. SPIE*, 11326 (2020) 113261E.
17. H. Deng, X. Li, and J. Li, CN107245133B, US20180208697-A1, 2020.
18. Y. D. Luo, D. Montarnal, S. Kirn, W. C. Shi, K. P. Barteau, C. W. Pester, P. D. Hustad, M. D. Christianson, G. H. Fredrickson, E. J. Kramer, and C. J. Hawker, *Macromolecules*, **48** (2015) 3422.
19. K. Azuma, J. Sung, Y. Choo, Y. Rokhlenko, J. H. Dwyer, B. Schweitzer, T. Hayakawa, C. O. Osuji, and P. Gopalan, *Macromolecules*, **51** (2018) 6460.
20. K. Aissou, M. Mumtaz, G. Fleury, G. Portale, C. Navarro, E. Cloutet, C. Brochon, C. A. Ross, and G. Hadziioannou, *Adv. Mater.*, **27** (2015) 261.
21. W. J. Durand, G. Blachut, M. J. Maher, S. Sirard, S. Tein, M. C. Carlson, Y. Asano, S. X. Zhou, A. P. Lane, C. M. Bates, C. J. Ellison, and C. G. Willson, *J. Polym. Sci. Part a-Polym. Chem.*, **53** (2015) 344.
22. T. Hirai, M. Leolukman, T. Hayakawa, M.-A. Kakimoto, and P. Gopalan, *Macromolecules*, **41** (2008) 4558.
23. T. Hirai, M. Leolukman, C. C. Liu, E. Han, Y. J. Kim, Y. Ishida, T. Hayakawa, M.-A. Kakimoto, P. F. Nealey, and P. Gopalan, *Adv. Mater.*, **21** (2009) 4334.
24. R. Nakatani, H. Takano, A. Chandra, Y. Yoshimura, L. Wang, Y. Suzuki, Y. Tanaka, R. Maeda, N. Kihara, S. Minegishi, K. Miyagi, Y. Kasahara, H. Sato, Y. Seino, T. Azuma, H. Yokoyama, C. K. Ober, and T. Hayakawa, *ACS Appl. Mater. Interfaces*, **9** (2017) 31266.
25. T.-Y. Lo, M. R. Krishnan, K.-Y. Lu, and R.-M. Ho, *Progress in Polym. Sci.*, **77** (2018) 19.
26. G. Wu, and H. Deng, *J. Photopolym. Sci. Technol.*, **33** (2020) 537.
27. S. Langle, F. David-Quillot, A. Balland, M.

Abarbri, and A. Duchene, *J. Organomet. Chem.*, **671** (2003) 113.
28. T. P. Russell, R. P. Hjelm and P. A. Seeger, *Macromolecules*, **23** (1990) 890.
29. L. Leibler, *Macromolecules*, **13** (1980) 1602.
30. Y. Zhao, E. Sivaniah, and T. Hashimoto, *Macromolecules*, **41** (2008) 9948.
31. A. N. Semenov, *Macromolecules*, **26** (1993) 6617.
32. J. Waddon, L. Zheng, R. J. Farris, and E. B. Coughlin, *Nano Lett.*, **2** (2002) 1149.
33. A. Lee, and J. D. Lichtenhan, *Macromolecules*, **31** (1998) 4970.

Communication

Journal of Photopolymer Science and Technology
Volume 34, Number 4 (2021) 335−338 ©2021SPST

Synthesis of Ordered Fluorinated BCPs with One Block Composed of Random Copolymer

Min Cao and Hai Deng*

School of Micro-Electronics, State Key Laboratory of Molecular Engineering of Polymers
Fudan University, Shanghai 200433, China
**haideng@fudan.edu.cn*

A series of fluorinated block copolymers (BCPs), with one block composed of random vinyl copolymers were synthesized by reversible addition fragmentation chain-transfer (RAFT) polymerization. Despite of the hugely different properties of the two monomers in the random copolymer block, highly ordered lamellar structure with sub-10 nm resolution was observed by SAXS after 160 ºC annealing for 24 h. Each micro-domain consisted of two uniformly distributed monomers, with a low T_g down to 24 ºC.

Keywords: Random Copolymer, Fluorinated BCP, Low T_g, DSA

1. Introduction

As a potential candidate for sub-10 nm lithography technology, Directed Self-Assembly (DSA) with high resolution has attracted great attention from both academic and industrial fields. Block copolymers (BCPs) are the most common materials used for DSA [1-6]. Extreme Ultraviolet lithography technology (EUVL) [7] has entered high-volume-manufacture (HVM) era with 13 nm half-pitch resolution, while patterning technologies for sub-10 nm resolution is still under defined.

The most widely studied DSA material has been polystyrene-block-poly(methyl methacrylate) (PS-*b*-PMMA) [8-10], both of the two blocks show a high glass transition temperature (T_g), giving rise to plastic domains. Introducing rubbery block with low T_g into DSA material offers the possibility of thermal reflow to reduce the defect in the final pattern.

Our group recently reported several series of low-T_g fluorinated BCPs capable of forming 4-8 nm microdomains, in which fluorinated block can drive BCPs to form lamellar line patterns [11-20]. In these cases, both of the two blocks are composed of one monomer. In this study, two monomers (one was methacrylate monomer, the other was a totally different vinyl monomer) of hugely different properties were randomly incorporated into one block, with the other block maintaining fluorinated methacrylate. After thermal annealing, ordered lamellar structure with sub-10 nm domain size was obtained, demonstrating that fluorinated block can also drive the two-component random copolymer block to form ordered structures. Each micro-domain consisted of two uniformly distributed monomers, with a low T_g down to 24 ºC.

2. Experimental

2.1. Synthesis and characterization

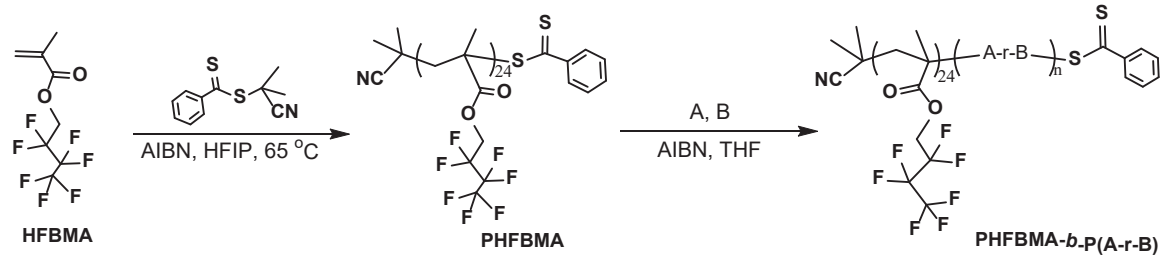

Fig. 1. Synthesis route of PHFBMA-*b*-P(A-r-B) by RAFT polymerization

Received April 1, 2021
Accepted May 3, 2021

Table 1. Characterizations of P(HFBMA)$_{24}$-*b*-P(A-r-B)$_n$ block copolymers

Sample	$M_{n,NMR}$ [a] (kg mol^{-1})	PDI [b]	A/B [a] in 2nd block	DP_{A-B} [a]	T_g [c] (°C)	Morphology [d]	*d*-spacing [e] (nm)
S1	14.3	1.16	81/19	20	24&45	LAM	13.0
S2	9.8	1.13	74/26	8	46	LAM	12.9
S3	8.6	1.09	76/24	5	51	DIS	/

a) The molecular weight ($M_{n, NMR}$) and degrees of polymerization (DP) were determined by ^{1}H NMR. b) Polydispersity indexes (PDI) were determined by GPC in THF against PS standards. c) LAM represented lamellar morphology and DIS represented disordered structure. d) *d*-Spacing represented the domain spacing of block copolymer and was calculated by the equation as $d = 2\pi/q^*$, while q^* was the value of the first order peak in SAXS.

The PHFBMA-*b*-P(A-r-B) BCPs were synthesized via two-step RAFT polymerization. The macromolecular chain transfer agent PHFBMA was synthesized first, followed by adding monomer A and B to build the second block. All the other monomers and initiators were purchased from Energy Chemical or J&K and purified by neutral alumina column or recrystallization to remove inhibitors and impurities. All the solvents, including hexafluoroisopropanol (HFIP), tetrahydrofuran (THF), methanol and 2-acetoxy-1-methoxypropane (PGMEA) were purchased from Titan and used as received.

All the synthesized BCPs were purified by dissolution twice and precipitation.

Gel permeation chromatography (GPC) characterizations of the molecular weight (M_n) and molecular weight distribution (PDI = M_w/M_n) of the polymers were performed on a Shimadzu instrument equipped with a differential refractive index (RI) detector, and an ultraviolet (UV) detector. THF was used as the eluent at a flow rate of 1.0 mL min^{-1}.

Differential scanning calorimetry (DSC) of polymers was performed on a TA Instruments Q2000 equipped with a RCS 90 electric freezing machine under nitrogen flow at a heating or cooling rate of 10 ˚C min^{-1}. TGA was performed on a PE Pyris 1 and measurements were taken under a nitrogen flow with a heating rate of 10 ºC min^{-1}.

The small-angle X-ray scattering (SAXS) diffraction patterns of powder polymer samples were collected on a Xenocs Xeuss 2.0 scattering system with a Pilatus 3R 200 K-A detector, which is equipped with Cu Kα radiation wavelength of 1.54 Å.

2.2. BCP bulk sample preparation

For SAXS characterizations, the bulk samples were prepared as follows: 1 mL 10 wt % BCP solution in THF was drop-casted on a clean Si wafer. After the evaporation of THF, the samples were annealed at 160 ºC under a nitrogen atmosphere for 24 h on a hot plate.

3. Results and discussion

3.1. Synthesis of PHFBMA-*b*-P(A-r-B)

The PHFBMA-*b*-P(A-r-B) BCPs were synthesized via two-step RAFT polymerization, and the corresponding synthetic route were presented in Fig. 1. The degree of polymerization (DP) of the macromolecular chain transfer agent PHFBMA was kept as 24. The GPC curves in Fig. 2 completely shifted to higher molecular weight, with PDI keeping relatively low (1.16), despite that the second block was composed of two monomers, indicating a uniform chain-to-chain monomer distribution.

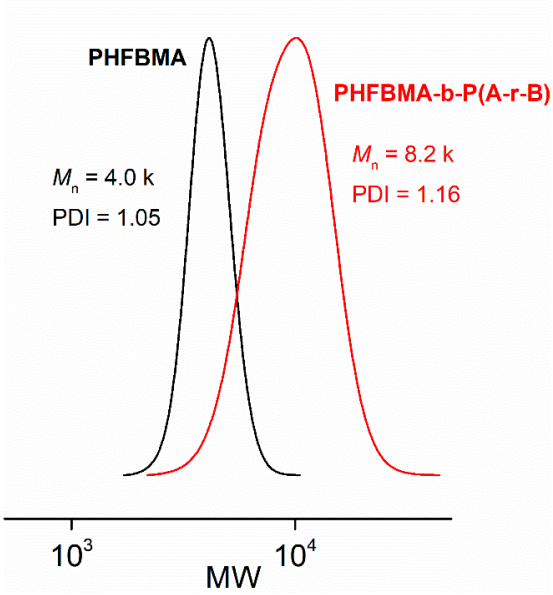

Fig. 2. Overlaid GPC curves of PHFBMA (black) and PHFBMA-b-P(A-r-B) block copolymers (red) of block copolymer S1.

M_n, DP and composition of the random copolymer block (A/B) of PHFBMA-*b*-P(A-r-B) were measured by ^{1}H NMR and summarized in Table 1. All the PHFBMA-*b*-P(A-r-B) BCPs have various M_n, ranged from 8.6 kg mol^{-1} to 14.3 kg mol^{-1} with low PDI (<1.16), and the composition of the two monomers in the random block could be tuned

from 81/19 to 76/24.

3.2. Phase separation in the bulk

If the random copolymer is uniform enough to act as one-component block, microphase separation is expected in such BCPs. Actually, the resulting BCPs could sub-10 nm lamellar morphology after annealing at 160 ºC for 24 h, as seen with SAXS in Fig. 3. Interestingly, BCP S1 and S2 exhibited similar d-spacings (13.0 nm vs 12.9 nm), although the DP of A-r-B block in BCP S1 was distinctly higher than that in BCP S2, which was attributed to the different incorporation amount of bulky monomer B in the random copolymer block. Further decrease of the DP of A-r-B block further to 5 resulted in disordered BCP.

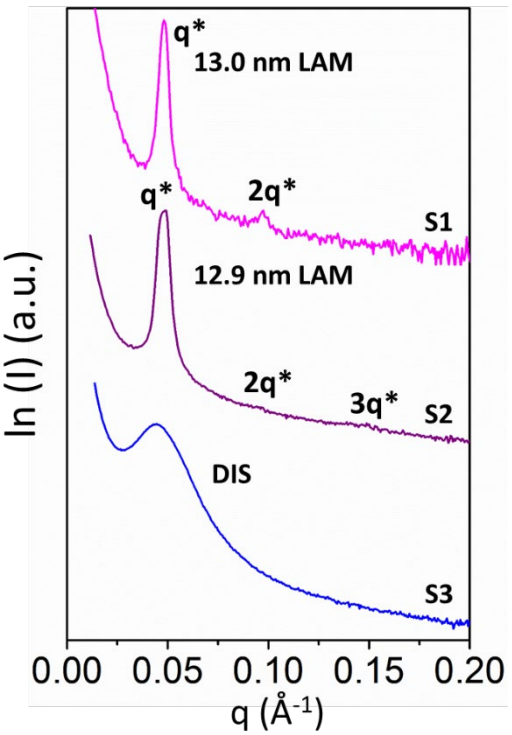

Fig. 3. SAXS profiles of PHFBMA-*b*-P(A-r-B) block copolymers S1-S3.

3.3. Themal analysis of PHFBMA-*b*-P(A-r-B)

The formation of random copolymer block was also demonstrated by the thermal analysis. As was shown in the DSC curves presented in Fig. 4, the T_g of PHFBMA homopolymer was 53 ºC. With the DP of A-r-B increasing from 5 to 20, two T_gs were observed in the PHFBMA-*b*-P(A-r-B), the higher T_g corresponded to PHFBMA block and the lower T_g was assigned to P(A-r-B) block. This was because that the incorporation of low T_g monomer B (T_g of the homopolymer of B was below 0 ºC while T_g of polymethacrylate was around 105 ºC) would dramatically decrease the T_g of the whole random copolymer block.

The thermal stability of PHFBMA-*b*-P(A-r-B) was also investigated by TGA, with a decomposition temperature (T_d) of 245 ºC, ensuring their stability under 160 ºC thermal annealing.

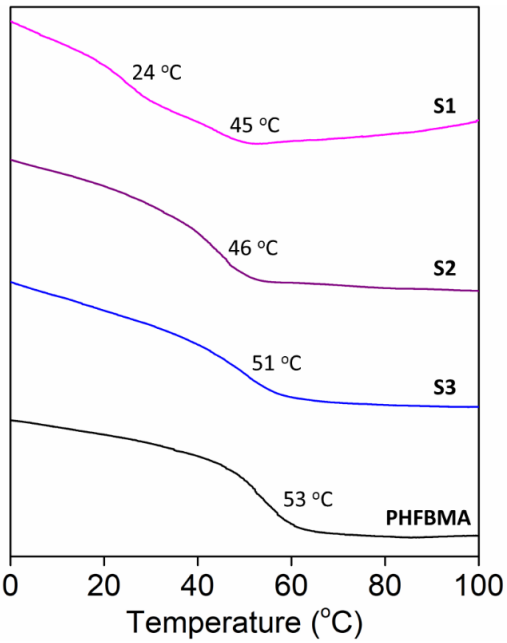

Fig. 4. DSC curves of block copolymers S1-S3 and PHFBMA homopolymer.

4. Conclusion

A series of fluorinated block copolymers with one block composed of random copolymer was synthesized by two-step RAFT polymerization. The resulted BCPs could form ordered lamellar structure with sub-10 nm domain size driven by fluorinated block after thermal annealing, confirming the uniformity of the random copolymer block. Each micro-domain consisted of two uniformly distributed monomers. Such a random copolymer block exhibited a low T_g, which could be tuned by the incorporated two components, indicating the possibility of achieving fine-tuning T_g as well as improved roughness for DSA patterning material.

Acknowledgement

This work was supported financially from the Shanghai Science and Technology Committee (18511104900) and Shanghai TD Advanced Material Technology Inc. (KCH1717170). The authors also acknowledge experimental support from the State Key Laboratory of Molecular Engineering of Polymers.

References

1. R. Ruiz, H. Kang, F. A. Detcheverry, E. Dobisz,

D. S. Kercher, T. R. Albrecht, J. J. de Pablo, and P. F. Nealey, *Science*, **321** (2008) 936.
2. M. Li and C. K. Ober, *Materials Today*, **9** (2006) 30.
3. J. Bang, U. Jeong, D. Y. Ryu, T. P. Russell, and C. J. Hawker, *Adv. Mater.*, **21**(2009) 4769.
4. H.-C. Kim, S.-M. Park, and W. D. Hinsberg, *Chemical Reviews*, **110** (2010) 146.
5. C. M. Bates, M. J. Maher, D. W. Janes, C. J. Ellison, and C. G. Willson, *Macromolecules*, **47** (2014) 2.
6. C. M. Bates and F. S. Bates, *Macromolecules*, **50** (2017) 3.
7. C. Wagner and N. Harned, *Nat. Photonics*, **4** (2010) 24.
8. A. M. Welander, H. Kang, K. O. Stuen, H. H. Solak, M. Muller, J. J. de Pablo, and P. F. Nealey, *Macromolecules*, **41** (2008) 2759.
9. L. Wan, R. Ruiz, H. Gao, K. C. Patel, T. R. Albrecht, J. Yin, J. Kim, Y. Cao, and G. Y. Lin, *ACS Nano*, **9** (2015) 7506.
10. C.-C. Liu, E. Han, M. S. Onses, C. J. Thode, S. X. Ji, P. Gopalan, and P. F. Nealey, *Macromolecules*, **44** (2011) 1876.
11. X. Li, J. Li, C. Wang, Y. Liu, and H. Deng, *J. Mater. Chem. C*, **7** (2019) 2535.
12. C. Wang, X. Li and H. Deng, *ACS Macro Lett.*, **8** (2019) 368.
13. X. Li and H. Deng, *Acs Appl. Polym. Mater.*, **2** (2020) 3601.
14. H. Cao, L. Dai, Y. Liu, X. Li, Z. Yang, and H. Deng, *Macromolecules*, **53** (2020) 8757.
15. H. Cao, X. Li, Y. Liu, and H. Deng, *J. Photopolym. Sci. Technol.*, **32** (2019) 413.
16. L. Dai, H. Cao, and H. Deng, *J. Photopolym. Sci. Technol.*, **33** (2020) 541.
17. H. Deng, X. Li, Y. Peng, and J. Zhou, *Proc. SPIE*, **10586** (2018) 105861E.
18. X. Li, Z. Li, L. Dai, H. Cao, and H. Deng, *Proc. SPIE*, 11326 (2020) 113261E.
19. H. Deng, X. Li, and J. Li, CN107245133B, US20180208697-A1, 2020.
20. Y. D. Luo, D. Montarnal, S. Kirn, W. C. Shi, K. P. Barteau, C. W. Pester, P. D. Hustad, M. D. Christianson, G. H. Fredrickson, E. J. Kramer, and C. J. Hawker, *Macromolecules*, **48** (2015) 3422.

Communication

Journal of Photopolymer Science and Technology
Volume 34, Number 4 (2021) 339−343 ©2021SPST

Synthesis of Highly Ordered Fluorinated Copolymers with One Polyhydroxystyrene Block for Subsequent Metal Incorporation

Zhenyu Yang and Hai Deng*

School of Micro-Electronics, State Key Laboratory of Molecular Engineering of Polymers
Fudan University, Shanghai 200433, China
**haideng@fudan.edu.cn*

Polyhydroxystyrene (PHS)-containing block copolymers (BCPs) were synthesized via reversible addition-fragmentation chain-transfer (RAFT) polymerization, and subsequent hydrolysis. Self-assembly domain size of poly (pentadecafluorooctyl methacrylate)-*block*-polyhydroxystyrene (PPDFMA-*b*-PHS) were measured by small-angle X-ray scattering (SAXS), revealing highly ordered nanostructure. The effective Flory-Huggins parameter χ (150 ºC) is 0.268. The resulted PPDFMA-*b*-PHS then reacted with metal ion or metallocene compounds. BCPs chemically bonded with metal ion were obtained.

Keywords: fluorinated BCPs, PHS-containing BCPs, Self-assembly, Sub-7 nm, Metal-containing BCP

1. Introduction

As extreme ultra violet lithography (EUVL) approaching its intrinsic resolution limit [1-2], directed self-assembly (DSA) is considered as an attractive alternative approach [3-13] due to its high resolution up to 5nm L/S [14].

In our recent studies, we demonstrated that BCPs with perfluoroalkyl-containing methacrylic block

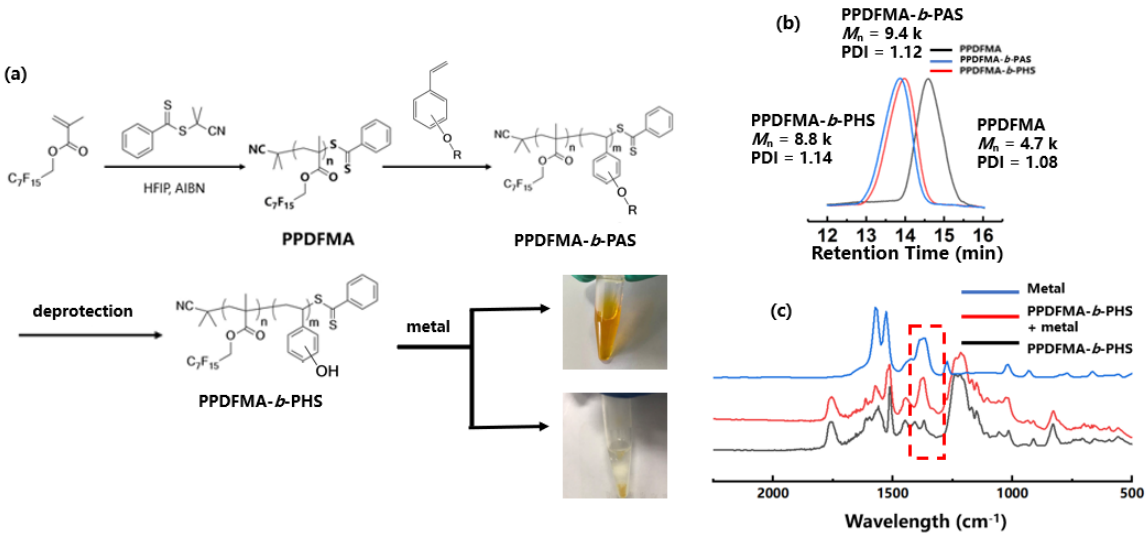

Fig. 1 (a) Synthetic route of PPDFMA-*b*-PHS via reversible addition-fragmentation chain-transfer (RAFT) polymerization followed by hydrolysis. Subsequent addition of metallocene or metal ion resulted in solution and insoluble solid; (b) GPC curves of PPDFMA (black), poly (pentadecafluorooctyl methacrylate)-*block*-poly acetoxystyrene (PPDFMA-*b*-PAS) (blue) and PPDFMA-*b*-PHS (red); (c) IR spectra of PPDFMA-*b*-PHS (black), metallocene introduced PPDFMA-*b*-PHS (red) and metallocene compound (blue).

Received April 1, 2021
Accepted May 3, 2021

can achieve sub-5 nm microdomains, with fast assembly speed up to 1 min at 80 °C annealing [15-19]. Although we successfully synthesized poly (pentadecafluorooctyl methacrylate)-*block*-poly(3-hydroxystyrene) (PPDFMA-*b*-P3HS) and demonstrated its fast assembly behavior [16], the isomer of poly(4-hydroxystyrene) (P4HS) is still under investigation. Furthermore, in order to enhance etch resistance, we introduced metallocene into BCPs with poly(2-vinylpyridine) (P2VP) block, showing better plasma etch resistance [20-21].

In this study, we synthesized PPDFMA-*b*-P4HS and characterized its effective Flory-Huggins parameter χ value, a parameter describing the binary monomer-monomer incompatibility [22-23], and its assembly micro structure and domain size. We also utilized hydroxy group in PHS BCPs to react with metal ion to increase etch resistance. Many attempts of introducing metal reagents into PHS domains were conducted.

2. Experimental

2.1. Synthesis and Characterization

Series of fluorine-containing hydroxystyrene BCPs were synthesized via RAFT polymerization and subsequent deprotection (Fig. 1a). The monomers utilized, 1H,1H-pentadecafluorooctyl methacrylate (PDFMA, 96%) and 4-acetoxystyrene (4AS, 96%) were purchased from Sigma-Aldrich and purified by passing through a neutral alumina column to remove stabilizer. The RAFT chain transfer reagent (CTA) 2-cyano-2-propylbenzodithioate (CPDB, 98%) was purchased from Stream. Hexafluoroisopropanol (99%, HFIP) was purchased from Admas-beta and was dried and de-oxygenated following standard procedures. Azoisobutyronitrile (AIBN, 98%) was received from Admas-beta and used after recrystallization from ethanol. Other chemicals were used as received without other purification.

All BCPs were purified by dissolution and precipitation. ^{1}H NMR spectrum was recorded on a Bruker spectrometer (Advanced HD III) using $CDCl_3$ and THF-d^8 as solvents with tetramethylsilane as an internal standard. Gel permeation chromatography (GPC) characterizations were conducted by an Agilent/Wyatt 1260 GPC eluting with THF (flow rate of 1 mL min^{-1}). The small-angle X-ray scattering (SAXS) diffraction patterns of powder polymer samples were recorded with a Xenocs Xeuss 2.0 scattering system with a Pilatus 3R 200K-A detector equipped with Cu K α radiation wavelength of 1.54 Å. Fourier transform infrared (FT-IR) spectroscopy measurements were conducted with a Thermo Fisher Nicolet 6700 at room temperature, and the samples were pressed into KBr pellets before measurements.

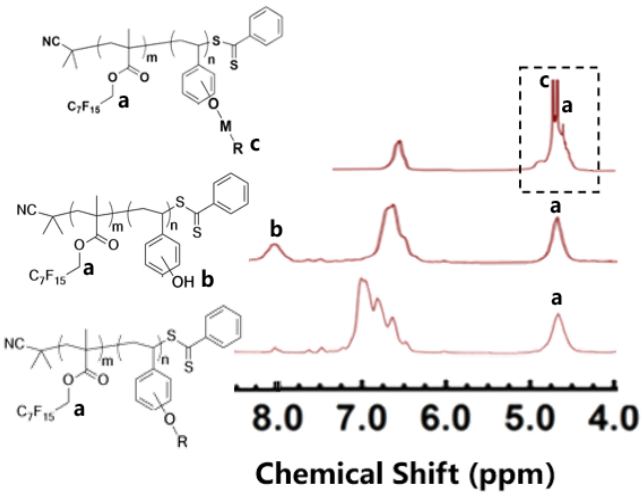

Fig. 2 ^{1}H NMR spectra of the block copolymers: PPDFMA-*b*-P4AS, PPDFMA-*b*-P4HS and metallocene introduced PPDFMA-*b*-P4HS.

Table 1. Characterizations of PPDFMA-*b*-PHS hydrolyzed from PPDFMA-*b*-PAS

Sample	$M_{n,NMR}$[a] (kg mol^{-1})	PDI[b]	Metal Introduced	Morphology[c]	χ_{eff}[d] @150°C	Solubility[e]	χN[f]
PAS	9.4	1.12	NA	HEX	0.167	Soluble	16.7
PHS	8.8	1.14	NA	HEX	0.268	Soluble	24.7
PHS-M	9.3	1.18	Metallocene	DIS	/	Soluble	/
PHS-M	/	/	Ni^{2+}, Co^{3+} (NO_3^-)	/	/	Insoluble	/

a) The molecular weights ($M_{n,\ NMR}$) were calculated by ^{1}H NMR results. DP of PPDFMA and PAS/PHS was 11.4 and 25, respectively. b) Polydispersity indexes (PDI) were measured by GPC in THF against PS standards. c) HEX represented hexagonal morphology, while DIS represented disordered structure was obtained after thermal annealing at 160 °C for 20 h. d) The effective χ value at 150°C. e) Solubility was tested via dispersing 10 mg samples in various solvents (DCM, THF, PGMEA) and then ultrasonicating for 4 h. f) *N* represented the total DP and was calculated by reference volume v_0 = 118 Å^3, based on the densities of PPDFMA and PAS/PHS. The *N* values of PPDFMA-*b*-PHS and PPDFMA-*b*-PAS were 92 and 100, respectively.

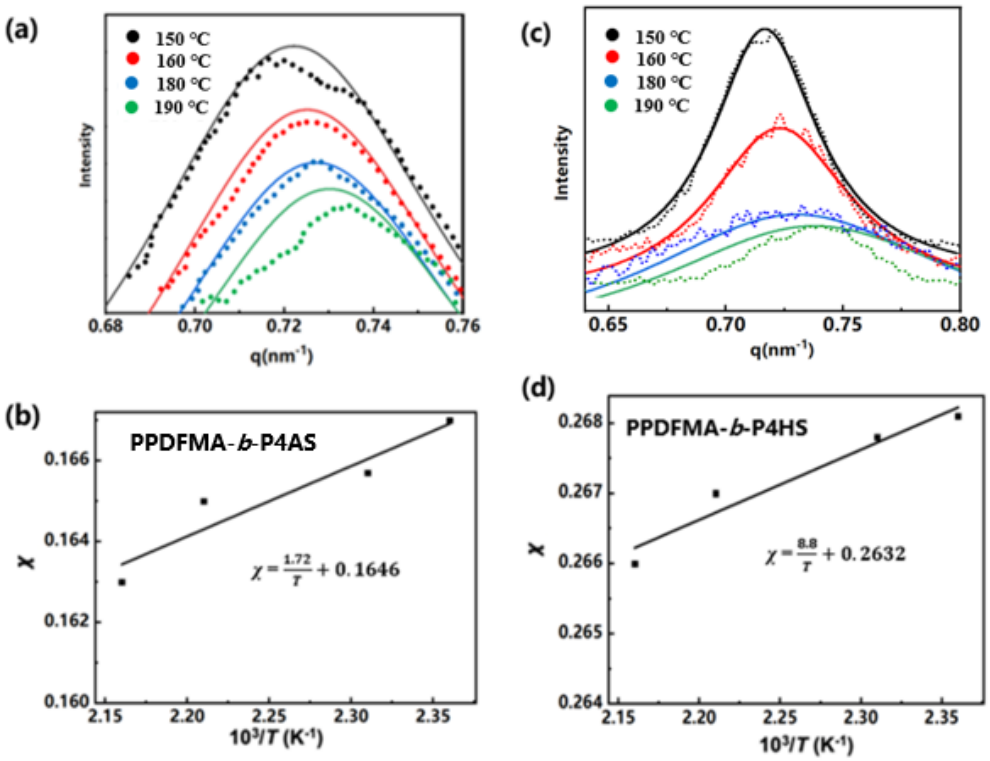

Fig. 3 (a) SAXS data and fitlines of SAXS intensities of disordered PPDFMA-*b*-P4AS at various temperatures (χ = 0.167 at 150 °C). (b) Temperature dependence of χ between PPDFMA and P4AS. (c) SAXS data and fitlines of SAXS intensities of disordered PPDFMA-*b*-P4HS at various temperatures (χ = 0.268 at 150 °C). (d) Temperature dependence of χ between PPDFMA and P4HS.

2.2. Preparation of BCP Bulk Samples

Two drops of a viscous, concentrated (~10 wt%) solution of BCPs in THF were gently placed onto a washed silicon wafer. The THF was evaporated under ambient conditions for 1 h. The samples were thermally annealed to observe their corresponding microphase-separated structures. The morphologies of these annealed samples were investigated by SAXS at room temperature.

2.3. Introduction of metal compound into BCPs

Addition of metallocene dichlorides was accomplished through dissolving PPDFMA-*b*-P4HS and PPDFMA-*b*-P3HS BCPs and metallocene dichlorides in dichloromethane and ultrasonicating for 4 h after adding triggering triethylamine at room temperature. Introduction of metal salts including nickel nitrate and cobalt nitrate was done by dissolving PPDFMA-*b*-P4HS BCPs and metal salt in dichloromethane and then ultrasonicating for 2 h at room temperature.

3. Results and discussion

3.1. Synthesis and characterizations of BCPs

An acetoxy group-containing monomer, 4AS was used to synthesize BCP systems and PPDFMA-*b*-P4HS BCPs were obtained after subsequent deprotection (Fig. 1). PPDFMA-*b*-P3HS BCPs were obtained through previous method reported.[16]

The polymer dispersity index (PDI) was determined by GPC. The GPC curve shows a good living nature of the RAFT polymerization of the 4AS monomer from fluorinated macroinitiator (PDI = 1.12, Fig. 1b.). The monodisperse nature was also well maintained through deprotection (PDI = 1.14, Fig. 1b).

The hydrolysis of acetoxy group was confirmed by the ^{1}H-NMR spectra. After hydrolysis, the hydrogen of benzene in PPDFMA-*b*-P4HS showed a single peak compared to multiple peaks in PPDFMA-*b*-P3HS [16].

The χ values of poly (pentadecafluorooctyl methacrylate)-block-poly(4-acetoxystyrene) (PPDFMA-*b*-P4AS) and PPDFMA-*b*-P4HS BCPs were estimated by Leibler's mean field theory using the random phase approximation of the absolute intensity from SAXS [24].

Morphologies and domain spacings of PPDFMA-*b*-P4AS and PPDFMA-*b*-P4HS BCPs were determined by SAXS. Fully disordered BCPs were used to estimate χ values, and the χ values at 150 °C of PPDFMA-*b*-P4AS and PPDFMA-*b*-P4HS are

0.167 and 0.268, respectively, all of which are higher than conventional PS-*b*-PMMA BCP (χ = 0.030, at 150 ºC). With exposed hydroxyl groups, the hydrophilicity of the styrene block is increased, therefore increasing the incompatibility between the two blocks and resulting in higher χ value of PPDFMA-*b*-P4HS BCPs than PPDFMA-*b*-P4AS (Fig. 3).

Both PPDFMA-*b*-P4AS and PPDFMA-*b*-P4HS are high χ BCPs, forming sub-7 nm hexagonal microdomains (see Table 1), which is similar to that of PPDFMA-*b*-P3HS reported previously [16].

3.2 Incorporation of metal into BCPs

In order to enhance etch resistance, both BCPs containing P3HS and P4HS were employed to incorporate metal ions. After reaction between metallocene dichlorides or nitrate salts and -OH group in PHS at 1:1 mole ratio, incorporation of metallocene was confirmed by the ligand peaks in FT-IR and ^{1}H NMR spectra (Fig. 1c, Fig. 2). Ligand peaks were observed at 1300 cm^{-1} in IR and 4.7 ppm in ^{1}H-NMR.

Surprisingly, after the reaction and 10 h annealing at 160 ºC, the nanodomain structure disappeared, which indicated strong interaction between metal ion and -OH group. Such phenomenon is different from the result of metallocene-P2VP system [20].

It seems like strong chemical bonding between oxygen and metal ion could destroy the ordered nanostructure. The nitrate salts actually directly resulted in insoluble solids, which may be the same cause.

By choosing adequate metal ions and ligands, we are expecting to obtain PHS-metal BCPs with highly ordered structure.

4. Conclusion

Series of F-containing hydroxystyrene BCPs, PPDFMA-*b*-PHS, were synthesized via RAFT followed by hydrolysis. Confirmed by ^{1}H NMR and GPC, BCPs with narrow PDI were successfully synthesized. The Flory-Huggins parameter χ of resulted BCPs is 0.268. Subsequent reaction with metal salts and metallocenes resulted in insoluble solids and solution from both PPDFMA-*b*-P4HS and PPDFMA-*b*-P3HS. Large amount of metallocenes reacted with PHS changed the BCP from a hexagonal cylindrical domain to disordered. More detailed results will be reported.

Acknowledgement

This work was supported financially from the Shanghai Science and Technology Committee (18511104900). The authors also acknowledge experimental support from the State Key Laboratory of Molecular Engineering of Polymers and the Nano-fabrication Laboratory of Fudan University.

References

1. G. Tallents, E. Wagenaars, and G. Pert, *Nature Photonics*, **4** (2010) 809.
2. R. Gronheid, C. K. Hohle, A. Oshima, F. Philippe, D. De Simone, H. Nakagawa, H. Nakashima, S. Biesemans, K. Nafus, T. Shiozawa, Y. Konishi, R. Aizawa, H. Makoto, T. Moriya, K. Takeshita, M. Tomono, R. Shimada, K. Yoshihara, Y. Kondo, H. Ide, Y. Minekawa, G. Shiraishi, S. Nagahara, M. Miyake, S. Tagawa, G. Vandenberghe, S. Dei, M. Hori, T. Naruoka, T. Kimura, M. Shima, T. Nagai, and M. Carcasi, *Advances in Patterning Materials and Processes XXXV*, Conference Presentation (2018).
3. H. C. Kim, S. M. Park, and H. D. Hinsberg, *Chem Rev*, **110** (2010) 146.
4. T. P. Russell, R. P. Hjelm, and P. A. Seeger, *Macromolecules*, **23** (1990) 890.
5. Y. Zhao, E. Sivaniah, and T. Hashimoto, *Macromolecules*, **47** (2008) 2.
6. C. C. Liu, E. Han, M. S. Onses, C. J, Thode, S. Ji, P. Gopalan, and P. F. Nealey, *Macromolecules*, **44** (2011) 1876.
7. L. Wan, R. Ruiz, H. Gao, K. C. Patel, T. R. Albrecht, Y. Jian, J. Kim, Y, Cao, and G. Lin, *ACS Nano*, **9** (2015) 7506.
8. G. Seguini, T. J. Giammaria, F. F. Lupi, K. Sparnacci, D. Antonioli, V. Gianotti, F. Vita, I. F. Placentino, J. Hilhorst, C. Ferrero, O. Francescangeli, M. Laus, and M. Perego, *Nanotechnology*, **25** (2014) 045301.
9. D. P. Sweat, M. Kim, S. R. Larson, J. W. Choi, Y. Choo, C. O. Osuji, and P. Gopalan, *Macromolecules*, **47** (2014) 6687.
10. D. P. Sweat, M. Kim, A. K. Schmitt, D. V. Perroni, C. G. Fry, M. K. Mahanthappa, and P. Gopalan, *Macromolecules*, **47** (2014) 6302.
11. K. Azuma, J. Sun, Y. Choo, Y. Rokhlenko, J. H. Dwyer, B. Schweitzer, T, Hayakawa, C. O. Osuji, and P. Gopalan, *Macromolecules*, **51** (2018) 6460.
12. J. Kwak, A. K. Mishra, J. Lee, K.S. Lee, C. Choi, S. Maiti, M. Kim, and J. K. Kim, *Macromolecules*, **50** (2017) 6813.

13. G. Jeong, D. M. Yu, J. K. D. Mapas, Z. Sun, J. Rzayev, and T. P. Russell, *J. Mater. Chem. C*, **7** (2019) 2535.
14. A. P. Lane, X. Yang, M. J. Maher, G. Blachut, Y. Asano, Y. Someya, A. Mallavarapu, S. M. Sirard, C. J. Ellison, and C. G. Willson, *ACS Nano*, **11** (2017) 7656.
15. X. Li, J. Li, C. Wang, Y. Liu, and H. Deng, *J. Mater. Chem. C*, **7** (2019) 2535.
16. C. Wang, X. Li, and H. Deng, *ACS Macro Lett.*, **8** (2019) 368.
17. X. Li, C. Wang, J. Zhou, Z. Yang, Y, Zhang, and H. Deng, *J. Photopolym. Sci. Technol.*, **31** (2018) 483.
18. H. Deng, X. Li, Z. Li, L. Dai, and H. Cao, *Advances in Patterning Materials and Processes XXXVII*, **11326**(2020) 113261E.
19. H. Deng, X. Li, and Y. Peng, *Advances in Patterning Materials and Processes XXXV*, **10586** (2018) 105861E.
20. X. Li and H. Deng, *ACS Applied Polymer Materials*, **2** (2020) 3601.
21. G. Wu and H. Deng, *J. Photopolym. Sci. Technol.*, **33** (2020) 537.
22. M. W. Matsen and M. Schick, *Phys. Rev. Lett,* **72** (1994) 2660.
23. F. S. Bates and G. H. Fredrickson, *Annu. Rev. Phys. Chem*. **41** (1990) 525.
24. L. Leibler, *Macromolecules*, **13** (1980) 1602.

Journal of Photopolymer Science and Technology
Volume 34, Number 4 (2021) 345−350 ©2021SPST

Environmental Dependence of Chemiluminescence Using Solvatochromic Molecules

Masaki Kayama*, Kohei Iritani, and Takashi Yamashita**

Department of Applied Chemistry, School of Engineering,

Tokyo University of Technology, 1404-1 Katakura, Hachioji, Tokyo 192-0982, Japan

**kayamamsk@stf.teu.ac.jp, **yamashitatks@stf.teu.ac.jp*

Functional dyes are one of the most attractive materials because of their potential use in microenvironment probes, bioapplications, and optoelectronic devices. The modification of chemical structures of the functional dyes due to external stimuli such as heat and photo-irradiation affects the absorption and emission behavior of the dyes. Among them, solvatochromic molecules are attracting great interest because they are used as molecular sensors and indicators. Herein, we investigated chemiluminescence using betaine 30 and dansyl acid ethyl ester (**DNSE**) as solvatochromic molecules. We demonstrated chemiluminescent reactions using a mixture of betaine 30 or **DNSE** as the functional dye and bis(2,4,6-trichlorophenyl) oxalate as a precursor to introduce a high-energy moiety under chemiluminescence conditions in several solvents. Although betaine 30 did not exhibit fluorescence except with toluene, **DNSE** showed different emission colors depending on the solvent polarity, which indicated that chemiluminescence depends on the environment.

Keywords: Chemiluminescence, Solvatochromism, Betaine 30, Dansyl group

1. Introduction

Functional dyes are attracting intense interest in applications such as photo-memories, optical devices, and dimming windows [1–4] because their absorbance and fluorescence can be controlled by the external stimuli such as heat and photo-irradiation. Crenshaw et al. [5] and Pucci et al. [6] reported that the emission wavelengths of solid-state distyrene derivatives were modified by changing their aggregation mechanisms following external stress. Imato et al. have reported the development of mechanochromic materials, in which a color change was observed in response to external stress, using a polymer with a spiropyran group [7]. Furthermore, we successfully showed volume phase transition using an *N*-isopropylacrylamide derivative and detected the emission of a dansyl group [8]. Solvatochromic molecules, in which the absorption and emission wavelengths change depending on the solvent polarity, are well-known functional dyes. Several studies have proposed their application as molecular sensors and indicators for examining solution polarity [9–12]. The solvatochromic molecules may also help develop solvatochromic materials.

Chemiluminescence is observed when a chemical moiety in the excited state is stabilized to its ground state, accompanied with the emission of fluorescence [13–16]. For example, 1,2-dioxetanedione is produced when oxalate derivatives are treated with hydrogen peroxide and an inorganic salt; subsequently, it changes to carbon dioxide with energy emission. When the dyes are mixed in the reaction system, they receive the emitted energy and exhibit fluorescence. In conventional research on chemiluminescence, the emission wavelengths were controlled by modifying the chemical structures of the dyes [15,16].

The purpose of the present study is to develop a solvatochromic dye using the chemiluminescence method, in which the wavelength of emission is controlled by

Received November 16, 2020
Accepted April 30, 2021

environmental conditions. To this end, we used betaine 30 [17–20] and a dansyl acid derivative [21–23] as solvatochromic molecules (Figure 1). The former, a well-known solvatochromic molecule, is a relatively highly polar molecule because it has both cationic and anionic charges within its molecular structure. Solvatochromism results due to the formation of a different molecular structure depending on polarity of solvents when the solvation manner of the polar ground state is varied with respect to the less polar excited state [17]. The dansyl group is generally used as a fluorescent labeling reagent for proteins and amino acids. Because the dansyl group has a large Stokes shift, its fluorescence quantum yield and emission wavelength are expected to change with solvent polarity. However, its solubility is quite low. Therefore, we used an esterified derivative of the dansyl group, dansyl acid ethyl ester (**DNSE**) [24, 25], to improve its low solubility. In addition, chemiluminescence reactions were performed using bis(2,4,6-trichlorophenyl) oxalate as a precursor to produce an excited intermediate with sodium carbonate and hydrogen peroxide. Figure 2 shows the chemiluminescence reaction. Although we did not visually observe chemiluminescence of betaine 30 because its fluorescence intensity was relatively low except with toluene, we showed the environmental dependence of chemiluminescence of **DNSE** using relatively low-polarity solvents.

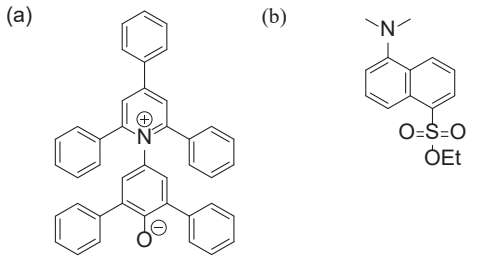

Fig. 1. Chemical structures of betaine 30 (a) and dansyl acid ethyl ester, **DNSE** (b).

2. Experimental

2.1. Apparatus

UV-vis absorption spectroscopy measurements were performed using a UV-visible spectrophotometer (V-550, JASCO Corporation UV-2600, SHIMADU Corporation), and emission and excitation spectroscopy measurements were performed using a spectrofluorometer (FP-6200 and FP8300 JASCO Corporation) with each solvent. The excitation wavelengths for the emission spectra and the detected wavelengths for the excitation spectra of betaine 30 and **DNSE** are summarized in Tables 1 and 2, respectively. ^{1}H NMR (400 MHz) spectra were measured on a Bruker UltraShield Plus 400

Table 1. Summary of excitation wavelengths for emission spectra and detected wavelengths for excitation spectra of betaine 30.

Solvent	Excitation wavelength of emission spectra (nm)	Detected wavelength of excitation spectra (nm)
MeOH	500	525
acetone	352	393
EtOAc	320	383
toluene	358	440

Table 2. Summary of excitation wavelengths for emission spectra and detected wavelengths for excitation spectra of **DNSE**.

Solvent	Excitation wavelength of emission spectra (nm)	Detected wavelength of excitation spectra (nm)
NAA	356	531
DMF	359	530
MeOH	350	529
DEP	358	514
EtOH	352	526
Acetone	354	522
CH_2Cl_2	358	507
THF	351	501
EtOAc	351	501
Toluene	352	482
HFB	354	475
Hexane	342	449

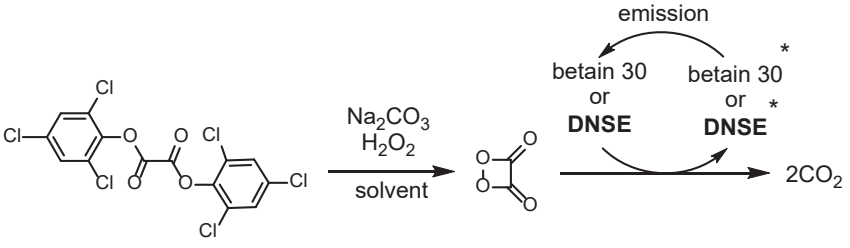

Fig. 2. Chemical reactions of chemiluminescence.

spectrometer. The spectra were referenced to the proton signal of tetramethylsilane (0 ppm) in $CDCl_3$.

2.2. Reagents

All commercially available reagents were used as received from TCI or Wako Pure Chemical Industries, Ltd.

2.3. Syntheses of compounds

2.3.1. Preparation of betaine 30 [17]

A mixture of 4-amino-2,6-diphenylphenol (254 mg, 972 μmol), 2,4,6-triphenylpyrylium hydrogensulfate (399 mg, 982 μmol), sodium acetate (2.02 g, 24.6 mmol), and ethanol (9.9 mL) was refluxed for 3 h. To the mixture, 1 M NaOH *aq*. (178 mg) was added. Then, ethanol was removed under vacuum and the crude product was washed with pure water. After filtration, the product was dried under vacuum for 88 h. The crude mixture was purified by silica gel column chromatography (CH_2Cl_2/EtOH = 9/1) to afford betaine 30 (44% yield) as a blue solid. The chemical reaction is shown in Figure 3a.

^{1}H NMR (400 MHz, $CDCl_3$, 25 °C): δ 8.06 (s, 2H), 7.86–7.88 (m, 2H), 7.62–7.64 (m, 3H), 7.38–7.39 (m, 10H), 7.31–7.33 (m, 4H), 7.16 (t, J = 7.5 Hz, 4H), 7.08 (t, J = 7.5 Hz, 2H), 6.45 (s, 2H).

2.3.2. Preparation of **DNSE** [24]

Dansyl chloride (403 mg, 1.48 mmol) and 1,8-diazabicyclo[5.4.0]undec-7-ene (DBU) (225 mg, 1.48 mmol) were dissolved in ethanol (20 mL). The reaction mixture was stirred at room temperature. After 17 h, the mixture was added dropwise to water. The product was extracted with CH_2Cl_2. The organic layer was dried over Na_2SO_4. After removing the solvent under vacuum, the mixture was subjected to silica gel column chromatography (CH_2Cl_2/hexane = 4/1) to obtain **DNSE** (50% yield) as a yellow solid. The chemical reaction is shown in Figure 3b.

^{1}H NMR (400 MHz, $CDCl_3$, 25 °C): δ 8.59 (d, J = 8.0 Hz, 1H), 8.26 (dd, J = 7.3 and 1.2 Hz, 1H), 8.11 (d, J = 8.0 Hz, 1H), 7.71 (dd, J = 10.1 and 9.7 Hz, 1H), 7.69 (dd, J = 10.1 and 9.7 Hz, 1H), 7.30 (d, J = 8.0 Hz, 1H), 4.05 (q, J = 8.0 Hz, 2H), 2.84 (s, 6H), 1.15 (t, J = 8.0 Hz, 3H).

2.4. Chemiluminescence reaction

A mixture of bis(2,4,6-trichlorophenyl) oxalate (50 mg, 110 μmol), sodium carbonate (100 mg, 940 μmol), dye (0.1 eq. of betaine 30 or **DNSE**), and solvent (10 mL) was treated with an ultrasonic cleaner. After 5 min, 35% hydrogen peroxide *aq.* (3 mL) was added to the mixture.

3. Results and discussion

3.1. Optical properties of betaine 30 based on solvents

We measured the UV spectra of betaine 30 (1.0×10^{-4} M) using methanol, acetone, ethyl acetate, and toluene as solvents (Figure 4). Table 3 shows a summary of maximum wavelengths of absorption (λ_{Abs}), emission (λ_{Em}), and excitation (λ_{Ex}) in each solution. The value of λ_{Abs} red-shifted from 525 nm (MeOH) to 738 nm (ethyl acetate) as the polarity of the solvent except toluene (429 nm) was increased. In addition, concentration quenching was observed in the excitation spectrum of toluene.

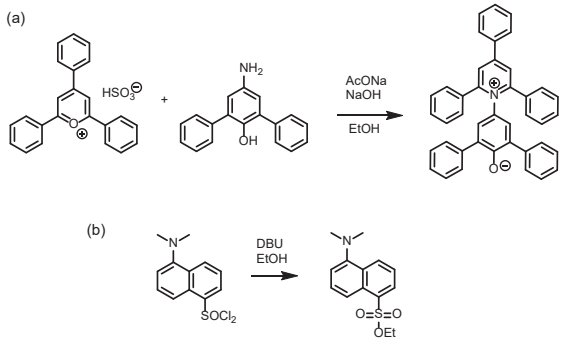

Fig. 3. Schemes of syntheses of betaine 30 (a) and **DNSE** (b).

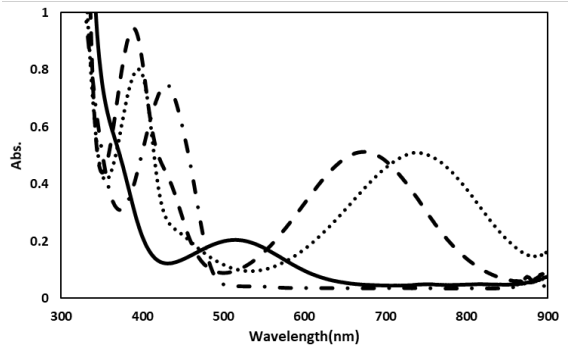

Fig. 4. UV spectra of betaine 30 measured in methanol (solid line), acetone (broken line), ethyl acetate (dotted line), and toluene (chain line).

Figure 5 shows the emission and excitation spectra of betaine 30 using methanol, acetone, ethyl acetate, and toluene (1.0×10^{-4} M). Table 3 shows summary of λ_{Abs}, λ_{Em}, and λ_{Ex} for these spectra. For acetone and ethyl acetate, although λ_{Abs} was detected at 685 nm , 738 nm (Figure 4), the corresponding emission was not observed. Instead, emission at 467 nm was detected for excitation at 400 nm for methanol. For the other solvents, emissions corresponding to the absorption of betaine 30 were observed. For fluorescence in the visible range, the intensity of emission in toluene was the highest, although the intensity of the detected emissions was relatively weak.

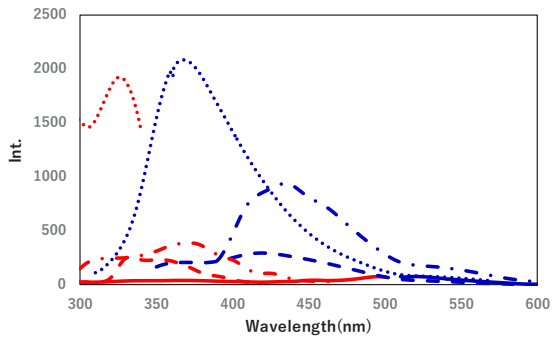

Fig. 5. Emission (blue) and excitation (red) spectra of betaine 30 in methanol (solid line), acetone (broken line), ethyl acetate (dotted line), and toluene (chain line).

Table 3. Summary of maximum wavelengths of absorption (λ_{Abs}), emission (λ_{Em}), and excitation (λ_{Ex}).

Solvent	λ_{Abs} (nm)	λ_{Ex} (nm)	λ_{Em} (nm)
MeOH	525	500	522
acetone	394, 685	352	420
EtOAc	399, 738	320	370
toluene	429	358	437

3.2. Chemiluminescence using betaine 30

Although the intensity of betaine 30 was low, we performed its chemiluminescence reaction using the method described in Section 2.4. We demonstrated the reaction using methanol, acetone, ethyl acetate, and toluene solvents; however, we could visually detect chemiluminescent emission only in toluene (Figure 6). In other solvents, unfortunately, we did not observe chemiluminescent emission because of the low intensity of the emission.

Fig. 6. Photo image of the mixture of reagents for chemiluminescence using betaine 30 as a dye in toluene.

3.3. Optical properties of **DNSE** based on solvents

Next, we investigated the optical properties of **DNSE** using *N*-methylacetamide (NAA), dimethylformamide (DMF), methanol, diethyl phthalate (DEP), ethanol, acetone, CH_2Cl_2, ethyl acetate, toluene, hexafluorobenzene (HFB), and hexane as the solvent. The solute concentration of **DNSE** was 1.0×10^{-4} M for each solvent [25]. Figures 7 and 8 show the UV spectra and emission and excitation spectra, respectively, obtained with each solution. The values of λ_{Abs}, λ_{Em}, and λ_{Ex} with permittivity are summarized in Table 4. The λ_{Abs} was detected between 330 and 360 nm for all solutions. However, λ_{Em} shifted to longer values with increasing polarity of the solvent. The λ_{Em} was detected at 449 nm in hexane (the lowest-polarity solvent) and at 529

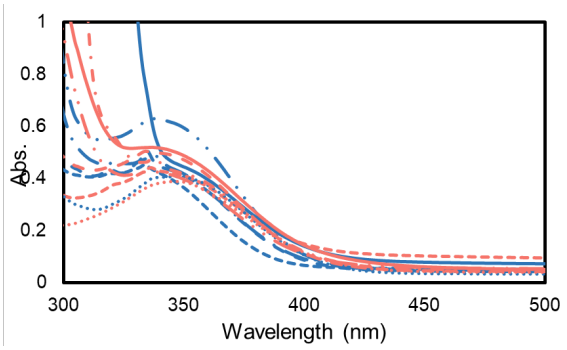

Fig. 7. UV spectra of **DNSE** in NAA (pink solid line), DMF (pink dotted line), methanol (pink broken line), DEP (pink one-dot chain line), ethanol (pink two-dot chain line), acetone (blue solid line), CH_2Cl_2 (blue dotted line), THF (pink short broken line), ethyl acetate (blue broken line), toluene (blue one-dot chain line), HFB (blue two-dot chain line), and hexane (blue short broken line).

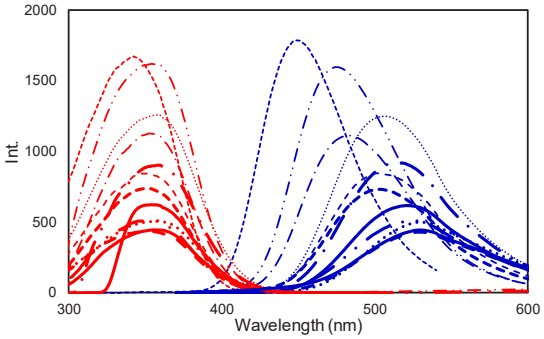

Fig. 8 Emission (blue) and excitation (red) spectra of **DNSE** in NAA (bold solid line), DMF (bold dotted line), methanol (bold broken line), DEP (bold one-dot chain line), ethanol (bold two-dot chain line), acetone (narrow solid line), CH_2Cl_2 (narrow dotted line), THF (bold short broken line), ethyl acetate (narrow broken line), toluene (narrow one-dot chain line), HFB (narrow two-dot chain line), and hexane (narrow short broken line).

Table 4. Summary of maximum wavelengths of absorption (λ_{Abs}), emission (λ_{Em}), excitation (λ_{Ex}), and the value of permittivity (E).

Solvent	λ_{Abs} (nm)	λ_{Em} (nm)	λ_{Ex} (nm)	E (ev)
NAA	337	529	356	2.34
DMF	334	530	359	2.34
MeOH	334	529	350	2.34
DEP	338	514	358	2.41
EtOH	336	524	352	2.37
acetone	360	520	354	2.38
CH_2Cl_2	347	506	358	2.45
THF	336	504	351	2.46
EtOAc	335	501	351	2.48
toluene	337	483	352	2.57
HFB	338	474	354	2.62
hexane	334	449	342	2.76

nm in NAA (the highest-polarity solvent). Moreover, large Stokes shifts were detected with a maximum of 173 nm for NAA solution and a minimum of 107 nm for hexane solution (Figure 8). Furthermore, the intensity of fluorescence in the lower-polarity solvents was weaker than that in higher-polarity solvents.

To summarize the solvent effect on the emission of **DNSE**, we plotted the fluorescent energies using the relative dielectric constants [26] for each solvent. The fluorescent energies (E) were calculated using the following formula:

$$E = hc / \lambda,$$

where h and c are the Planck constant and the speed of light, respectively. Figure 9 shows the plot of the calculated fluorescent energies with respect to the relative dielectric constants. The fluorescent energies were relatively higher in lower-polarity solvents. In contrast, the

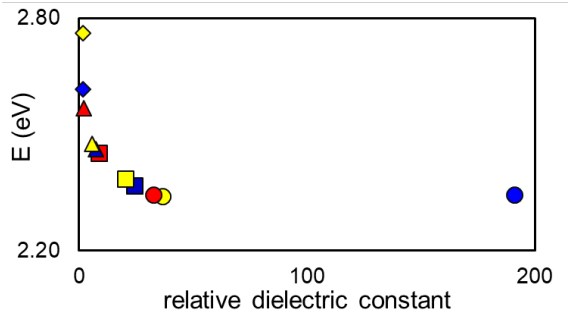

Fig. 9. Plots of the fluorescence energies of **DNSE** in NAA (blue circle), DMF (yellow circle), MeOH (red circle), EtOH (blue square), acetone (yellow square), CH_2Cl_2 (red square), THF (blue triangle), EtOAc (yellow triangle), toluene (red triangle), HFB (blue rhombus), and hexane (yellow rhombus) solution with respect to the relative dielectric constants.

fluorescence energies of **DNSE** in solvents with relatively higher relative dielectric constants were observed at a constant value of ~2.3 eV.

3.4. Chemiluminescence using ethyl dansylate

We performed chemiluminescent experiments using **DNSE** in NAA, DMF, methanol, DEP, ethanol, acetone, CH_2Cl_2, THF, ethyl acetate, toluene, HFB and hexane. Figure 10 shows the photos of the reaction mixtures in each solvent taken after adding hydrogen peroxide *aq*. No light emission was detected visually in the NAA, DMF, methanol, ethanol, and acetone EtOAc, and hexane solutions, while the emission was detected visually in DEP, CH_2Cl_2, THF, toluene and HFB. The emission colors of the solutions owing to chemiluminescence are relatively well consistent with the fluorescent wavelengths detected in the solution phase (Table 4), which indicates that **DNSE** was excited by 1,2-dioxetanedione produced from bis(2,4,6-trichlorophenyl) oxalate in the organic phase. Surprisingly, the lifetime of the THF emission instantaneously decreases when hydrogen peroxide was added. Although we

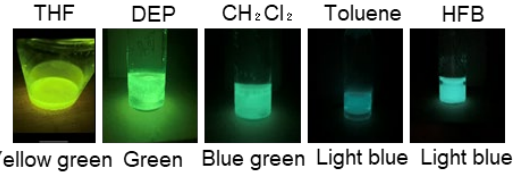

Fig. 10. Photo images of the solutions after chemluminescent reaction using **DNSE** in THF, DEP, CH_2Cl_2, toluene and HFB solution.

could not completely understand this phenomenon, we hypothesize that energy transfer from 1,2-dioxetanedione to **DNSE** occurred momentarily in the THF and water solution because of their miscibility. Note that, in highly polar solvents, the emission of **DNSE** was not visualized, probably because the rate of chemiluminescent reaction is too fast to visually detect the emission caused by the miscibility of their solvents with water in comparison with the case observed using low-polarity solvents. Moreover, no emission was observed with ethyl acetate, although it is immiscible with water. This is probably because the reaction of ethyl acetate with hydrogen peroxide was faster than the oxidation of bis(2,4,6-trichlorophenyl) oxalate. As a result, **DNSE** was not excited because 1,2-dioxetanedione was not produced.

4. Conclusion

We used betaine 30 and **DNSE** as solvatochromic molecules to investigate the dependence of chemiluminescence on solvent polarity. Although absorptions of betaine 30 were detected within 340–900 nm depending on the solvent polarity, the intensity of fluorescence was relatively low and chemiluminescence was not observed visually except for toluene. **DNSE** showed chemiluminescence with the solvents that are immiscible with water, producing several colors depending on the solvent polarity. It is possible that the lifetime of chemiluminescence in the solvents miscible with water is quite short and is not sufficient to visualize because the emission of **DNSE** in THF solution was observed only for a moment. Although it is necessary to optimize chemiluminescence conditions using solvatochromic molecules, we showed that it is possible to modify the chemiluminescence of dyes by varying the microenvironment.

References

1. C. Calvino, L. Neumann, C. Weder, and S. Schrettl, *J. Polym. Sci.,* **55** (2017) 640.
2. T. Ikeda, J. Mamiya, and Y. L. Yu, *Angew. Chem. Int. Ed.*, **46** (2007) 506.
3. X. Pang, J. Lv, C. Zhu, L. Qin, and Y. Yu, *Adv. Mater.*, **31** (2019) 1904224.
4. F. Ge, and Y. Zhao, *Adv. Funct. Mater.*, **30** (2020) 1901890.
5. B. R. Crenshaw, and C. Weder, *Chem. Mater.*, **15** (2003) 4717.
6. A. Pucci, M. Bertoldo, and S. Bronco, *Macromol. Rapid Commun.*, **26** (2005) 1043.
7. K. Imato, T. Kanehara, T. Ohishi, M. Nishihara, H. Yajima, M. Ito, A. Takahara, H. and H. Otsuka, *ACS Macro Lett.*, **4** (2015) 1307.
8. Y. Hu, K. Horie, H. Ushiki, F. Tsunomori, and T. Yamashita, *Macromolecules*, **25** (1992) 7324.
9. A. V. Kulinich, A. A. Ishchenko, G. V. Bulavko, and N. A. Davidenko, *Theor. Exp. Chem.*, **54** (2018) 178.
10. A. S. Klychenko, *Acc. Chem. Res.*, **50** (2017) 366.
11. B. Błasiak, C. H. Londergan, L. J. Webb, and M. Cho, *Acc. Chem. Rev.*, **50** (2017) 968.
12. C. Reus, and T. Baumgartner, *Dalton Trans.*, **45** (2016) 1850.
13. H. Cui, Z.-F. Zhang, M.-J. Shi, Y. Xu, and Y.-L. Wu, *Anal. Chem.*, **77** (2005) 6402.
14. M. Shamsipur, M. J. Chaichi, A. R. Karami, and H. Sharghi, *J. Photochem. Photobiol., A,* **174** (2005) 23.
15. M. Shamsipur, A. Yeganeh-Faal, M. J. Chaichi, M. Tajbakhsh, and A. Parach. *Dyes Pigm.*, **72** (2007) 113.
16. A. L. Pay, C. Kovash, and B. A. Logue, *J. Chem. Educ.*, **94** (2017) 1580.
17. B. R, Osterby, and R. D. McKelvey, *J. Chem. Educ.*, **73** (1996) 260.
18. S. A. Kovalenko, N. Eilers-König, T. A. Senyushkina, and N. P. Ernsting, *J. Phys. Chem. A*, **105** (2001) 4834.
19. K. Kumar, and A. K. Mishra, *Talanta*, **100** (2012) 414.
20. A. Miyagawa, J. Eng, T. Okada, Y. Inoue, T. J. Penfold, and G. Fukuhara, *ACS Omega*, **5** (2020) 897.
21. P. M. Page, C. A. Munson, and F. V. Bright, *Langmuir*, **20** (2004) 10507.
22. A. K. Tripathi, M. Mohapatra, and A. K. Mishra, *Phys. Chem. Chem. Phys.*, **17** (2015) 29985.
23. P. Wang, J. Wu, Y. An, and Y. Liao, *Spectrochim. Acta, Part A*, **220** (2019) 117140.
24. A. Choi, and S. C. Miller, *Org. Biomol. Chem.*, **15** (2017) 1346.
25. K. Naitoh, and T. Yamaoka, *J. Chem. Soc. Perkin Trans.* **2** (1992) 663.
26. The Chemical Society of Japan, "*Handbook of Chemistry: Pure Chemistry, 5th ed.*", Maruzen Publishing Co., Ltd., Tokyo, 2004, p. 770 (in Japanese).

Journal of Photopolymer Science and Technology
Volume 34, Number 4 (2021) 351−356 ©2021SPST

Analyses of Charge Accumulation of PTzBT Ternary Polymer Solar Cells Using ESR Spectroscopy

Dong Xue[1], Masahiko Saito[2], Itaru Osaka[2], and Kazuhiro Marumoto[1,3*]

[1] Division of Materials Science, University of Tsukuba, Tsukuba, Ibaraki 305-8573, Japan
[2] Graduate School of Advanced Science and Engineering, Hiroshima University, Higashihiroshima, Hiroshima, 739-8527, Japan
[3] Tsukuba Research Center for Energy Materials Science (TREMS), University of Tsukuba, Tsukuba, Ibaraki, 305-8571, Japan
**marumoto@ims.tsukuba.ac.jp*

Ternary polymer solar cells based on a polymer PTzBT have attracted attention because its power conversion efficiency (PCE) and thermal stability have been greatly improved by adding a small amount of an oligomer ITIC. However, the charge accumulation states of the PTzBT ternary polymer solar cells have not yet been completely clarified. Here, we report electron spin resonance (ESR) spectroscopy of layered samples of ZnO/(blend or pristine film) using PTzBT, ITIC, and a fullerene derivative $PC_{61}BM$ to investigate the charge accumulation states of the PTzBT ternary solar cells at a molecular level. We have observed monotonic increases in the ESR intensity of the ZnO/(blend or pristine film) samples under simulated solar irradiation, where the increases in the ESR intensity of the $PC_{61}BM$ with ITIC component are smaller than those without ITIC component. The present results would be useful to develop further highly efficient and durable polymer solar cells.

Keywords: Charge accumulation, Electron spin resonance spectroscopy, Ternary polymer solar cells, ITIC

1. Introduction

Polymer solar cells have been extensively investigated as they have characteristics such as low manufacturing cost, enabling large-area, and flexibility that are difficult to be realized with silicon-based solar cells [1–3]. In recent years, the power conversion efficiency (PCE) of ternary polymer solar cells has been remarkably improved [4]. However, the internal deterioration mechanism has not yet been completely clarified. Ternary polymer solar cells with a wide-band gap polymer based on thiophene and thiazolothiazole (PTzBT) (Fig. 1a) have attracted attention because the maximum PCE of the solar cells with PTzBT and [6,6]-phenyl C_{61}-butyric acid methyl ester ($PC_{61}BM$) have been improved from 7.4% to 10.3% by adding a small amount of ITIC (Fig. 1b). This ternary polymer solar cells with ITIC have excellent thermal stability that the PCE has almost not changed even after the storage at 85°C for 1000 h in a nitrogen-filled glove box under dark conditions under open-circuit conditions. Thus, the PTzBT solar cells are expected as polymer solar cells with high PCE and stability, and ITIC are expected as an ideal additive [5].

Sealing solar cells can suppress the extrinsic irreversible degradations from oxygen and moisture [6−12]. However, there is still some internal deterioration factors that cannot be prevented such as charge accumulation. Electron spin resonance (ESR) spectroscopy is a useful method that can directly investigate the states of accumulated charges in polymer solar cells and organic solar-cell materials at a molecular level [13−23]. It is very interesting to investigate the charge accumulation in PTzBT ternary polymer solar cells with ITIC.

In this study, we have measured layered samples of the active layer and an electron transport layer (ETL) ZnO using light-induced ESR spectroscopy, and have found some differences of the ESR signals between the samples of ZnO/PTzBT:ITIC:$PC_{61}BM$ and ZnO/PTzBT:$PC_{61}BM$. We conducted a further study by measuring layered samples of ZnO/ITIC:$PC_{61}BM$ and ZnO/$PC_{61}BM$. We have

Received March 31, 2021
Accepted April 22, 2021

observed several signals and monotonic increases in the ESR intensities of all the ZnO layered samples. The ESR signal of $PC_{61}BM$ electron (or radical anion), namely, the electron signal of $PC_{61}BM$, is observed and the signal increase in the ESR intensity of $PC_{61}BM$ with ITIC component is smaller than that without ITIC. This deep understanding of the charge accumulation states would be important for optimizing the device structures and for improving the PCE and durability of ternary polymer solar cells.

2. Experimental

In the present work, the ternary polymer solar cells were fabricated with PTzBT, ITIC (Fig. 1b), and $PC_{61}BM$ (Solenne BV, purity > 99.5%). A quartz substrate (20 mm × 3 mm) was cleaned with acetone and 2-propanol in ultrasonic treatment. A ZnO layer was prepared by a spin-coating method (at 1500 rpm) from a diluted solution of ZnO nanoparticles. PTzBT, ITIC, and $PC_{61}BM$ (1:0.2:2 w/w/w) dissolved in chlorobenzene (CB) solvent was mixed at 100 °C for 30 min with a vibrational method. Active layers (PTzBT:ITIC:$PC_{61}BM$ or PTzBT:$PC_{61}BM$) were fabricated by a spin-coating method (600 rpm, 20 s) on the quartz substrate in a nitrogen-filled glove box (O_2 < 0.2 ppm, H_2O < 0.5 ppm). The fabricated samples were measured under dark conditions or simulated solar irradiation with a solar simulator (AM1.5G, 100 mW cm^{-2}) (OTENTOSUN-150LX).

3. Results and discussion

3.1. ESR measurements

ESR is a magnetic resonance phenomenon occurring for unpaired electrons, which is a non-destructive and highly sensitive method that can evaluate materials at the molecular level by observing the microwave absorption at the magnetic resonance. We used a continuous-wave ESR method in the experiments which performs a lock-in detection with an external magnetic field (H) modulation of 100 kHz. Thus, photogenerated charges with a lifetime (<10 μs) cannot be observed, and it is possible to observe only long-lived (or accumulated) photogenerated charges with an unpaired spin with a long lifetime (>10 μs) in thin films and solar cells [19, 21−23].

We simultaneously measured the ESR signals of our sample and a same standard Mn^{2+} marker sample in a same ESR cavity in all ESR measurements in order to compare these g factors directly. The calibration of the g factor was

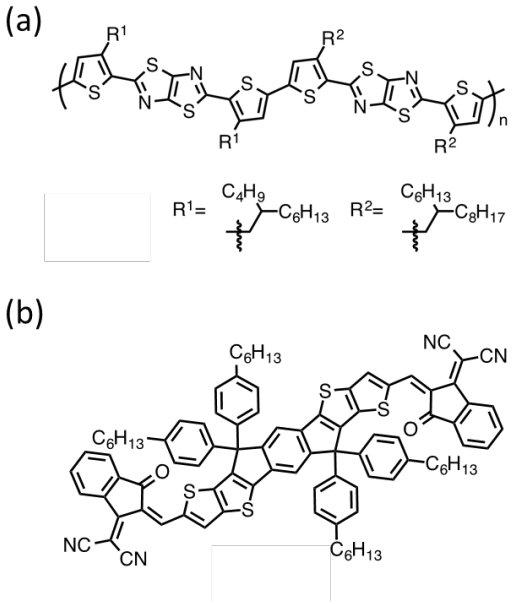

Fig. 1. Chemical structures of (a) PTzBT and (b) ITIC.

performed by using a software program of the ESR system considering high second-order correction of the effective resonance field. Its correctness was also confirmed by using 2,2-diphenyl-1-picrylhydrazyl (DPPH) as another standard sample. The present ESR system significantly reduces experimental errors because the fluctuation of experimental conditions such as microwave power etc. can be calibrated by using the signal of the marker sample [19, 21−23].

By using ESR measurements, it is possible to investigate accumulated charge states in the samples directly. The light-induced ESR spectrum is a difference spectrum between ESR spectra obtained from under dark condition and simulated solar irradiation. We can study the effect of the irradiation for the samples. In our study, the substrate plane was

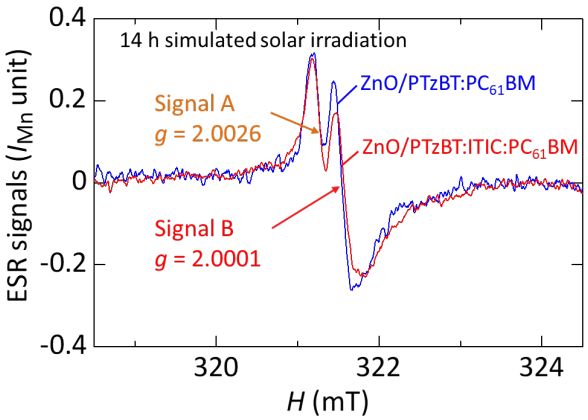

Fig. 2. ESR signals of ZnO/PTzBT:ITIC:$PC_{61}BM$ (red line) and ZnO/PTzBT:$PC_{61}BM$ (blue line) after 14 h simulated solar irradiation at room temperature.

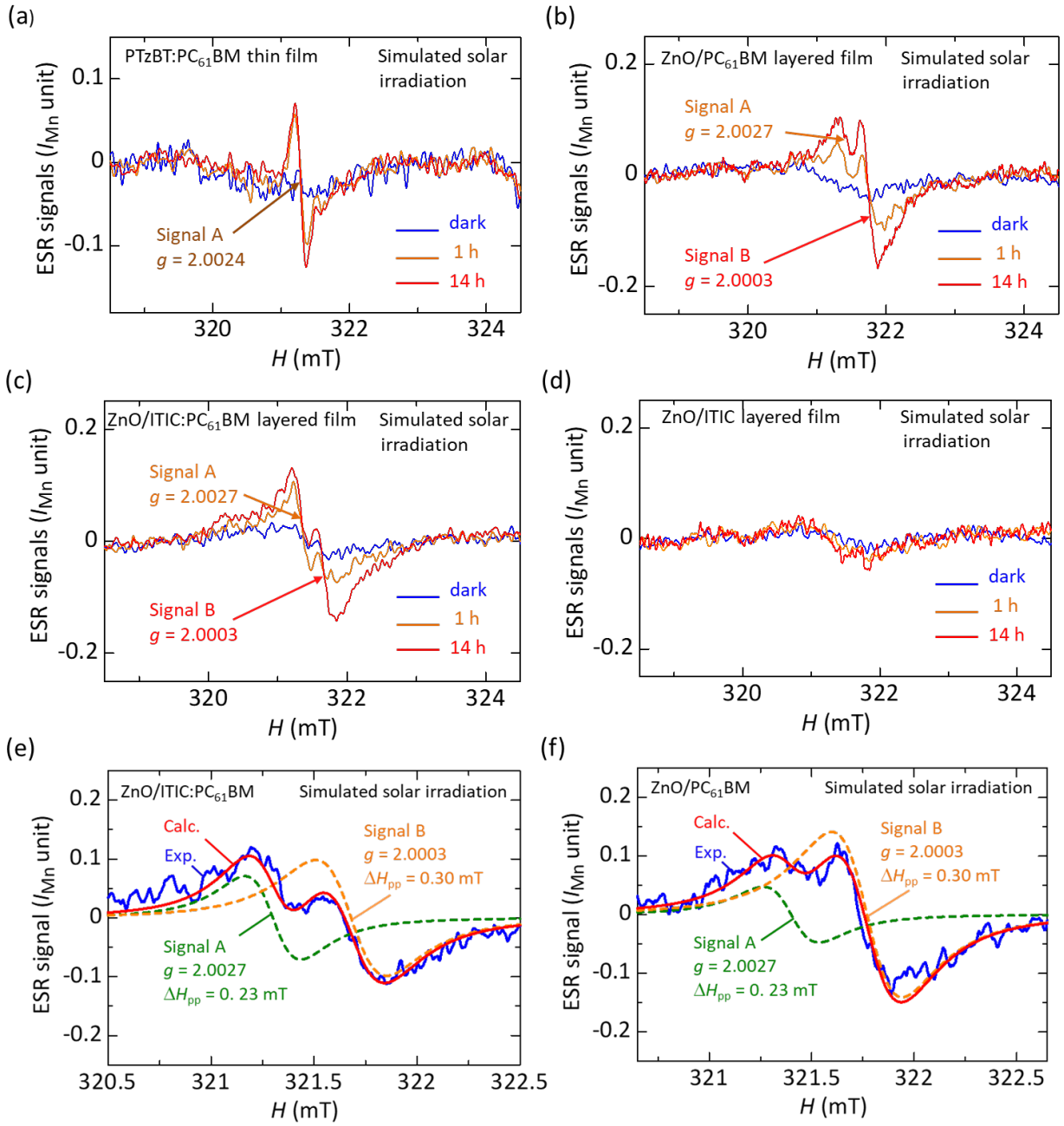

Fig. 3. Time variation of ESR spectra of layered samples of (a) PTzBT:$PC_{61}BM$, (b) ZnO/$PC_{61}BM$, (c) ZnO/ITIC:$PC_{61}BM$, and (d) ZnO/ITIC under simulated solar irradiation at room temperature. Fitting analyses for the light-induced ESR signals of layered samples of (e) ZnO/ITIC:$PC_{61}BM$ and (f) ZnO/$PC_{61}BM$.

parallel to the H direction. All measured light-induced ESR spectra were averaged over 1 h irradiation [19, 21−23].

3.2. ESR spectra of layered samples

Investigating the effect of ITIC addition on charge accumulation is a very interesting issue to clarify the internal deterioration mechanism of the ternary polymer solar cells. For this purpose, layered samples of ZnO with PTzBT:ITIC:$PC_{61}BM$ or PTzBT:$PC_{61}BM$ have been fabricated and measured using ESR spectroscopy. Fig. 2 shows the ESR spectra of the layered samples after 14 h simulated solar irradiation. According to Fig. 2, whether or not ITIC has been used, apparent two signals have been observed. We define the signal on the left as Signal A, and the signal on the right as Signal B, respectively. The g factors of the Signal A and Signal B are obtained as $g = 2.0026 \pm 0.0004$ and $g = 2.0001 \pm 0.0004$, respectively.

In order to find out the origins of ESR signals, layered samples of PTzBT:$PC_{61}BM$, ZnO/$PC_{61}BM$,

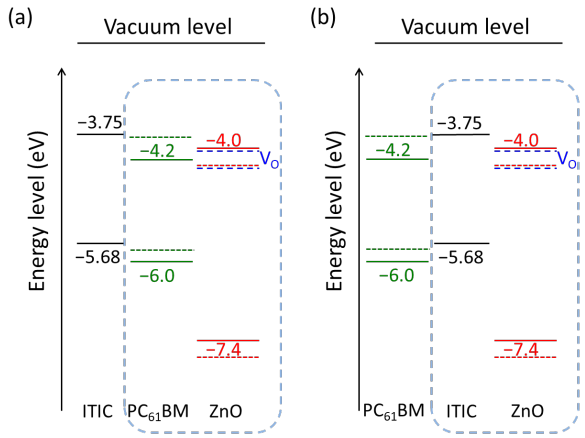

Fig. 4. Two cases of energy diagrams of the ZnO/ITIC:$PC_{61}BM$ layered sample. (a) $PC_{61}BM$ (green line) and (b) ITIC (black line) contact with ZnO (red line). The broken line shows the energy level of V_O (blue line) in ZnO. The dotted lines show the variation of energy levels of $PC_{61}BM$ (green line) and ZnO (red line).

ZnO/ITIC:$PC_{61}BM$, and ZnO/ITIC were fabricated and measured using ESR spectroscopy. The observed ESR spectra are shown in Fig. 3a,b,c,d, respectively. As the duration of the light irradiation increased, the intensity of the ESR signals in Fig. 3a,b,c increased, while the ESR intensity in Fig. 3d was almost constant. The ESR signal of Fig. 3a is identified as a hole signal of PTzBT because the spin-lattice relaxation time of $PC_{61}BM$ is so short that the ESR signal of $PC_{61}BM$ cannot be observed at room temperature [21−23]. The g factor of holes in PTzBT is identified as $g = 2.0024\pm0.0004$. When measuring the ESR signals of ZnO/$PC_{61}BM$ (Fig. 3b) and ZnO/ITIC:$PC_{61}BM$ (Fig. 3c), we observed same signals of two components with their g factors $g = 2.0027\pm0.0004$ and $g = 2.0003\pm0.0004$, respectively. The observed signals of ZnO/$PC_{61}BM$ (Fig. 3b) and ZnO/ITIC:$PC_{61}BM$ (Fig. 3c) are almost the same as those of ZnO/PTzBT:ITIC:$PC_{61}BM$ and ZnO/PTzBT:$PC_{61}BM$ (Fig. 2), whose g factors are $g = 2.0026$ (Signal A) and $g = 2.0001$ (Signal B) as mentioned above. The ESR signal of $g = 2.0027$ has been reported as the signal of a singly positively charged oxygen vacancy (V_O^+) in ZnO [24,25]. The ESR signal of $g = 2.0003$ has been reported as the electron signal of $PC_{61}BM$ [21−23].

In order to get more accurate component signal, we performed fitting analyses for the light-induced ESR signals of ZnO/$PC_{61}BM$ (Fig. 3b) and ZnO/ITIC:$PC_{61}BM$ (Fig. 3c) after 14 h light irradiation, and the calculated results are shown in Fig. 3f and 3e, respectively. In previous studies, the

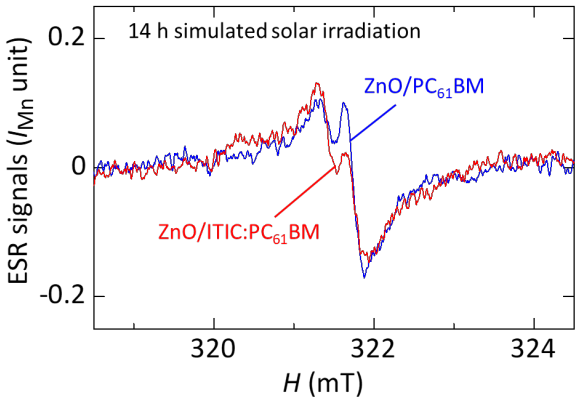

Fig. 5. ESR spectra of ZnO/ITIC:$PC_{61}BM$ (red line) and ZnO/$PC_{61}BM$ (blue line) after 14 h simulated solar irradiation at room temperature.

electron signal of $PC_{61}BM$ with an anisotropic lineshape have been observed at low temperatures such as 30 K [26]. However, the molecular vibrations are large and the electron signal of $PC_{61}BM$ is averaged at room temperature. The isotropic electron signal of $PC_{61}BM$ and the isotropic hole signal of V_O^+ in ZnO have been reported by previous studies at room temperature [24,27]. Thus, we have fitted the light-induced ESR signals of ZnO/ITIC:$PC_{61}BM$ and ZnO/$PC_{61}BM$ at room temperature using isotropic signals, and found that the best result can be described using the sum of two Lorentzian functions. The results of the fitting analyses are evaluated as follows: ESR parameters of Signal A are g factor $g = 2.0027\pm0.0004$, peak-to-peak ESR linewidth $\Delta H_{pp} = 0.23\pm0.02$ mT, and ESR parameters of Signal B are $g = 2.0003\pm0.0004$, $\Delta H_{pp} = 0.30\pm0.02$ mT. Thus, the Signal A ($g = 2.0026$) is identified to be composed of both the hole signals of PTzBT ($g = 2.0024$) and ZnO ($g = 2.0027$), and the Signal B ($g = 2.0001$) is identified to be due to the electron signal of $PC_{61}BM$ ($g = 2.0003$). It is worth noting that the electron signal of $PC_{61}BM$, which have not been observed with the active layer thin films at room temperature because of the short spin-lattice relaxation time due to the rotation of wave function of electrons on $PC_{61}BM$ [21−23], has been observed when we have measured ZnO/$PC_{61}BM$ (Fig. 3b) and ZnO/ITIC:$PC_{61}BM$ (Fig. 3c). The observation of the Signal B indicates the interactions between ZnO and $PC_{61}BM$ electrons with a strong spin-orbital interaction due to a heavy element Zn in the ZnO layer. Compared to the previous study, our observed g factor of $PC_{61}BM$ is slightly larger because the heavy element Zn is effective in shifting the g factor [28].

3.3. Effect of ITIC addition.

Schematic energy level diagrams of ZnO, ITIC, and $PC_{61}BM$ are shown in Fig. 4. The values of energy levels are taken from previous studies [29-33]. The energy levels of valence band (VB) top and conduction band (CB) bottom of ZnO have been reported as a range of −7.4 ~ −7.7 eV and −4.0 ~ −4.3 eV, respectively [29-31]. The energy levels of highest occupied molecular orbital (HOMO) and lowest unoccupied molecular orbital (LUMO) of $PC_{61}BM$ have been reported as a range of −6.0 ~ −6.2 eV and −3.8 ~ −4.2 eV, respectively [30-33]. The energy level of the oxygen vacancy V_O is −0.05 eV deeper than the CB bottom of ZnO [29]. Normally, the electrons are transferred from $PC_{61}BM$ to ZnO. However, our present ESR results indicate that the electrons are transferred from ZnO to $PC_{61}BM$. In the case of ZnO/$PC_{61}BM$ (Fig. 3b), the electron signal of $PC_{61}BM$ and the hole signal of V_O^+ are observed. We infer that the the LUMO of $PC_{61}BM$ may be deeper than the energy level of the V_O, and thus electrons can transfer from the V_O in ZnO to the LUMO of $PC_{61}BM$. The bandgap energy of ITIC calculated by the difference between HOMO and LUMO energy levels, which have been determined by photon yield spectroscopy and low-energy photoemission spectroscopy, respectively, is 2 eV [5]. This is actually different from the value determined by optical absorption onset of ITIC (1.59 eV) [5]. Such difference originates in the exciton binding energy and is typical to π-conjugated organic materials [34].

It is interesting to find out the effect of the ITIC addition by comparing the ESR spectra of ZnO/$PC_{61}BM$ (Fig. 3b) and ZnO/ITIC:$PC_{61}BM$ (Fig. 3c) after 14 h simulated solar irradiation. The compared ESR spectra are shown in Fig. 5. It is worth noting that the intensity of the Signal B with ITIC is weaker than that without ITIC (see Fig. 2 and 5). The reason may be that some of ITIC molecules prevent the contacts between the ZnO layer and $PC_{61}BM$ molecules (see Fig. 4b), and thus some electrons' signal of $PC_{61}BM$ cannot be observed because of the short spin-lattice relaxation time of $PC_{61}BM$ without contacting ZnO at room temperature as mentioned above [21−23,26]. From our ESR study, we suggest that $PC_{61}BM$ and ITIC are mixed, and both are in contact with the ZnO layer. Our clarification of the charge accumulation at the interface between the ZnO and active layers would be important for improving the PCE and durability of ternary polymer solar cells.

4. Conclusion

The layered samples of ZnO/PTzBT:ITIC:$PC_{61}BM$ and PTzBT:$PC_{61}BM$ have been investigated with ESR spectroscopy under dark conditions and simulated solar irradiation. As the duration of the light irradiation increased, the intensities of the hole signal of PTzBT, the hole signal of ZnO, and the electron signal of $PC_{61}BM$ increased. The observation of the electron signal of $PC_{61}BM$ indicates the interactions between ZnO and $PC_{61}BM$ electrons with the strong spin-orbital interactions due to the heavy element Zn in the ZnO layer. The electron signal of $PC_{61}BM$ with ITIC are smaller than that without ITIC under simulated solar irradiation. The reason may be that some of ITIC molecules prevent the contacts between the ZnO layer and $PC_{61}BM$ molecules, and thus some electrons' signal of $PC_{61}BM$ cannot be observed. This deep understanding of the charge accumulation states at the interface between the ZnO and active layers of ternary polymer solar cells will be useful for optimizing the device structures and for improving the PCE and durability.

Acknowledgement

This work was partially supported by JSPS KAKENHI Grant Number JP19K21955, by JST PRESTO, by The Hitachi Global Foundation, by The MIKIYA Science And Technology Foundation, by Iketani Science and Technology Foundation, and by JST ALCA Grant Number JPMJAL1603, Japan.

References

1. S. Günes, H. Neugebauer, and N. S. Sariciftci, cells, *Chem. Rev.*, **107** (2007) 1324–1338.
2. T. M. Clarke and J. R. Durrant, *Chem. Rev.*, **110** (2010) 6736–6767.
3. R. Søndergaard, M. Hösel, D. Angmo, T. T. Larsen-Olsen, and F. C. Krebs, *Mater. Today*, **15** (2012) 36–49.
4. Q. An *et al.*, *Sci. Bull.*, **65** (2020) 538–545.
5. M. Saito, Y. Tamai, H. Ichikawa, H. Yoshida, D. Yokoyama, H. Ohkita, and I. Osaka, *Macromolecules*, **53** (2020) 10623–10635.
6. C. Y. Chang, C. T. Chou, Y. J. Lee, M. J. Chen, and F. Y. Tsai, *Org. Electron.*, **10** (2009) 1300–1306.
7. S. Sarkar, J. H. Culp, J. T. Whyland, M. Garvan, and V. Misra, *Org. Electron.*, **11** (2010) 1896–1900.
8. M. Hermenau, S. Schubert, H. Klumbies, J. Fahlteich, and L. Müller-Meskamp, *Sol. Energy Mater. Sol. Cells*, **97** (2012) 102–108.
9. H. J. Lee, H. P. Kim, H. M. Kim, J. H. Youn,

D. H. Nam, Y. G. Lee, J. G. Lee, A. R. Bin Mohd Yusoff, and J. Jang, *Sol. Energy Mater. Sol. Cells*, **111** (2013) 97–101.
10. M. D. Clark, M. L. Jespersen, R. J. Patel, and B. J. Leever, *Org. Electron.,* **15** (2014) 1–8.
11. T. M. Abdel-Fattah, E. M. Younes, G. Namkoong, E. M. El-Maghraby, A. H. Elsayed, and A. H. Abo Elazm, *Synth. Met.*, **209** (2015) 348–354.
12. A. Singh, A. Dey, D. Das, and P. K. Iyer, *ACS Appl. Mater. Interfaces*, **8** (2016) 10904–10910.
13. K. Marumoto, S. Kuroda, T. Takenobu, and Y. Iwasa, *Phys. Rev. Lett.*, **97** (2006) 256603.
14. K. Marumoto, N. Arai, H. Goto, M. Kijima, K. Murakami, Y. Tominari, J. Takeya, Y. Shimoi, H. Tanaka, S. Kuroda, T. Kaji, T. Nishikawa, T. Takenobu, and Y. Iwasa, *Phys. Rev. B*, **83** (2011) 075302.
15. T. Nagamori and K. Marumoto, *Adv. Mater.*, **25** (2013) 2362–2367.
16. T. Biskup, M. Sommer, S. Rein, D. L. Meyer, M. Kohlstädt, U. Würfel, and S. Weber, *Angew. Chem. Int. Ed.*, **210** (2015) 148–155.
17. D. Son, T. Kuwabara, K. Takahashi, and K. Marumoto, *Appl. Phys. Lett.*, **109** (2016) 4963285.
18. G. Sato, D. Son, T. Ito, F. Osawa, Y. Cho, and K. Marumoto, *Phys. Status Solidi A*, **215** (2018) 1700731.
19. T. Kubodera, M. Yabusaki, V.A.S.A. Rachmat, Y. Cho, T. Yamanari, Y. Yoshida, N. Kobayashi, and K. Marumoto, *ACS Appl. Mater. Interfaces*, **10** (2018) 26434–26442.
20. Y. Kobori, T. Ako, S. Oyama, T. Tachikawa, and K. Marumoto, *J. Phys. Chem. C*, **123** (2019) 13472–13481.
21. V. A. S. A. Rachmat, T. Kubodera, D. Son, Y. Cho, and K. Marumoto, *ACS Appl. Mater. Interfaces*, **11** (2019) 31129–31138.
22. D. Xue, S. Kamiya, M. Saito, I. Osaka, and K. Marumoto, *ACS Appl. Energy Mater.*, **3** (2020) 2028–2036.
23. D. Xue, S. Kamiya, M. Saito, I. Osaka, and K. Marumoto, *J. Photopolym. Sci. Technol.*, **33** (2020) 97–102.
24. M. Zhang, F. Averseng, F. Haque, P. Borghetti, J. Krafft1, B. Baptiste, G. Costentin, and S. Stankic, *Nanoscale*, **11** (2019) 5102-5115.
25. M. Zhang, F. Averseng, J. Krafft, P. Borghetti, G. Costentin, and S. Stankic, *J. Phys. Chem. C*, **124** (2020) 12696–12704.
26. O. G. Poluektov, S. Filippone, N. Martın, A. Sperlich, C. Deibel, and V. Dyakonov, *J. Phys. Chem. B*, **114** (2010) 14426–14429.
27. C. Y. Chang, W. K. Huang, Y. C. Chang, and K. T. Lee, *J. Mater. Chem. A*, **4** (2016) 640–648.
28. D. Liu, T. Nagamori, M. Yabusaki, T. Yasuda, L. Han, and K. Marumoto, *Appl. Phys. Lett.*, **104** (2014) 243903.
29. L. Schmidt-Mende and J. L. MacManus-Driscoll, *Mater. Today*, **10** (2007) 40–48.
30. F. Yang, D. W. Kang, and Y. S. Kim, *Solar Energy*, **155** (2017) 552–560.
31. J. C. Yu, J. A Hong1 E. D. Jung, D. B. Kim, S. M. Baek, S. Lee, S. Cho, S. S. Park, K. J. Choi, and M. H. Song, *Sci. Rep.*, **8** (2018) 1070.
32. Y. Wang, J. Chen, H. D. Kim, B. Wang, R. Iriguchi, and H. Ohkita, *Front. Energy Res.*, **6** (2018) 113.
33. T. Nakamura, S. Yakumaru, M. A. Truong, K. Kim, J. Liu, S. Hu, K. Otsuka, R. Hashimoto, R. Murdey, T. Sasamori, H. D. Kim, H. Ohkita, T. Handa, Y. Kanemitsu, and A. Wakamiya, *Nat.Commun.*, **11** (2020) 3008.
34. J. L. Bredas, *Mater. Horiz.*, **1** (2014) 17-19.

Review

Journal of Photopolymer Science and Technology
Volume 34, Number 4 (2021) 357−362 ©2021SPST

A Study On Ant Colony Optimization

Tomohisa Takimi[1*]

[1] *Digital Strategy Department, Yamato Holdings Co., Ltd,*
19F, 1-2, 2-Chome, Kyobashi, Chuo-ku, Tokyo 104-0031, Japan
**tomohisa.takimi@kuronekoyamato.co.jp*

Biomimetics is attracting more and more attention as a powerful clue to cutting-edge breakthroughs in a lot of areas. Of course, it is so powerful not only for material science but also for the areas of social infrastructure such as transportation. I would like to review an example of Biomimetics in transportation, which is called as ant colony optimization (ACO), thoroughly studied in the area of mathematical optimization.
Keywords: Biomimetics, Mathematical Optimization, Transportation

1. Introduction

Sometimes, Biomimetics might be regarded as a subarea of material science due to enthusiastic activities in the area. Such active studies began with remarkable achievements with powerful electron microscopes. However, Biomimetics should not be limited to material science. It could be applied to almost all areas of human activities, as we can confirm through a lot of wisdom referring to animals' activities etc. Of course, it can be applied to the area of transportation. From the standpoint of material science also, it would be meaningful to study on transportation because the transportation area would be one of the most active playgrounds of the IoT and smart technologies.

In this occasion, we would like to introduce an example of Biomimetics applied to the mathematical optimization on transportation. In the area of transportation, a lot of studies are devoted to the mathematical optimization such as routing problems to search for an efficient way of management. Such studies would bring not only cost-effective management but also less carbon emission. In this article, we would like to explain the ant colony optimization which is a powerful calculation method for routing problems.

The aim of routing problems is to find out the shortest path for delivery visiting all customers. One might naively speculate that it would be so easy since a human being unintentionally thinks of an efficient path to visit all necessary locations in daily life. However, it is not so simple as one might speculate. Suppose that there are 50 locations to be visited for delivery, if one tries to find out the shortest path by assessing all patterns of location orders, it is required to probe 50! ~ 10^{64} patterns. This is a too tremendous number to work out within allowable time in practical usage. Even if a pattern can be evaluated by one operation in the current fastest computer (420 PFLOPS), it takes more than 10^{39} years. This duration is much longer than universe age (around 10^{10} years), then it is completely impossible. On the other hand, it is usual to visit more than 50 locations in daily delivery jobs, therefore we need to devise computational methods to find out the efficient way. This is one of the missions of mathematical optimization.

To devise methods, it could be natural to refer to efficient animals' activities. It has been known that ants take the shortest route to return to colony after obtaining their feeds. Inspired by this nature, M. Dorigo suggested a remarkable method so-called "ant colony optimization" (ACO) [1] in 1992. Following him, there are a lot of studies based on this ant colony optimization [2-13]. We will explain the ant colony optimization. Since human being is also one of animals, it could suite human behavior also.

2. Ants' behavior to return to their colony

It would be well known that ants form a walking line along the shortest path between the colony and their destination, on which their feeds are often located. This chapter is devoted to the explanation

Received March 22, 2021
Accepted April 19, 2021

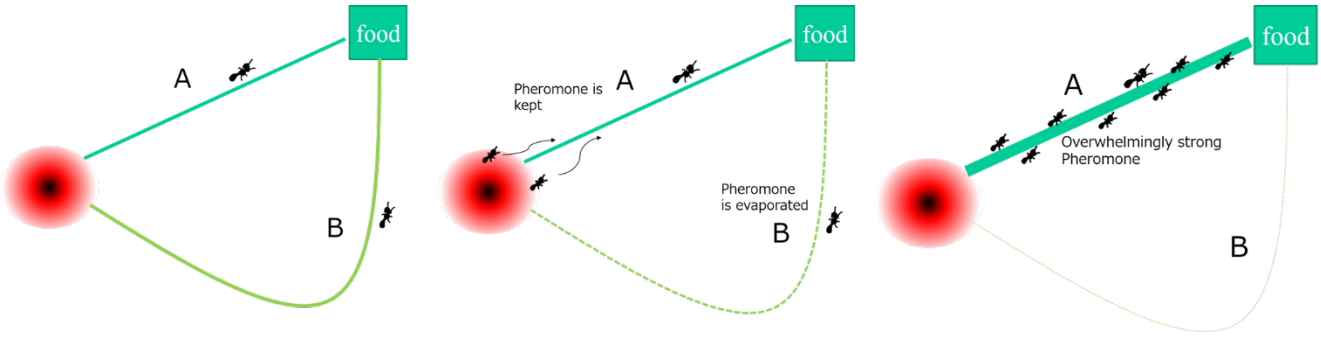

Fig. 1. (Left) Two ants arrived at the same food at the same time, but A's route is shorter than B's.
(Center) Pheromone on B's route becomes weaker while A's one is kept strong
(Right) Pheromone on the B's route is almost disappeared and only A's one survives

of a mechanism to form the line with the shortest path. Ref. [14] would be a famous paper on the ants' behavior. Since the ants live under the ground, they do not have a strong ability to see the environment through light. Alternately they rely on the sense related to the smell. Although ants initially wander randomly outside the colony with dropping the pheromone, upon once finding their feed, they return to the colony guided by the pheromone laid down along the path to the colony. Ants tend to be attracted to the pheromone line, probed by their sense of smell. This pheromone plays a role of signal of safe path, since it could be an evidence that precedent ants passed along. It is important that pheromone has strong volatility, then the ants can feel it.

Here let us see how the walking line is formed. Suppose that there are two ants, A and B, the two arrived at the target food at the same time, and the length of the ant A's route is much shorter than the ant B's one (Fig. 1. Left). In this case, since the pheromone on the B's route would be exposed for longer time, due to the strong volatility of pheromone, ant B's route would lose more pheromone than the A's route. Then subsequent ants are attracted to A's route more than B's route due to the stronger pheromone. Moreover, the subsequent ones would put additional pheromone on the A's route, while the pheromone on the B's route is vapored only without sufficient addition (Fig. 1. Center). Then the pheromone on the A's route becomes relatively stronger and stronger than the one on the B's route. B's route would be gradually excluded from the options for subsequent ants, and then only A's route would remain as the unique route connecting the food and the colony (Fig. 1. Right). Due to this mechanism, only the shortest path is kept, we can see that the ant walking line indicates the shortest path.

3. Ant colony optimization algorithm

Inspired by the above nature, the ant colony optimization algorithm, which is explained in this chapter, was developed.

3.1. Setup

For the efficient routing path for daily delivery jobs, it is required to consider the route visiting all locations to be delivered. Here symbol D denotes the set of the locations to be delivered. For each pair of locations denoted by $i, j \in D$, the distance between these two is described as d_{ij}. In the algorithm, not only distances but also "pheromone" which attracts the deliverers are considered. We describe the quantity of the pheromone put on the road between $i \in D$ and $j \in D$ as τ_{ij}. Here the deliverers start from the point s and after visiting all location to deriver, they return to the starting point.

3.2. Calculation procedure

3.2.1. Decision probability for selecting next visiting location

First of all, it is necessary to set up the procedure to decide the first visiting point. Inspired by the ants' behavior, it is natural to set up the probability for choosing the point depending on the quantity of the pheromone. Among the locations, the probability to choose $k \in D$ is described as

$$P_{sk} = \frac{{\tau^{\alpha}}_{sk} / {d^{\beta}}_{sk}}{\sum_{i \in D} {\tau^{\alpha}}_{si} / {d^{\beta}}_{si}} \quad (1).$$

Here, the exponent α, β are parameters which can be set according to the preference. This shows the tendency to select a location with a shorter route and stronger pheromone. After arriving at the point k, the deliverer should visit a

location which has not been visited yet. If the set of the unvisited point is denoted as U, the probability to visit the point $i \in U$ next to the present location k is described similarly as

$$P_{ki} = \frac{\tau_{ki}^{\alpha} / d_{ki}^{\beta}}{\sum_{j \in U} \tau_{kj}^{\alpha} / d_{kj}^{\beta}} \quad (2).$$

Since all the points are unvisited at the beginning, $D = U$, equation (2) results to equation (1) at the starting. Until the deliverer visits all the required points and returns to the starting point, a deliverer keeps selecting a next visiting point according to the probability described in equation (2). After finishing the sequence of the selecting, pheromone would be updated by the procedure explained in the next section, and after that the same calculation would be restarted from equation (1).

We should note that equations (1) and (2) just provide the probability, hence it is not ensured to reproduce the same result. One might wonder that this procedure might provide so random results which might not be reliable. However, thanks to the updating process of the pheromone explained in the following section, we can expect that this algorithm surely provides solutions with shorter routes which we pursue.

3.2.2. Pheromone update

Evaporation and addition process of the pheromone plays a central role in the mechanism of forming ants' line with the shortest length. Therefore, it is natural to include the process in the algorithm. In the ant colony optimization, the pheromone update is usually executed after visiting all required locations. Suppose that the pheromone before the update is denoted as τ_{ij}^{old}, updated pheromone τ_{ij}^{new} is calculated as

$$\tau_{ij}^{new} = (1-\rho)\tau_{ij}^{old} + \Delta\tau_{ij} \quad (3).$$

Here ρ $(0 \le \rho \le 1)$ denotes the evaporation ratio and the first term becomes residue of old pheromone. The second term $\Delta\tau_{ij}$ is the pheromone added by ants which passed through the route between $i \in D$ and $j \in D$. Of course, $\Delta\tau_{ij}$ becomes zero if the ant did not pass through the route. Suppose that the closed path of the ant is denoted by c, and the length of the path is X_c, the nonzero case of the $\Delta\tau_{ij}$ is usually given as ξ / X_c, with some constant coefficient ξ. We should note that the quantity is inversely proportional to the length of the closed route X_c, then a shorter route would append stronger pheromone which is more attracting.

It would deserve to note that equations (1) and (2) refer only to the very local information of places connected to the current location of the deliverer. So, this means that both the equations do not overlook the nature of the whole part of the closed path. Hence it would not be ensured to enforce to choose the shortest path only by equations (1) and (2), then it would be necessary to include the information of the whole part of the path. Here equation (3) would compensate for such lack of information. Equation (3) plays a role to set a proper bias on probability gradually enforcing deliverer to select the shorter path. Once a short path is chosen, the pheromone quantity to be added ξ / X_c is large enough and it can be so powerful bias for the short path to dominate the relative probability weight. On the other hand, suppose that the inadequate path is chosen, the quantity of the added pheromone is not so big, and hence there is still a chance to escape from selecting the wrong answer.

3.2.3. Pheromone reset

As explained in equations (1) and (2), the calculation procedure is stochastic. Hence it is not perfectly ensured to derive the proper optimized solution. Once the wrong answer is selected, due to the pheromone updating process, the probability to choose the wrong answer could be dominating. Then only the wrong answer is focused due to the pheromone allocated inadequately. To resolve this biased situation, it is necessary to reset the pheromone distribution. The following quantity, so-called the convergence factor, is often used to evaluate the degree of the localization of pheromone distribution,

$$cf = 2\left(\frac{\sum_{i,j \in D} \max(\tau_{\max} - \tau_{ij}, \tau_{ij} - \tau_{\min})}{|\tau|\,|\tau_{\max} - \tau_{\min}|} - 0.5 \right) \quad (4).$$

Here,

$$\tau_{\max} = \max_{i,j \in D}(\tau_{ij}), \quad \tau_{\min} = \min_{i,j \in D}(\tau_{ij}) \quad (5),$$

and $|\tau|$ is the number of connecting routes between two locations of delivery points D. It

is often asserted that the pheromone distribution is too biased if $cf > 0.99$, and pheromone distribution is reset to be initial. In the following experiments also, we use this level to judge whether the pheromone distribution is too biased or not.

3.3. The number of ants

It is natural to set multiple ants in the calculation, since it is a consequence of swarm intelligence. Compared with the single ant case, it is usual to get better results since the effect of the pheromone becomes more effective. Even if an ant passed through an improper route, as long as the other ants go through a much better route, it is easy to recover the defect by the stronger pheromone on the shorter route. We can also see this effect in the experiments in the next section.

4. Experiments to observe the reliability of this stochastic calculation

Here we will demonstrate how the above updating and resetting procedure of the pheromone works well to obtain solutions with short length. As a problem instance, we prepared eil51 [15] in the TSPLIB. The TSPLIB [16] is the library of the sample instances for the traveling salesman problem, which can be accessed via the internet. The shortest length of the optimal solution of the instance is known to be 426, which was obtained by some refined methods. Let us compare the three kinds of calculations, (i) calculation by full-fledged ACO, (ii) calculation by ACO without pheromone reset, (iii) almost random calculation without both the pheromone reset and update, at which the pheromone does not help anything. The parameters and the setup are summarized in Table. 1. In this setup, we obtain the result described in Table. 2.

Table 1. Parameters in the calculation

α	(i),(ii) 1.2 (iii) 0.0
β	1.0
ρ	0.5
Number of Ants	7
Iteration number of calculation	10000
Number of implementing pheromone reset	(i)100 (ii),(iii) 0
ξ	2.0
Program Language	Java

Table 2. Results of the calculation

(i) Full-fledged ACO	477
(ii)ACO without reset	514
(iii)No pheromone	937

The full-fledged ACO result (i) is the closest to the optimized result. Calculation (i) and (ii) get much shorter length than (iii), hence we can see that the pheromone update is significant to get a good result. The updating seems to work well for making ants concentrate on the shorter route. Compare the result (i) with (ii), we can also see that the pheromone reset procedure is working well to obtain shorter routes. Actually, in these calculations, we set up the parameters very roughly. Even in this rough set-up, the result (i) looks close to the best-known result of the instance. Hence ACO could be reliable, although the method employs stochastic calculation.

It would be also interesting to compare with the calculation with a single ant. In these calculations, only the number of ants is changed to 1. The results are described in Table 3.

Table 3. Result of the calculation in the case of single ant

(i) Full-fledged ACO	853
(ii)ACO without reset	1021
(iii)No pheromone	991

It is remarkable that the results in (i) and (ii) are terribly disimproved. The result of (iii) is not so changed from the one in Table 2. From these, we can see that the number of ants would affect the pheromone effects so much. Moreover, the result of (ii) got even worse than the result (iii). Although the pheromone is expected to attract the ants to the short route, once the pheromone is put on the improper route, it becomes a nuisance confining the ants within an improper path. If there are multiple ants, even if one ant takes a mistake, such mistake can be easily smeared out if the other ants put their more attractive pheromone on the proper route. However, if there is only one ant, if the ant takes a mistake, it would be impossible to smear out the mistake since the pheromone can be added only on the improper route. So, the pheromone could sometimes lead to the worse result if we use it in an improper way. This result could imply the significance of the diversity of the ants.

5. Comment on the ant colony and comparison with other algorithms

In equations (1) and (2), if we choose the nearest location as the next visiting point, in a deterministic way, it would come down to be a greedy algorithm. Although, in some classes of the problems, a greedy algorithm is proven to provide the optimized solution, it is not the case in the routing problems. Once we choose a starting point in a deterministic algorithm, the whole order of the visiting points is

totally determined and is not ensured to be optimal. In a usual routing problem, it is often specified the starting point without taking into account the nature of the whole part of the route network. Hence it is important to deviate from a rut of the deterministic method. One powerful option would be employing a stochastic method, and the ant colony optimization is one of them. One might wonder that the stochastic calculation would not surely provide the optimal solution. Although as we already confirmed by the above experiment, we can expect that the method provides a good solution. However, such anxiety is partially true, it is not perfectly ensured that the algorithm always gives the proper solution, due to the randomness.

The important point is that it is basically happy to choose the locally shorter path, but at the same time, a small deviation should be allowed. Such a deviation is a crucial clue to break a curse forcing to focus on limited options only. This kind of spirit is often referred to as "diversification and intensification". In simple problems, simple intensification would work well, one example is the greedy algorithm. But if the problem becomes more complex with additional constraints, intensification could be an obstacle to screen the global perspective. In this case, diversification is also required. Small deviation is a key clue for the diversification, and a lot of mathematical optimization algorithms take such deviation to obtain globally better solutions. The ant colony optimization is one of those algorithms. Pheromone updating plays a role of intensification and resetting is regarded as a diversification procedure. Other than ant colony optimization, there are several methods taking the "diversification and intensification", for instance, simulated annealing [17], tabu search [18], and genetic algorithm [19][20], and so on. It is so interesting to observe that there are several bio-inspired "diversification and intensification" algorithms, such as genetic algorithm and ant colony optimization. It would deserve to consider the feature of evolution and Biomimetics from the aspects of "diversification and intensification" and we discuss in the next chapter.

ACO is known to be an algorithm utilizing the stigmergy [21], which is the nature of self-organization of swarm intelligence without need of central controlling. Such a nature appears in equations (1) and (2) referring to only local information nearby the ant. Thanks to this nature, the ACO can be a strong method when the graph may change dynamically. In the case of a central controlling method, large overhead is required to rebuild the network information. On the other hand, ACO is free from such disturbing overhead because ant has only to react to the local environment nearby which is free from the change in far place. Due to this merit, the ant colony approach is often employed in urban transportation systems and network routing [22-25].

6. Discussion

It would be so interesting to consider Biomimetics, R&D, and species evolution from the aspect of "diversification and intensification". Intensification would be regarded as the refinement based on the well-grounded local examination. Usual research and development activities in the industry would be categorized as intensification. Currently, existing bio-species would be an ultimate consequence of the evolution with intensification, because the several functions are especially emphasized to adjust to the specific environment. Living fossils could be typical explicit examples of intensification. These species already reached the optimal style for surviving, and there is no need to deviate from their style. In this viewpoint, since usual Biomimetics are activities to refer to the specific functions, they are surely regarded as activities utilizing the ultimate form of the intensification. However, species evolution has an aspect of diversification also. The mutation is one typical example. The mutation is a source of diversity of bio-species, and this deviation so-called mutation plays a key role for sustain the environment with bio-species. As we can see from the extinction of dinosaurs and sustained bio-species prosperity, such diversity could be a backup to sustain bio-species under the drastic change of environment. Moreover, the human beings and many animals are the consequence of the mutations. So, the diversification plays a key role to lead to a sustainable and better solution. Due to the virtue, the evolution system is referred to in mathematical optimization directly.

We can also see the significance of the diversification in human activities. In past, there was an event trying to exterminate the sparrows because they steal the rice and crops. However, once the number of sparrows became drastically decreased, a lot of noxious insect spoiling crops showed up and human beings started to suffer from starvation. This is a harmful consequence of intensification from the narrow viewpoint. The point of this story would be that it is important to have a breadth of mind for small deviations and defects. Sustainable traditions would have the good sense to keep diversity, as a consequence of it, they would survive as traditions.

Field of vision with diversification would have a key role to shift to better solution and sustainability. Studies of mathematical optimization would give hints for the perspective.

Acknowledgement
The author would like to thank A. Kawashima and H. Murakami for reading the subscript and make the comments and useful discussions.

References

1. M. Dorigo, PhD thesis, Politecnico di Milano, Italy, (1992).
2. M. Drigo, V. Maniezzo, and A. Colorni, *IEEE Trans. Syst. Man Cybern. Part B* **26** (1996) 1.
3. T. Stutzel and H. H. Hoos, *Future. Gener. Comput. Syst.* **16** (2000) 889.
4. L. M. Gambardella and M. Dorigo, *Proceedings of ML-95, Twelfth Intern. Conf. on Machine Learning* (1995) 252.
5. M. Dorigo and T. Stutzle, "*Ant Colony Optimization*" A Bradford Books (2004) p319.
6. C. Blum, *Comput. Oper. Res* **32** (2005) 1565.
7. B. Bullnheimer, R. F. Hartl, and C. Strauss, "A new rank based version of the ant system" *a computational study* (1997).
8. M. Guntsch and M. Middendorf, *In Workshops on Applications of Evolutionary Computation* (2002) 72.
9. V. Maniezzo, *INFORMS J. Comput.* **11** (1999) 358.
10. O. Cordon I.F. de Viana, and F.H. Triguero, *Mathware & soft computing* **9** (2002) 177.
11. M. Guntsch and M. Middendorf, *In Workshops on Applications of Evolutionary Computation* (2002) 72.
12. C. Blum, "*Theoretical and practical aspects of ant colony optimization*" IOS Press, (2004) p282.
13. C. Blum, A. Roli, and M. Dorigo *In Proceedings of MIC* **2** (2001) 399.
14. J. L. Deneubourg, S. Aron, S. Goss, and J. M. Pasteels, *J. Insect Behav.* **3** (1990) 159.
15. The instance is available at http://elib.zib.de/pub/mp-testdata/tsp/tsplib/tsp/eil51.tsp.
16. TSPLIB, available from http://comopt.ifi.uni-heidelberg.de/software/TSPLIB95/.
17. S. Kirkpatrick, C. D. Gelatt Jr and M. P. Vecchi, *Science* **220** (1983) 671.
18. F. Glover, *Comput. Oper. Res,* **13** (1986) 533.
19. J. H. Holland, "*Adaptation in Natural and Artificial Systems*" A Bradford Books, (1976) p232.
20. D. E. Goldberg, "Genetic algorithms in search, optimization, and machine learning" Addison-Wesley, (1989) p432.
21. M. Dorigo, E. Bonabeau, and G. Theraulaz, *Future Gener. Comput. Syst.* **16** (2000) 851.
22. G. D. Caro and M. Dorigo, *Proceedings of the First International Workshop on Ant Colony Optimization,* (1998).
23. G. D. Caro and M. Dorigo, *Proceedings of the Thirty-First Hawaii International Conference on System Science* **7** (1998) 74.
24. K. M. Sim and W. H. Sun, *IEEE Trans. Syst. Man Cybern. Part A* **33** (2003) 56.
25. G. D. Caro, F. Ducatelle and L. M. Gambardella *Euro. Trans. Telecomms.* **16** (2005) 443.

Journal of Photopolymer Science and Technology
Volume 34, Number 4 (2021) 363−367 ©2021SPST

Effect on Suppression of Biofilm Growth using Microstructures Inspired by Living Organism

Mariko Miyazaki[1*] and Akihiro Miyauchi[2]

[1] Research and Development Group, Hitachi, Ltd.,
7-1-1 Omika-cho, Hitachi, Ibaraki 319-1292, Japan
[2] Institute of Biomaterials and Bioengineering, Tokyo Medical and Dental University,
2-3-10 Kanda-Surugadai, Chiyodaku, Tokyo 101-0062, Japan
**mariko.miyazaki.jm@hitachi.com*

A technique for antibacterial functions is always required in such as medical treatment or food manufacturing. Sharkskin, wings of cicadas and dragonflies have antibacterial functions on their surfaces. It is attractive for human technologies to mimic their microstructural surfaces. In this study, we cultured biofilms on micro-pillar surfaces which was inspired by living organism, and evaluated the antibacterial effect. Growth of biofilms depended on the pitch and diameter of pillar arrays. Formations of the biofilm were suppressed when the pitch and diameter of the pillars were comparable to the size of the bacteria. This suppression seems to be caused by the instability of bacteria sticking on the pillar-array scaffold.
Keywords: Biomimetic riblets, Sharkskin, 3D digitizing, Antibacterial effect, Biofilm, Fluid control

1. Introduction

There has been remarkable progress in biomimetics, the emulation of nature's time-tested patterns, functions, and strategies for the purpose of discovering sustainable solutions to practical problems in recent years [1]. For example, the adhesive function of geckos' feet has been studied [2]. Geckos are known to crawl up walls, hang from ceilings, and firmly grasp slippery glass-like surfaces using their adsorptive toes. The flagella on the soles of geckos' feet are dense, and the feet adhere by van der Waals forces working between the flagella and the surface. In addition, an excellent water-repellent surface was developed that was inspired by the fine, rough surface texture of lotus leaves [3].

With respect to antibacterial effects, two surface structures of living matter are known as having antibacterial functions.

One is the nano-structural pillar surface on the wings of cicadas and dragonflies [4–6]. Ivanova et al. found that the surfaces of both black silicon and wings of *Diplacodes bipunctata* have a strong antibacterial effect that were confirmed by Gram-negative *(Pseudomonas aeruginosa*) and Gram-positive (*Staphylococcus aureus, Bacillus subtilis*) bacteria [4]. Both surfaces have a hierarchical surface-structure through the formation of clusters of adjacent nano-protrusions. These nanostructures are significantly smaller than the size of bacteria, and reported that antibacterial effect is caused by physical breaking of the cell membranes of the bacteria.

Another is the denticles of shark skin. Sharkskin is covered with numerous small tooth-like elements termed "dermal denticles" ("denticles" hereafter) [7, 8]. The microstructure of denticles (i.e., the minute projections) are reported in view of controlling a turbulence flow and reducing drag experimentally and computationally [9–24]. We reported that there is a special flow, vertical flow near the denticles, and this flow beark the bacteria film and suppress the growth of biofilm [25, 26]. Also an antibacterial plate (Sharklet™) made of silicone elastomer has been known to provide an antibacterial effect in various pathogenic microorganisms (*Staphylococcus aureus, methicillin-resistant Staphylococcus aureus, Pseudomonas aeruginosa, Escherichia coli,* and *vancomycin-resistant enterococci*) [27, 28].

Received March 24, 2021
Accepted April 19, 2021

Considering the feature size of functional surfaces of living matters, the micron-scale such as the flagella of geckos' feet or denticles of shark skin is cell-size because these structures are generated by cell. On the other side, the surface structures of lotus leave or wings of cicadas and dragonflies are sub-micron scale and formed by self-organization of proteins or organics.

We focused self-organized structures, namely concave-convex surface, in this research, and analyze the antibacterial effect using artificially designed pillar arrays as a self-organized surface.

2. Experiment

2.1. Fabrication of pillar arrays

Pillar arrays for a bacterial culture were prepared using nanoimprinting [32]. Figure 1 shows the fabrication process of nanoimprint. A mold has fine hole patterns on its surface. The mold is pressed to a resin film at the temperature around a glass-transition of resin film. Then the mold is de-molded from the film, and the designed pillar array were formed on the film surface.

Figure 2 shows a schematic diagram of a mold on which the micro-patterned hole structures were fabricated. A conventional optical lithography and silicon etching were used to fabricate the mold. Figure 2 (a) shows a perspective view of the mold. The mold size is 28 × 28 × 2 mm, and half of the area was the fabrication area. Figure 2 (b) shows a top view of the mold. 1 μm-diameter holes (about the same size as bacteria) and 5 μm-depth were fabricated. The mold was divided into eight regions of 4 mm × 4 mm, and each differed in the pitch (a distance between the centers of the nearest holes). The pitch size were 1.5, 1.6, 1.7, 1.8, 1.9, 2.0, 2.2, and 2.4 μm. Using this mold, pillar arrays on resin films were obtained by nanoimprint.

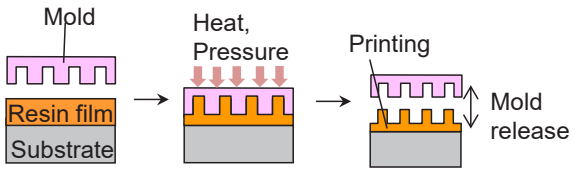

Fig. 1. Method for fabricating resin sheet by nanoimprinting.

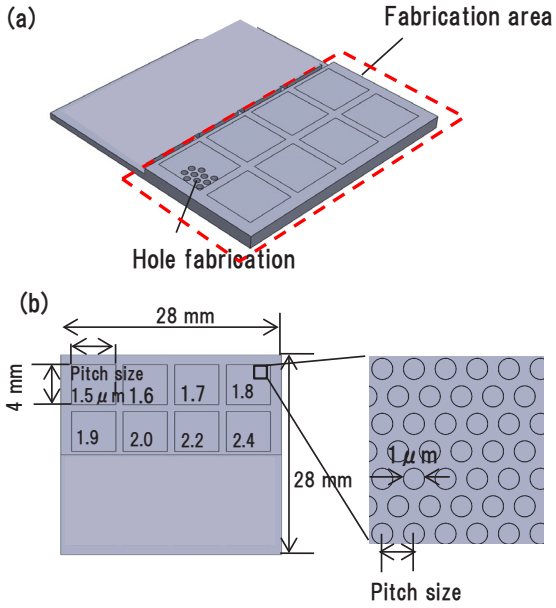

Fig. 2. Schematic diagram of mold for pillar arrays. (a) Perspective view. (b) Top views.

2.2. Method of bacterial culture

A culture device was designed for the pillar arrays. Figure 3 shows a CAD image and appearance of the designed culture device. A resin container which fix the pillar-array chips was placed in a glass petri dish with an outer diameter of 90 mm and a height of 45 mm. The container has four places to fix the pillar-array chip. There was a glass-lid.

The bacterial culture conditions are shown in Table 1. *Staphylococcus aureus subsp. aureus* NBRC 15035 was used as test bacteria. *Staphylococcus aureus* is spherical and has a diameter of about 0.9 μm. The test bacteria was cultured in a trypticase soy (SCD) broth medium, and the number of cultured test bacteria was 10^7–10^8/mL The medium was exchanged once a day. The temperature of an incubator was kept at 37 ℃, and the cultured bacteria solution was obtained on the fifth day of the culture.

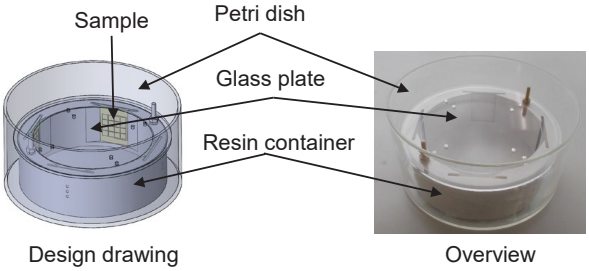

Fig. 3. CAD image and appearance of the culture device.

2.3. Quantification method of bacteria coverage

A degree of biofilm-growth was evaluated by an optical image. After 5-day culture, the pillar array chips were removed from the culture device, and then Gram stain were treated [33]. The chips were immersed in crystal violet solutions for one minute and then rinsed with purified water.

The color-images of dyed chips were taken by an optical microscope. The degree of color indicates a thickness of biofilm, namely the image appears darker as the biofilm becomes thicker. The coverage ratio of biofilm was calculated from a binary-processed image of the chip. Each pixel of the taken image was binarized to white (not existing bacteria) and black (existing bacteria), and the covering ratio was obtained using the equation as follow.

$$\text{covering ratio of bacteria} = \frac{\text{Area of black area}}{\text{Total area of image}} \times 100\ (\%) \quad (1)$$

Table 1. Bacterial culture conditions

Bacteria type	*Staphylococcus aureus subsp. aureus* NBRC 15035
Preparation of bacteria solution	The bacteria are cultured in SCD broth medium at 37 ℃ for 24 hours, and then suspended in SCD broth medium to prepare test bacteria in which the number of bacteria is 10^7 to 10^8 /mL.
Sterilization process	Sterilize test samples culturing equipment under high pressure steam sterilization (121 ℃, 15 minutes)
Biofilm formation	Prepared bacteria solution (300 − 350 mL) was added to the culture device. The solution was stirred for 1 minute using a magnetic stirrer. The cultured device with pillar arrays were rinsed by a purified water three times, then add fresh SOD broth medium (300 − 350 mL) and cultured at 37 ℃. This process repeated once a day.

3. Result and discussion

Figure 4 (a) and (b) shows the SEM image after *Staphylococcus aureus* culture, and the pitch is 1.5 μm and 2.2 μm, respectively. Few bacteria (*Staphylococcus aureus*) were detected in 1.5 μm pitch size. However, there were many bacteria in the gaps of the pillar structures observed like white round shapes in case of 2.2 μm pitch array. Same distributions of bacteria were observed in the case of 2.0 μm pitch array. When the pitch size was large than 2.0 μm, bacteria seems to exist between the pillars and form a biofilm easily.

Figure 5 shows the optical microscopic images (200x) of pillar arrays after 5-day bacterial culture and staining with crystal violet. The pillar structures cannot be observed in this low magnitude, and an average situation can be evaluated in wide area. The optical image becomes darker as increase of pitch size, namely the thickness of biofilm becomes thicker as increase of pitch size of pillar array. Figure 6 shows the relationship between the pitch size and the brightness of each array. The vertical axis is normalized by the value at the pitch size of 1.5 μm. The brightness is maximum when the pitch is lower than 1.7 μm. However, the brightness decreases when the pitch becomes less than 1.9 μm. This shows the growth situation of biofilm depends on the pitch of pillar array, and there is a critical pitch size around 1.7 – 1.9μm. We add the comment that when observe the edge of pillar array region, plenty of stained areas were observed outer the pillar array region, namely a plenty of biofilm was grown on the flat area.

Next, we examined to calculate the coverage ratio of biofilm using equation (1). Figure 7 shows the relationship between the pitch size and the coverage ratio. The coverage ratio on the vertical axis was normalized by the value at the pitch size of 1.5 μm. This graph also shows that there is the critical pillar pitch around 1.7 – 1.9 μm.

As mentioned above, there is the critical pillar pitch around 1.7 – 1.9 μm for growth of *Staphylococcus aureus*. Here considering the size of *Staphylococcus aureus*, namely around 0.9 μm, the suppression model of growth is shown in figure 8. In general, biofilms are grown step by step. First a pioneer bacteria stick on a carbonated substrate, and then a next bacteria stick onto the first pioneer bacteria. Therefore, the important process of biofilm is the first coverage of pioneer bacteria onto the substrate. In our experiment, the first sticking of bacteria is restricted in case of a narrow spacing of pillar. Therefore, the continuous sticking of bacteria

is restricted and a conventional growth process of biofilm seems to be inhibited.

4. Conclusion

Surface structures in micron-scale in nature is formed by self-organization phenomena. The artificially designed micron-structures were designed and pillar array chips were fabricated by nanoimprint. *Staphylococcus aureus* was cultured using the original culture device. The growth of *Staphylococcus aureus* was restricted when the pillar pitch is less than 1.7 – 1.9 μm, and the biofilm did not grow in these narrow pitch array chips. The restriction of inserting *Staphylococcus aureus* to base area of substrate seem to cause the inhabitation of biofilm growth process.

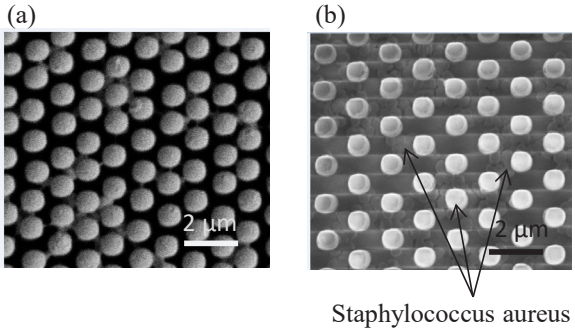

Fig. 4. SEM images of pillar arrays after 5-day bacterial culture. Pitch size is (a) 2.2 μm, (b) 1.5 μm.

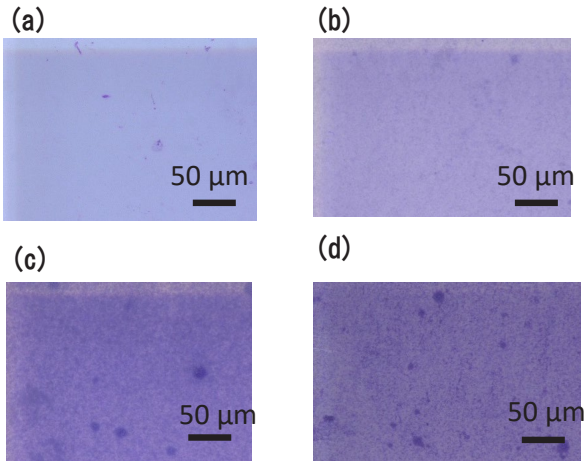

Fig. 5. Microscope images of pillar arrays after 5-day bacterial culture (200x). The chips were stained by crystal violet. The pitch is (a) 1.5 μm, (b) 1.7 μm, (c) 1.8 μm, (d) 2.2 μm.

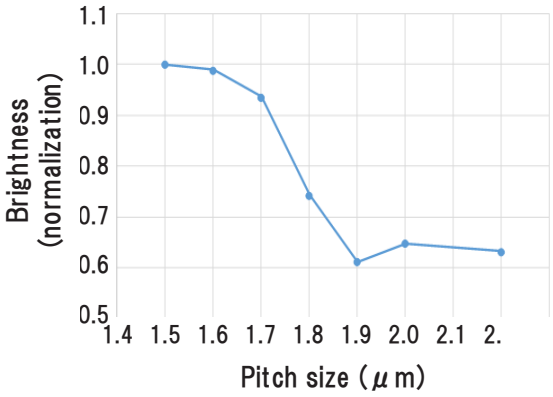

Fig.6. Relationship between pitch size and brightness of optical microscope images of cultured chips.

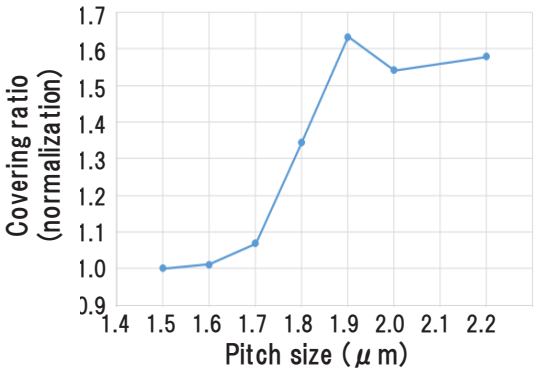

Fig.7. Caluclated coverage ratio of biofilm on cultured chips.

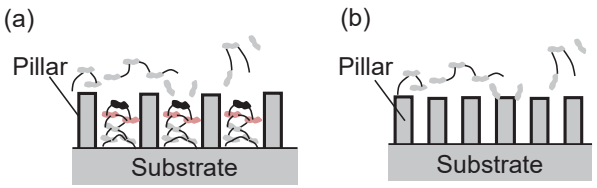

Fig.8. Model of biofilm growth. (a) In case of the pitch size is enough for inserting the bacteria, the bacteria stick onto the base substrate, then biofilm grows step by step by continuous sticking of bacteria. (b) In case of pitch size is narrower than the size of bacteria, the first bacteria is hard to stick onto the pillar-tops and hard to form the biofilm.

4. Conclusion

In this study, we focused on the antibacterial effect of surfaces inspired by living organism and evaluated the effect of suppressing biofilm growth on the scaffold with fabricated microstructural designs. Micro-patterned pillar structures were fabricated on a resin sheet by nanoimprint, on which Staphylococcus aureus was cultured for five days. The amount of attached bacteria was evaluated by calculating the brightness of the optical microscopic

images of cultured samples stained with crystal violet. The micro-patterned pillar structures suppress the biofilm growth and decrease the bacteria covering when the pitch size of the pillars and the size of the bacteria are comparable. The antibacterial mechanism was proposed in which the concavo-convex structure of the surface makes unstable for bacteria sticking and the formation of the biofilm was suppressed when the pitch size of the pillars and the size of the bacteria were comparable.

References

1. H. Liu, T. Nakata, G. Li, and D. Kolomenskiy, *Acta Mechanica Sinica*, **33** (2017) 663.
2. K. Autumn, A. L. Yiching, S. T. Hsieh, W. Zesch, W. P. Chan, and T. W. Kenny, *Nature*, **405** (2000) 681.
3. E. P. Chan, C. Greiner, E. Arzt, and A. J. Crosby, *MRS Bulletin*, **32** (2007) 496.
4. E. Ivanova, J. Hasen, H. Webb, G. Gervinskas, S. Juodkazis, V. Truong, A. Wu, R. Lamb, V. Baulin, G. Watson, J. Watson, D. Mainwaring, and R. Crawford, *Nature Communications*, **4** (2013) 2838.
5. J. Hasen, H. Webb, V. Truong, S. Pogodin, V. Baulin, G. Watson, J. Watson, R. Crawford, and E. Ivanova, *Appl. Microbiol. Biotechnol*., **97** (2013) 9257.
6. K. Nakade, T. Sagawa, H. Kojima, T. Shimizu, and T. Ito, *Material Today*: *Proceedings* **7** (2019) 497.
7. L. Wen, J. C. Weaver, and G. V. Lauder, *J. Exp. Biol*., **217** (2014) 1656.
8. N. E. Kemp, "*Integumentary System and Teeth in Sharks, Skates, and Rays: The Biology of Elasmobranch Fishes*" (ed. W. C. Hamlet), Johns Hopkins University Press, 43 (1999).
9. W. Meyer and U. Seegers, *J. Fish Biol.*, **80** (2012) 1940.
10. J. I. Castro, The Sharks of North America, Oxford University Press, (2011).
11. W. E. Reif and A. Dinkelacker, *Neues Jahrb. Geol. Palaontol. Abh.*, **164** (1982) 184.
12. W. E. Reif, Squamation and Ecology of Sharks , Frankfurt am Main: Senckenbergische Naturforschende Gesellschaft, (1985).
13. D. W. Bechert, M. Bruse, W. Hage, van der Hoeven J, and G. Hoppe, *J. Fluid Mech.*, **338** (1997) 59.
14. D. W. Bechert, M. Bruse, and W. Hage, *Exp. Fluids*, **28** (2000) 403.
15. A.W. Lang, P. Motta, R. Hueter, and M. Habegger, *J. Mar. Technol. Soc.*, **45** (2011) 208.
16. M. J. Walsh, *AIAA J.*, **72** (1980) 168.
17. M. J. Walsh, *AIAA J.*, **21** (1983) 485.
18. P. Vukoslavcevic, J. M. Wallace, and J. I. Balint, *AIAA J.*, **30** (1992) 1119.
19. H. Choi, P. Moin, and J. Kim J, *J. Fluid Mech.*, **255** (1993) 503.
20. S. R. Park, *AIAA J*., **32** (1994) 31.
21. S. J. Lee and S. H. Lee, *Exp. Fluids*, **30** (2001) 153.
22. B. Dean and B. Bhushan, *Phil. Trans. R. Soc.*, **A368** (2010) 4775.
23. C. C. Buttner and U. Shulz, *Smart Matter. Struct.*, **20** (2011) 094016.
24. Y. Luo, Y. Liu, D. Zhang, and EYK NG, *J. Mech. Med. Biol.*, **14** (2014) 1450029.
25. M. Miyazaki, Y. Hirai, H. Moriya, M. Shimomura, A. Miyauchi, and H. Liu, *J. Bionic Engineering*, **15** (2018) 999.
26. M. Miyazaki and A. Miyauchi, *J. Photopolymer Science and Technology*, **32** (2019) 295.
27. K. K. Chung, J. F. Schumacher, E. M. Sampson, R. A. Burne, P. J. Antonelli, and A. B. Brennan, *Biointerphases*, **2** (2007) 89.
28. S. T. Reddy, K. K. Chung, C. J. McDaniel, R. O. Darouiche, J. Landman, and A. B. Brennan, *J. Endourol*., **25** (2011) 1547.
29. D. C. Mayette, *WaterReview*, Water Quality Research Council, Lisle Il (1992) 1.
30. S. B. Borenstein, "*Microbiologically Influenced Corrosion Handbook*", Industrial Press Inc., New York (1994).
31. A. Coghlan, *New Scientist*, **15** (1996) 32.
32. A. Miyauchi, "*Nanoimprinting and its applications*", Jenny Stanford Publishing (2019).
33. M. J. Wilhelm, J. B. Sheffield, M. S. Gh., Y. Wu, C. Spahr, G. Gonella, B. Xu, and H. L. Dai, *ACS Chemical Biology*, **10** (2015) 1711.

Journal of Photopolymer Science and Technology
Volume 34, Number 4 (2021) 369−373 ©2021SPST

Direct Observation of Gastropod's Locomotion for Soft Robot Application

Kazuki Maeda[1] and Fujio Tsumori[2*]

[1] Department of Mechanical Engineering, Kyushu University,
744 Motooka, Nishi-ku, Fukuoka 819-0395, Japan
[2] Department of Aeronautics and Astronautics, Kyushu University,
744 Motooka, Nishi-ku, Fukuoka 819-0395, Japan
**tsumori@aero.kyushu-u.ac.jp*

In this paper, snail's crawling motion was precisely observed and measured to understand the mechanism of its special locomotion. The locomotion has been focused on not only biological researchers but also engineers. Snails can crawl on rough surfaces with obstacles, and also can climb up even on vertical walls. These features are highly useful for applications in the field of soft robotics. We prepared an experimental setup for direct observation of the locomotion. A snail was put on a soft gel substrate, and the deformation of the substrate was measured by tracking marker particles dispersed under the surface of the substrate. At the same time, deformation of the snail's sole was also obtained by tracing the marker particles which was embedded in the snail as fluorescent tattoo. It is essential to obtain these data at the same time to verify the reported locomotion theory. A similar observation was performed with a soft magnetic crawling robot, and we compared these data, which would be helpful to design bio-mimic soft robots like snails.

Keywords: Gastropod, Crawling motion, Soft robot, Bio-mimic, Bio-inspired

1. Introduction

In this paper, we focused on locomotion behavior of gastropods, especially the locomotion of snails. They can crawl on a flat surface using their body propagating wavy contraction and relax motion of muscle. The motion is versatile and makes it possible to crawl on not only flat surfaces but also rough surfaces with obstacles. As you know, locomotion on vertical walls is also possible for them to climb up. These characteristics are highly useful to apply for the soft-robotics field, which has been a growing field.

In the soft-robotics field, elastic or flexible materials are essential to realize many kinds of soft motions. In our previous works, we employed elastomer dispersed with magnetic particles. We developed energy harvesting systems [1-3], artificial cilia [4-14] and worm-like robots [15, 16] using the magnetic soft material. We evaluated the motion of worm-like crawling robots and found that the interface between the robot and the substrate affected so much for the locomotion ability of the robot [15]. Also, wavy motion should be optimized, so that we started to mimic the motion of natural creatures.

Among many kinds of natural creatures, we focused on gastropod, which possesses a soft pedal sole. This pedal is a curious part which can generate wavy motion for locomotion. The crawling mechanism of gastropods has been discussed in some decades [17-19], however more observation has been still needed for further understanding of the locomotion. There are various motions found in natural, and some of them are different each other so much [20]. For example, some gastropods move forward with forward movement of muscle wave, but others move forward with "backward" wave. This behavior has been explained theoretically [19].

It is needed to know stress distribution on the substrate where a test creature crawls. We can measure the stress using soft substrate such as gel, which is soft and easy to deform [21]. In order to verify the theory, not only the force from the body

Received April 1, 2021
Accepted April 27, 2021

to the substrate but also motion of the test creature should be taken simultaneously. This is the main objective of this paper.

For this purpose, 2 colors of fluorescent particles were prepared. One was dispersed on the surface of gel substrate and the other was injected into the sole of the test snail as “fluorescent tattoo”. Also 2 kinds of color filters were prepared so that we could obtain both the deformation of the surface of the substrate and the motion of the bottom surface of the body at the same time. The detailed explanation will be shown in the experimental section.

2. Materials and Methods

Red and blue colored fluorescent particles were prepared for markers. The red particles were dispersed onto the bottom of a plastic case, and uncured silicone gel (Sylgard 527) was poured in it. After curing at 80 ºC for 7.2 ks, the cured silicone gel was put out which has the red markers on the surface. The test creatures were snails (*Euhadra herklotsi*) which were collected for this experiment on Ito campus of Kyushu University. We put blue fluorescent particles into the sole of a snail by a bundle of needles. For easy operation, the snail was anesthetized by dipping diluted mouth wash (Listerine, Johnson & Johnson). This is a popular method to make biological specimens of gastropods. The tattooed particles remained in their body at least for some months. Also, we checked the operation had not harmed their locomotion ability. Figure 1 shows a snail with fluorescent particles inside. The embedded blue particles fluoresced under black light and were clearly observed.

2.1. Experimental setup for snail

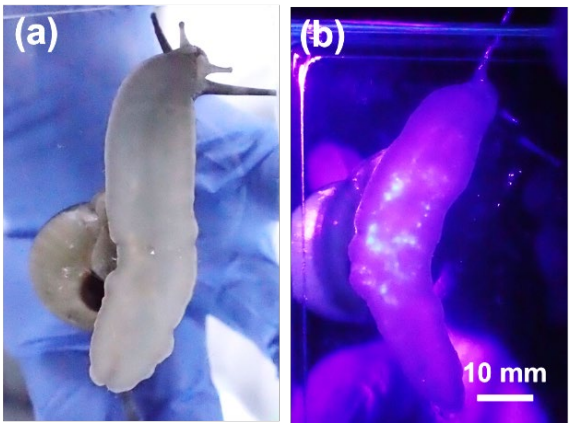

Fig. 1. Snail with blue fluorescent particles inside. Photos under visible light (left), and under black light (right).

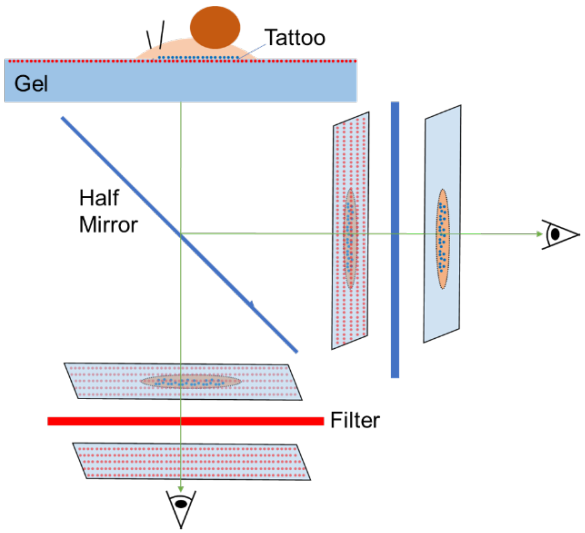

Fig. 2. Schematic illustration of experimental setup. The red particles on the gel surface and the blue particles in a snail are separately observed through filters.

The experimental setup is shown in Fig. 2. The snail was put on a silicone gel substrate, and the crawling snail was observed from the bottom side. The image was split by a half-mirror, and each split image was filtered to show only one of the blue or red image, which corresponded to the motion of snail or the deformation of the gel substrate, respectively.

2.2. Experimental setup for soft robot

We also tried to actuate a crawler-robot which was made of silicone rubber and rubber magnetic parts, which was the same sample as reported work [15], instead of a live snail in a similar setup. The setup is schematically shown in Fig. 3. In this case,

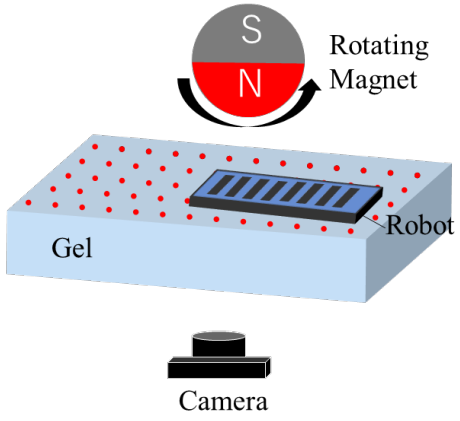

Fig. 3. Experimental setup for a crawler-type magnetic soft robot. The robot was actuated as wavy motion by rotating magnet.

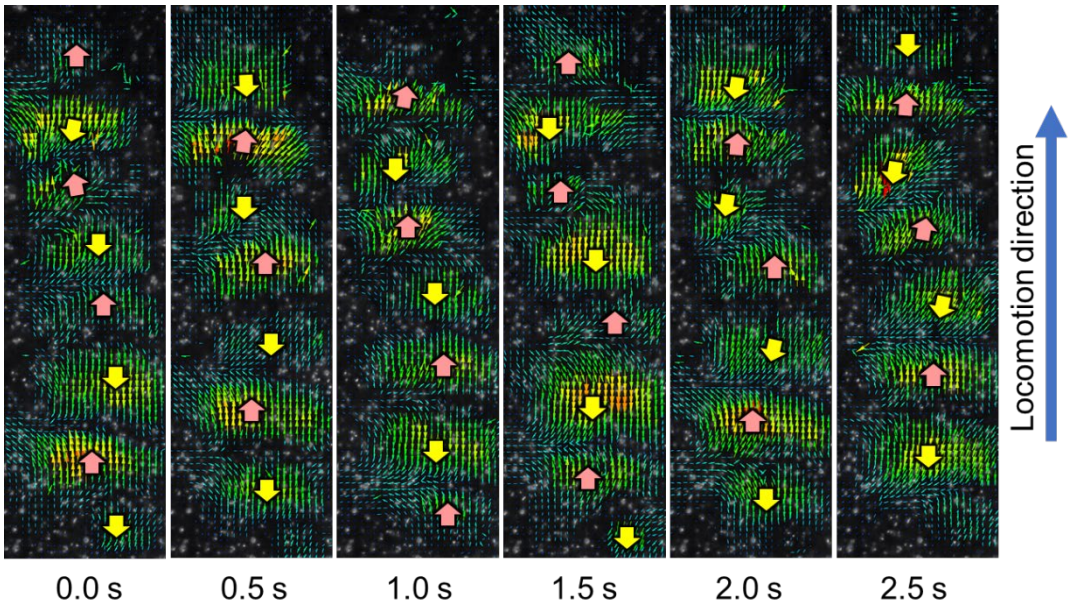

Fig. 4. Velocity map of the gel substrate just under a crawling snail. The map was obtained by PIV. Pink and yellow arrows show upward and downward moving directions, respectively. The arrow patterns shifted upward as the snail crawled upward.

the motion of the robot could be easily observed without fluorescent particles.

3. Results and discussion

3.1. Locomotion of snail

Figure 4 shows velocity map of the gel substrate in every 0.5 s. The snail was crawling from down to up direction. To clarify the motion, pink and yellow arrows are added in each image which shows upper and lower movement, respectively. These pink and yellow arrows were arranged periodically several times and the contraction and extraction areas propagated to upward as the snail crawled to upward. We can obtain stress distribution on the surface of the substrate from this result.

Figure 5 shows deformation of the gel substrate as positions of markers. The blue markers on the snail were also plotted. Wavy change of each position was caused by the force excreted by the snail motion. Phase of each position shifted as its position; however more precise data would be needed using computational image analysis. To show the deformation of the snail, two points on the snail body were selected to be traced. The blue markers in the snail were observed as shown in Fig. 1, and the numbers of the markers were not enough to show deformation in a large area of the snail sole. This is an issue that we should improve the skill of our tattoo operation. Anyway, the 2 blue markers proceeded in y-direction with changing the distance between the markers. This periodic change in the body deformation should be compared with the

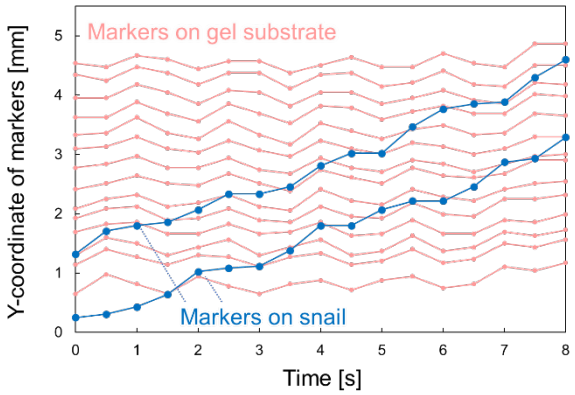

Fig. 5. Markers positions on the gel substrate (red) and on the snail (blue).

stress distribution on the substrate which would express the effect of friction between the body and the substrate. It is the key point of the snail locomotion theory [19] so that more precise and higher resolution of data should be taken.

3.2. Locomotion of soft robot

The similar observation and measurement method could be used also for a robot. Authors already developed soft robots which have been actuated like snails or slugs by an applied magnetic field [15]. In this report, we tried to actuate a crawler on some kinds of substrate, such as glass and paper. The surface state affected so much to crawling behavior of the robots that we should consider the surface effect such as friction.

Figures 6 and 7 show results of the experiments

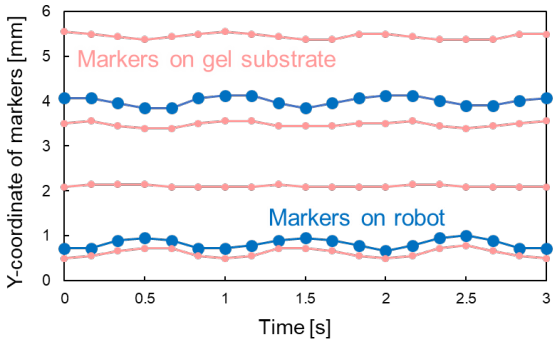

Fig. 6. Markers positions on the gel substrate (red) and on the soft robot (blue). The robot was sticking to the substrate so that it could not proceed, and the substrate deformed similarly.

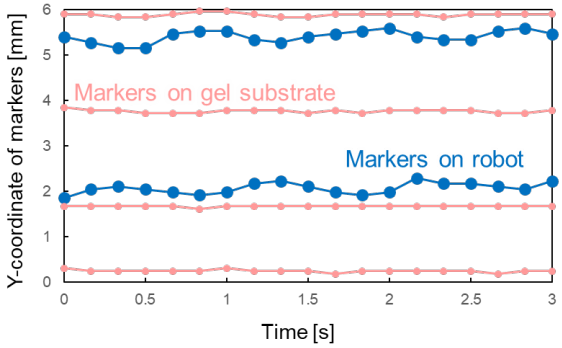

Fig. 7. Markers positions on the gel substrate (red) and on the snail (blue) with oil. The robot slipped on the substrate so there was no deformation in the gel substrate.

of soft robot locomotion. The red lines and the blue lines correspond the motion of the markers on the substrate and the robot, respectively. The robot was just put on the substrate in the former case, and silicone oil was applied on the substrate before putting the robot in the latter case. The robot generated wavy motion that resulted periodic change of the distance between the 2 blue markers; however, the robot did not proceed at all for the both cases. The robot was sticking to the substrate without oil so that the substrate deformed in the same way as the robot. On the other hand, the substrate became so slippery with oil that only the robot deformed in the latter case.

The motions of a live snail and our soft robot look similar; they generated wavy motion from its tail to head. However, the robot could not crawl at all on a gel substrate. We should think 2 possibility, one is the difference of the motion, and the other is the effect of mucus, which is like a highly viscous liquid. Some papers reported non-linear effect of this mucus is the key of the snails' locomotion.

We will check these possibilities as our next work using the presented system. There is an idea to realize various motion in the soft robot. We are now developing 3D printing systems for the magnetic soft materials [22-25]. Of course, we can change oil to many kinds of viscous liquid to change the interfacial state. Also, micro patterning is another way to change the friction effect. Nano-imprinting processes [26, 27] would be a powerful tool for the purpose.

4. Conclusion

We developed a system for observation and measurement of the gastropod locomotion. Using a gel substrate dispersed with fluorescent particles. One of the most important characteristics of this system is simultaneous measurement of gel deformation and test creature's motion. The system is also available to apply for soft robots.

We showed examples using a live snail and a soft robot which was actuated by an applied magnetic field. We will consider the differences between live creatures and robots, such as the mimic of the essence of their movements, frictional phenomena at the interface, and the effects of viscous materials between the body and the ground.

References

1. F. Tsumori, S. Echikawa, Y. Hirabayashi, T. Nakatsuji, T. Osada, and H. Miura, *J. Jpn. Soc. Powder Powder Met.*, 61-4 (2014) 193.
2. H. Shinoda and F. Tsumori, *Jpn. J. Appl. Phys.*, **57**-6 (2018) 06HJ05.
3. D. Maede, F. Tsumori, T. Osada, and K. Kudo, *IEEJ Trans. Sensors Micromachines*, 138-2 (2018) 48.
4. F. Tsumori, N. Miyano, and H. Kotera, *J. Jpn. Soc. Powder Powder Met.*, 56-3 (2009) 133.
5. F. Tsumori, N. Miyano, and H. Kotera, *J. Jpn. Soc. Powder Powder Met.*, 56-3 (2009) 127.
6. F. Tsumori and J. Brunne, *Proc. IEEE MEMS*, (2011) 1245.
7. K. Hatama, F. Tsumori, Y. Xu, H. Kang, T. Osada, and H. Miura, *Jpn. J. Appl. Phys.*, **51**(2012) 06FL14.
8. F. Tsumori, K. Hatama, H. Kang, T. Osada, and H. Miura, *Proc. IEEE-NEMS*, (2013) 845.
9. F. Tsumori, A. Saijou, T. Osada, and H. Miura, *Jpn. J. Appl. Phys.*, **54** (2015), 06FP12.
10. F. Tsumori, R. Marume, A. Saijou, K. Kudo, T. Osada, and H. Miura, *Jpn. J. Appl. Phys.*, **55** (2016), 06GP19.
11. R. Marume, F. Tsumori, K. Kudo, T. Osada, and K. Shinagawa, *Jpn. J. Appl. Phys*, **56** (2017) 06GN15.
12. H. Shinoda, S. Azukizawa, and F. Tsumori, *Proc.*

Micro TAS, (2018) 679.
13. H. Shinoda and F. Tsumori, *Proc. IEEE MEMS*, (2020) 497.
14. S. Gaysornkaew and F. Tsumori, *Jpn. J. Appl. Phys.*, **60** (2021), SCCL02.
15. K. Maeda, H. Shinoda, and F. Tsumori, *Jpn. J. Appl. Phys.*, **59** (2020), SIIL04.
16. H. Shinoda, S. Azukizawa, K. Maeda, and F. Tsumori, *J. Electrochem. Soc.*, **166** (2019) B3235.
17. M. Denny, *Science*, **208**-4449 (1980) 1288.
18. M. Denny, *Nature*, **285** (1980) 160.
19. Y. Tanaka, K. Ito, T. Nakagaki, and R. Kobayashi, *J. Roy. Soc. Interface,* **9** (2011) 222.
20. S. L. Miller, *J. Exp. Marine Bio. Eco.*, **14**-2 (1974) 99.
21. R. W. Style, et al., *Soft Matter*, **10** (2014), 4047.
22. S. Azukizawa, H. Shinoda, K. Tokumaru, and F. Tsumori, *J. Photopolym. Sci. Technol.*, **31**-1 (2018) 139.
23. H. Shinoda, S. Azukizawa, K. Maeda, and F. Tsumori, *ECS Trans.*, **88**-1 (2018) 89.
24. F. Tsumori, H. Kawanishi, K. Kudo, T. Osada and H. Miura, *Jpn. J. Appl. Phys.*, 55-6S1 (2016), 06GP18.
25. S. Azukizawa, H. Shinoda, and F. Tsumori, *Proc. IEEE MEMS*, (2019) 248.
26. Y. Xu, F. Tsumori, H.G. Kang, and H. Miura, *Adv. Sci. Lett.*, **12**-1 (2012), 170.
27. T. Miyata, K. Tokumaru, and F. Tsumori, *Jpn. J. Appl. Phys.*, 59 (2020), SIIJ07.

Journal of Photopolymer Science and Technology
Volume 34, Number 4 (2021) 375−379 ©2021SPST

Soft Actuator with DN-gel Dispersed with Magnetic Particles

Shutaro Shigetomi[1] and Fujio Tsumori[2*]

[1] Department of Mechanical Engineering, Kyushu University, 744 Motooka, Nishi-ku, Fukuoka 819-0395, Japan
[2] Department of Aeronautics and Astronautics, Kyushu University, 744 Motooka, Nishi-ku, Fukuoka 819-0395, Japan
**tsumori@aero.kyushu-u.ac.jp*

We used double-network-gel (DN-gel) to develop a new magnetic gel. Agar and Polyacrylamide gels were selected to prepare Agar/PAAm DN-gel. We dispersed magnetic particles in this gel to fabricate a soft actuator or soft robot. Our modified DN-gel, Agar/PAAm, was suitable for this purpose. During the preparation, we employed thermal initiator instead of UV-initiator, which is popular for DN-gel, for crosslinking. The material contains magnetic particles so that it is difficult to use UV-light. The particles prevent from transmit the light. In this process, we employed thermal initiator so that UV-light is unnecessary. We also propose a micro patterning system of magnetic properties using laser scanning. CO_2 laser was employed for local heating, which can make reversible transformation of gel-liquid states. Finally, we demonstrated a simple strip soft actuator using the proposed method with DN-gel.

Keywords: Soft actuator, Double-network gel, Agar, Magnetic particles, Magnetic orientation

1. Introduction

Recently, double-network gels (DN-gel) have been attracting attention as a tough gel material. This gel was developed by Gong et al. and has the characteristics of compression strength of 20 MPa and elongation at break of more than 80 % [1]. Figure 1 shows an example of DN-gel sample we tried. It is found that the gel was extremely tough. In this study, we aim to develop a soft actuator by dispersing magnetic powder particles in this gel material.

The magnetic soft actuators that have been reported so far mainly use silicone rubber as the base material, and magnetic particles are dispersed in it. The authors have been studying magnetic soft actuators using this kind of silicone rubber, focusing on biomimetic structures such as artificial cilia [2-12] and worm-like robots [13, 14]. Silicone rubber material is a viscous liquid material before curing. We can make magnetic rubber by mixing magnetic powder material with it. Also, it is possible to prepare a magnetic rubber material with magnetic anisotropy by curing it while applying a magnetic field. Silicone is easy to handle and is widely used in this field because it can be prepared as magnetic rubber by the method described above.

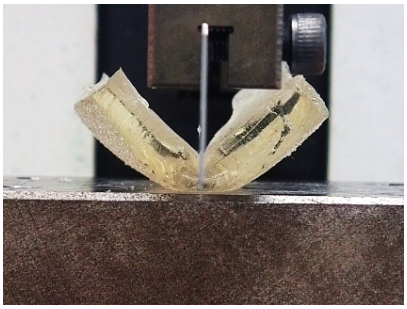

Fig. 1. Photo of DN-gel sample (PAMPS/PAAM gel), which has high resistance from cutting.

On the other hand, in recent years, gel materials have been focused as flexible materials as

Received April 1, 2021
Accepted April 27, 2021

well [15-18]. A gel material is a flexible material that contains a liquid such as water in its polymer network structure. Among them, DN-Gel is a promising material due to its toughness. DN-gel has a structure in which a network of two gel materials overlap at the molecular level. When a large deformation occurs, the first gel network collapses first. On the other hand, the 2nd gel network continues to bridge the 1st gel network, and at that time, the 2nd gel molecular chain slides to relieve the concentration of stress. This is the key mechanism that generates toughness.

The most popular DN-gel material is made of 2 kinds of polymer materials, the 1st gel is poly (2-acrylamido-2-methylpropane-sulfonic acid) gel and poly-acrylamide gel. It is called PAMPS/PAAm gel. This material was developed by Gong et al. In their recipe, UV crosslinking initiator is used and gelation is performed by UV light. The 1st gel material is gelated and then immersed in the 2nd gel monomer solution. After that, the swollen material is irradiated with UV light, and the 2nd gel is gelated to obtain DN-gel.

In this paper, authors propose to use DN-gel as a matrix of a magnetic soft actuator. In order to use DN-gel for this purpose, Gong's PAMPS/PAAm had some problems. Therefore, we chose Agar/PAAm gel system [19], which can be controlled by thermal crosslinking. The reason will be described in the following experimental section.

We also propose a new micro-patterning method of magnetic orientation in this paper. The agar plays an important role for this process, which will be also explained later. This method would be used for a new method for a 4D-printing system of magnetic materials [16-18, 20].

2. Experimental

2.1. DN-gel preparation

We prepared 2 kinds of materials for base gels, agar (Kantenpapa, Ina Food Industry) and acrylamide monomer (AAm). The flow of the preparation of the DN-gel is shown in Fig. 2. At first, 2 mass% of aqueous solution of agar was prepared by heating, and magnetic powder (carbonyl iron OM, BASF) with a mean diameter of 4.3 μm was mixed in it (Fig. 2a). The mixture was put in a plastic case and it was cooled in a refrigerator at 4 ºC for 1.8 ks (0.5 h). Agar gel dispersed with magnetic particles was obtained (Figs. 2b, c). Next, the agar gel was dipped into AAm solution for 10.8 ks (3h). The AAm solution was added 0.03 mol% of methylene-bisacrylamide (MBAA) as crosslinker, 1 mol% of ammonium peroxodisulfate (APS) as thermal initiator, and 0.25 mol% of

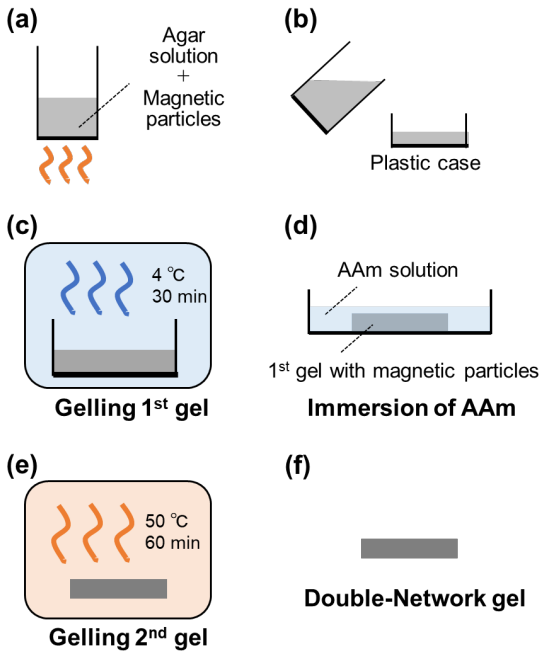

Fig. 2. Flow of Agar/PMMa DN-gel preparation.

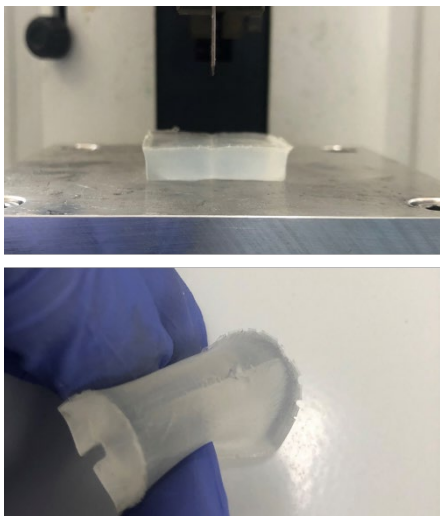

Fig. 3. Prepared Agar/PAAm gel sample; (upper) after knife edge cutting test, and (lower) the bent sample after the test.

tetramethylethylenediamine (TEMED) as hardening accelerator agent (Fig. 2d). The gel sample was heated at 50 ºC for 3.6 ks (1h) to crosslink AAm, and finally Agar/PAAm DN-gel was obtained (Figs. 2e, f). The material contains magnetic particles so that it is difficult to use UV-light. The particles prevent from transmit the light. In this process, we employed thermal initiator so that UV-light is unnecessary.

Figure 3 shows an example of an obtained DN-gel sample. We checked the toughness by a preliminary cutting resistance test. The sample was hard to cut by a knife edge, and hard to fracture even

in a severe bending state after testing.

2.2. Tensile test

Tensile test was performed in accordance with JIS6251K. We used a testing machine (EZ-Test, Shimadzu Cooperation) for the test. We prepared 4 kinds of Agar/PAAm DN-gels which contained 0, 5, 10, and 20 mass% of carbonyl iron powder. Test specimens of the 1st and 2nd gels, which were agar gel and PAAm gels, were also prepared. For all samples, stress-strain relations were obtained. Tensile speed was set at 10 mm/min for each sample.

2.3 Micro-patterning of magnetic orientation

Magnetic particles generate chain-like cluster structures which align to be parallel to an applied magnetic field. We can fix the cluster structures in a gel matrix to set an anisotropic magnetic orientation in the material. We propose a new method to pattern the magnetic orientation in a DN-gel sheet.

Figure 4(a) shows a schematic illustration of this process. A sheet of agar gel, which is just before immersion of AAm, is put under an applied magnetic field. Laser is scanned on the agar sheet to heat and melt the agar sheet. By laser heating, the agar is molten so that the magnetic particles can move freely and generate chain clusters as to align the applied magnetic field. The cluster structures are fixed by re-gelation after cooling in the air. Agar is useful for the present method as this reversible gel-liquid change by temperature. During the laser processing, a thin glass sheet was put on the agar sheet not to dry it. Figure 4(b) shows obtained micro chain clusters. The obtained agar sheet will be processed as shown in Figs. 2(d-f).

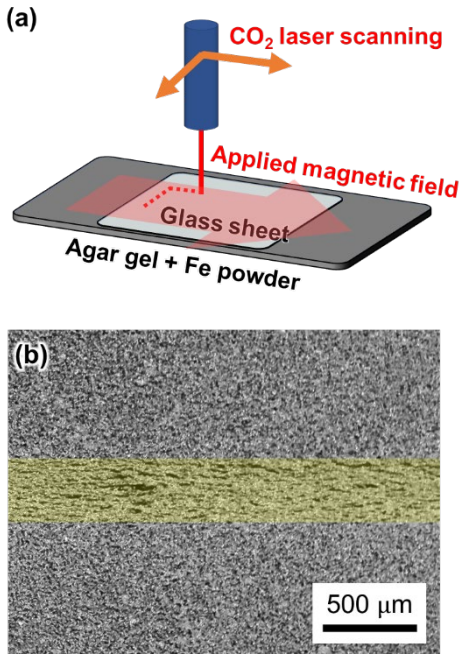

Fig. 4. (a) Schematic illustration of proposed patterning system of magnetic orientation, and (b) Sample photo of chain-like clusters. The highlighted area shows laser-scanned line, where horizontal chain-like clusters of particles were generated.

3. Results and discussion

3.1. Tensile tests

Stress-strain curves are shown in Fig. 5. The elongation of the 1st gel, agar, was much smaller than any other samples. The 2nd gel showed high elongation, while the tensile strength was less than 0.1 MPa. The DN-gel sample based on these 2 gels improved much better in the tensile properties. The elongation was more than 1000 % and the tensile strength was about 0.6 MPa.

As increasing iron powder contents, tensile properties decreased, however the tensile strength of each sample was larger than that of the 1st or 2nd gel. The particles might be origins of fractures in this case. The properties could be improved by surface treatment of powder particles, which would cause high bonding effect between particles surface and gel molecules.

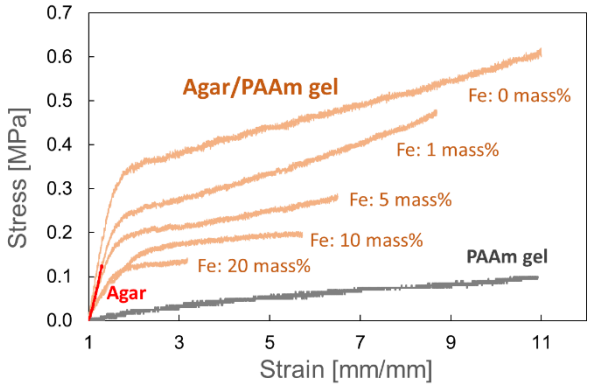

Fig. 5 Stress-strain relationships of DN-gel samples. The 1st and 2nd gels data were also plotted.

3.2. Micro-patterning and actuation

We prepared a sample strip as shown in Fig. 6. We scanned lasers in parallel lines changing the direction of an applied magnetic field. After cutting out, a thinner strip sample was obtained. Figure 7 shows an optical micro photo of the sample at the area as shown in Fig. 6(a). Chain clusters were generated in the scanned area.

The cut sample strip was set under a vertical applied magnetic field of 0.6 T. The deformed sample is shown in Fig. 8. Different rotational

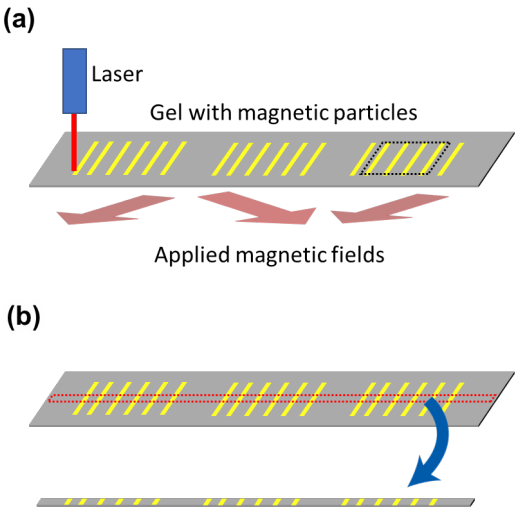

Fig. 6. Schematic of sample preparation; (a) Laser scanning pattern and applied magnetic fields, and (b) dimension of cut sample.

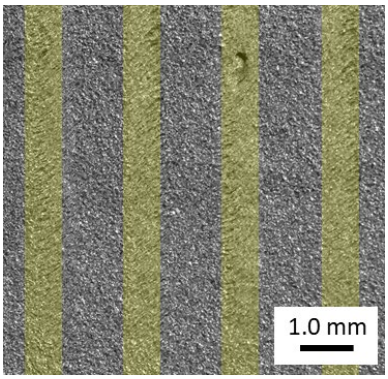

Fig. 7. Optical micro-photo image of laser scanned sample. The observed area is shown in Fig. 6(a) as a square with dashed line.

moments excreted in the 3 areas caused wavy shape change. Patterning of magnetic property was successfully applied by our proposed method.

4. Conclusion

We proposed to use DN-gel for magnetic soft actuators. Agar and PAAM gels were combined as DN-gel material for this purpose. The obtained material showed excellent tensile properties. Micro patterning system using laser scanning was also proposed for further application of 3D or 4D printing. We demonstrated a simple strip sample, which could actuate by an applied magnetic field.

The method would be useful to develop soft robots which is bio-compatible or bio-degradable. Micro- or nano- patterning on this kind of soft material on the surface will be our future work [21, 22], which would improve the locomotion ability of soft robots.

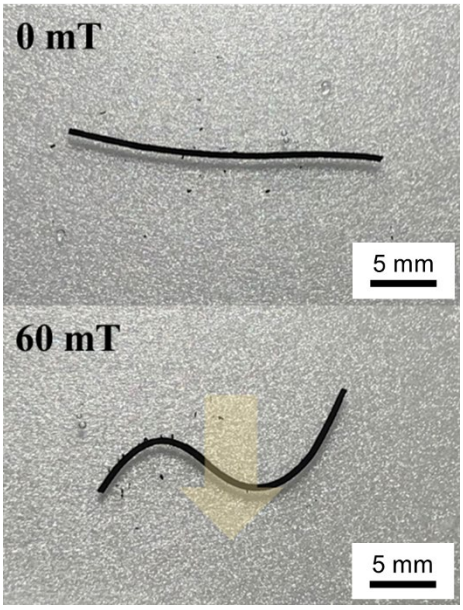

Fig. 8. DN-gel strip sample with patterned magnetic orientation. Wavy deformation was observed under a vertical magnetic field.

References

1. J. P. Gong, Y. Katsuyama, T. Kurokawa, and Y. Osada, *Adv. Mater.*, **15** (2003), 1155.
2. F. Tsumori, N. Miyano, and H. Kotera, *J. Jpn. Soc. Powder Powder Met.*, **56-3** (2009) 133.
3. F. Tsumori, N. Miyano, and H. Kotera, *J. Jpn. Soc. Powder Powder Met.*, **56-3** (2009) 127.
4. F. Tsumori and J. Brunne, *Proc. IEEE MEMS*, (2011) 1245.
5. K. Hatama, F. Tsumori, Y. Xu, H. Kang, T. Osada, and H. Miura, *Jpn. J. Appl. Phys.*, **51** (2012) 06FL14.
6. F. Tsumori, K. Hatama, H. Kang, T. Osada, and Hideshi Miura, *Proc. IEEE-NEMS*, (2013) 845.
7. F. Tsumori, A. Saijou, T. Osada, and H. Miura, *Jpn. J. Appl. Phys.*, **54** (2015), 06FP12.
8. F. Tsumori, R. Marume, A. Saijou, K. Kudo, T. Osada, and H. Miura, *Jpn. J. Appl. Phys.*, **55** (2016), 06GP19.
9. R. Marume, F. Tsumori, K. Kudo, T. Osada, and K. Shinagawa, *Jpn. J. Appl. Phys.*, **56** (2017) 06GN15.
10. H. Shinoda, S. Azukizawa, and F. Tsumori, *Proc. MicroTAS*, (2018) 679.
11. H. Shinoda and F. Tsumori, *Proc. IEEE MEMS*, (2020) 497.
12. S. Gaysornkaew and F. Tsumori, *Jpn. J. Appl. Phys.*, **60** (2021), SCCL02.
13. K. Maeda, H. Shinoda, and F. Tsumori, *Jpn. J. Appl. Phys.*, **59** (2020), SIIL04.
14. H. Shinoda, S. Azukizawa, K. Maeda, and F. Tsumori, *J. Electrochem. Soc.*, **166** (2019)

B3235.
15. S. Shigetomi, H. Takahashi, and F. Tsumori, *Jpn. J. Appl. Phys.*, **33** (2020), 193.
16. S. Azukizawa, H. Shinoda, K. Tokumaru, and F. Tsumori, *J. Photopolymer Sci. Technol.*, **31-1** (2018) 139.
17. H. Shinoda, S. Azukizawa, K. Maeda, and F. Tsumori, *ECS Trans.*, **88-1** (2018) 89.
18. S. Azukizawa, H. Shinoda, and F. Tsumori, *Proc. IEEE MEMS*, (2019) 248.
19. D. Wei, J. Yang, L. Zhu, F. Chen, Z. Tang, G. Qin, and Q. Chen, *Polymer Testing*, **69** (2018) 167.
20. F. Tsumori, H. Kawanishi, K. Kudo, T. Osada, and H. Miura, *Jpn. J. Appl. Phys.*, **55-6S1** (2016), 06GP18.
21. Y. Xu, F. Tsumori, H.G. Kang, and H. Miura, *Adv. Sci. Lett.*, **12-1** (2012), 170.
22. T. Miyata, K. Tokumaru, and F. Tsumori, *Jpn. J. Appl. Phys.*, **59** (2020), SIIJ07.

Journal of Photopolymer Science and Technology
Volume 34, Number 4 (2021) 381−384 ©2021SPST

Glass Microchannel Formation by Mycelium

Daiki Sato[1] and Fujio Tsumori[2*]

[1] Department of Mechanical Engineering, Kyushu University,
744 Motooka, Nishi-ku, Fukuoka 819-0395, Japan
[2] Department of Aeronautics and Astronautics, Kyushu University,
744 Motooka, Nishi-ku, Fukuoka 819-0395, Japan
**tsumori@aero.kyushu-u.ac.jp*

We propose a new method to fabricate complicated 3-dimensional glass microchannels. We employed mycelium for this purpose. Mycelium possesses a complicated, fine and three-dimensional network structure. We cultivated mycelium in silica compounds, and subsequently silica compounds were heated to be sintered. During this heating process, all the mycelium was burned off and remained a fine network channel structure in a transparent glass chip. We also tried to control of the growth of this mycelium. The growth could be changed by growth conditions. In this work, we used cyclic mechanical stimuli for this purpose. We set cyclic tensile strain to the sample under growing mycelium. This cyclic strain caused anisotropic growth of the mycelium in some condition.
Keywords: Microchannel, Glass, Mycelium, Aspergillus oryzae

1. Introduction

In this paper, we employed mycelium to form 3-dimensional microchannel in a glass chip. Microchannels are widely used for lab-on-a-chip including organ-on-a-chip. The popular microchannels are 2-dimensional, and most of them are fabricated by lithography methods [1]. It is more difficult to prepare 3-dimensional channels, some processes have been proposed to fabricate them, such as lamination [2-4], reverse imprinting [5, 6], and the utilization of deformation [7-10] and the 3D printer [11-13]. The blood vessel structure is more complicated than that of microchannels fabricated by these methods.

Authors utilized glass nano powder as a start material of microchannels in this work. We have already developed many kinds of processes to form micropatterned sheets or other micro devices using nano powders [14-25]. Nano powders of ceramics and glasses are popular and already have used in industry fields, so that it is affordable and easy to obtain. We can form nano powder as a powder compact by some ways. Sometimes we compress powder; this is the simplest way to get some form. Also, we can mix powder to polymer binder material. The mixed compound material could show plasticity, and we can form it easier. We have tried nano imprint lithography to fabricate a ceramic or glass sheet with highly fine patterns on it. After forming, powder compacts can be solidified by heating. It is called sintering process.

Fig. 1. Overview of rice-malt, *Aspergillus oryzae*, employed for this work.

Instead of forming by machines, we came up with an idea that live organs such as plant root or mycelium could form the nano powder compound. Plants and fungi grow into soil which consists of inorganic particles. Nano particles could also work as soil. We have tried to grow plant seed on nano particles with aqueous binder. The seed grew into particles, and after then, we heated this “soil” with

Received April 7, 2021
Accepted April 27, 2021

plant to burn off the plant and to sinter the sample. We obtained a ceramic chip with root-shaped microchannels [26]. Silica powder was also used for the same procedure, and a transparent glass chip with microcavity was obtained [27]. In this glass chip, we could fix the structure where plant roots were in symbiosis with arbuscular mycorrhiza.

In this paper, rice-malt, *Aspergillus oryzae*, was employed to form microchannels in glass chips. Figure 1 shows rice-malt we used in this work. Mycelium generated a network structure in the sample, which could be fixed as a cavity in a transparent glass chip after sintering. It is also important to control growth of mycelium. The growth could be changed by growth conditions. We used cyclic mechanical stimuli for this purpose. We set cyclic tensile strain to the sample under growing mycelium.

2. Experimental

2.1. Cultivation and sintering

Aqueous solution of agar and sucrose as cultivation medium. Water was boiled, and 1 mass% agar and 1 mass% sucrose was dissolved. The same mass of silica powder was mixed with the solution to obtain a compound material. We prepared spherical silica powder (SC2500-SQ, Admatechs). The particle size of the prepared silica powder was about 0.5 μm. We dispersed spores into water by dipping edible rice-malt grains. The spores were mixed into the silica compound, and subsequently, mixed sample was poured into a plastic case. After cooling, agar became gelatinous.

The sample was put in an incubator at 35 ºC for 2 days. After growth of mycelium, the sample was taken out from the case and was dried in an oven at 50 ºC for more than 21.6 ks (6 h). Next, the dried sample was sintered at 1400 ºC for 7.2 ks (2 h). The obtained glass samples were observed by an optical microscope.

2.2. Cultivation under cyclic strain.

A flexible container was made using silicone rubber (Ecoflex 00-30, SmoothOn) to be deformed. The container was set to a hand-maid stretching device. The container and the device are shown in Fig. 2. In this experiment, 0.5 mass% agar gel was used as cultivation medium. Sucrose of 1.0 mass% was also added to the gel. Silica powder was not used in this experiment for easy observation.

We prepared 2 kinds of samples following the flows as shown in Fig. 3; one was an agar sample dispersed with spores, and the others was 2 agar sheets which sandwiched spores. Both samples in the silicone container was set in an incubator, and

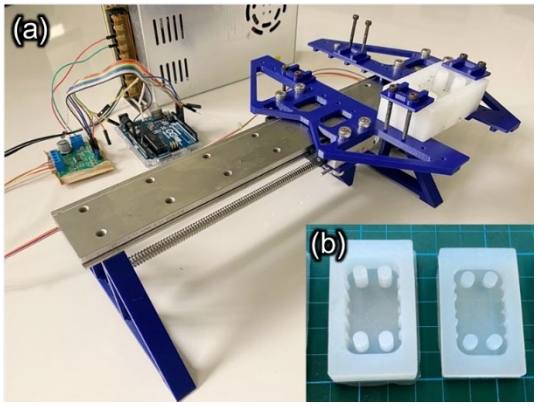

Fig. 2. (a) Stretching device, and (b) silicone containers. The soft containers could be attached to the device so that the linear rale could apply cyclic strain. The cyclic motion was controlled by microcomputer board which is also shown in this figure.

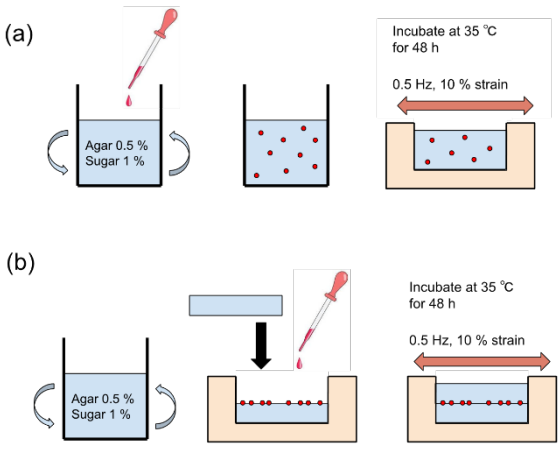

Fig. 3. Two methods for agar sample preparation. (a) Spores were dispersed in medium. (b) Spores were set between 2 gel sheets.

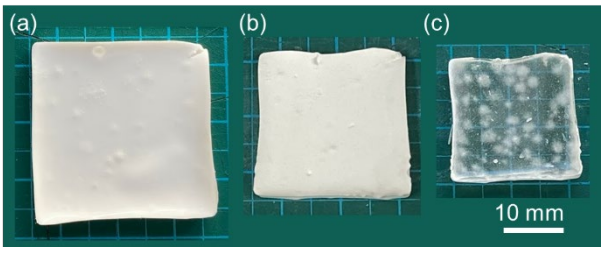

Fig. 4. Sample after cultivation (a), after drying (b), and after sintering (c).

applied cyclic strain of 10 % at 0.5 Hz. Incubation was carried out at 35 ºC for 2 days.

3. Results and discussion

3.1. Sintered glass channel

Figure 4 shows photos of a silica sample with mycelium after cultivation (a), after drying (b), and

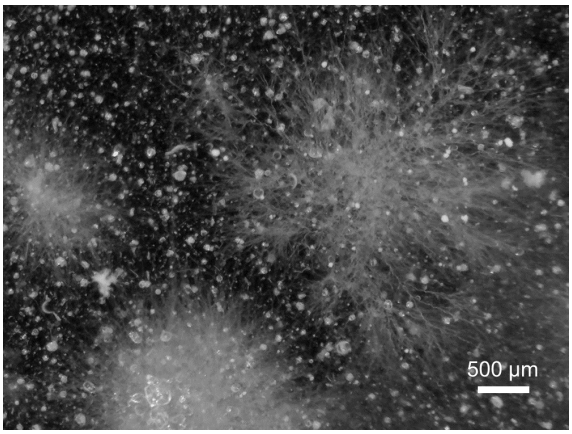

Fig. 5. Optical micro photo of sintered glass chip. Microchannels remained after mycelium networks are observed.

after sintering (c). Shrinking was observed in each step. After cultivation, a sample gel was distorted a little, and more distortion was observed during the drying stage, but there was less distortion during sintering.

The sintered sample looked clear, but unclear spots were observed inside. Spots were observed by an optical microscope. The image is shown in Fig. 5. The spot was an area where a colony of mycelium grew. From the microscopic image, many pores were also observed. We have not made it clear how these pores generated. It might be possible that bubbles which were generated during mixing the high viscous material had remained in the compact. We should improve the process to remove the bubbles.

3.1. Anisotropic growth under cyclic strain

We cultivated mycelium in 2 kinds of setup. The first one was with a medium in which spores were dispersed (Fig. 3a), and the other one was that spores were sandwiched between agar sheets (Fig. 3b). Figure 6 shows the mycelium in the former setup. There were colonies which were similar to the result in the previous section. The growth was isotropic that means the colony grew radially even under unidirectional cyclic strain.

In the latter case, mycelium grew differently between agar sheets. Figure 7 shows colonies after cultivation. The colony which grew in a static state was isotropic, whereas the mycelium was aligned vertical direction, which was the same direction to the cyclic strain.

The strain caused anisotropic growth of mycelium. This is one possible way to control the growth. We will try to cultivate mycelium in a silica compound to fabricate a glass chip with controlled grown channels. This is our future work.

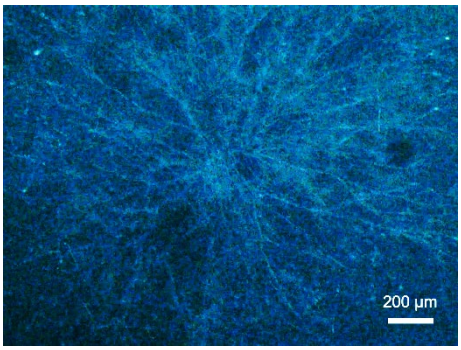

Fig. 6. Colony of mycelium grown in medium dispersed with spores at initial state.

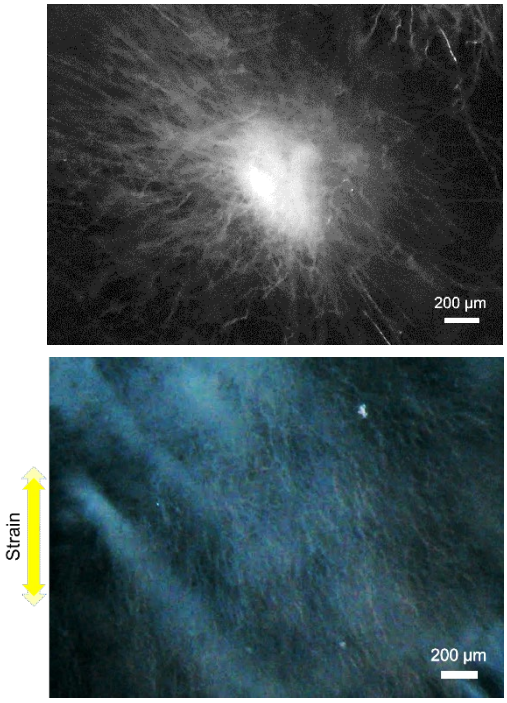

Fig. 7. Colony of mycelia grown between 2 agar sheets in a static state (upper), and under vertical cyclic strain (lower).

4. Conclusion

We propose a method to form microchannels in a glass chip by growth of mycelium. We employed silica nano powder as a starting material and fabricated a glass chip with fine channels. In order to control the growth of the mycelium, we cultivated mycelium under uniaxial cyclic strain state. Anisotropic growth was observed in some condition.

Acknowledgement

This work was partly supported by MEXT KAKENHI Grant Number JP21H00371.

References

1. P. Gravesen, J. Branebjerg, and O. S. Jensen, *J.*

Micromech. Microeng., **3** (1993) 168.
2. J. R. Anderson, D. T. Chiu, R. J. Jackman, O. Chemiavskaya, J. C. McDonald, H. Wu, S. H. Whitesides, and G. M. Whitesides, *Anal. Chem.*, **72** (2000) 3158.
3. D. T. Chiu, N. L. Jeon, S. Huang, R. S. Kane, C. J. Wargo, I. S. Choi, D. E. Ingber, and G. M. Whitesides, *PNAS*, **97** (2000) 2408.
4. B.H. Jo, L.M. Van Lerberghe, K.M. Motsegood, and D.J. Beebe, *J. Microelectromech. Syst.*, **9** (2000) 76.
5. M. Nakajima, T. Yoshikawa, K. Sogo, and Y. Hirai, *Microelectron. Eng.*, **83**, (2006) 876.
6. W. Hu, B. Yang, C. Peng, and S. W. Pang, *J. Vac. Sci. Technol. B*, **24** (2006) 2225.
7. F. Tsumori, S. Hunt, K. Kudo, T. Osada, and H. Miura, *J. Jpn. Soc. Powder Powder Met.*, **63** (2016) 511.
8. F. Tsumori, S. Hunt, T. Osada, and H. Miura, *Jpn. J. Appl. Phys.*, **54**, (2015) 06FM03.
9. K. Tokumaru, S. Hunt, and F. Tsumori, *Proc. MicroTAS*, (2018) 522.
10. H. Wu, T. W. Odom, D. T. Chiu, and G. M. Whitesides, *J. Am. Chem. Soc.* **125** (2003) 554.
11. W. Wu, A. DeConinck, and J. A. Lewis, *Adv. Mater.,* **23** (2011) H177.
12. P. J. Kitson, M. H. Rosnes, V. Sans, V. Dragone, and L. Cronin, *Lab Chip*, **12** (2012) 3267.
13. W. Lee, D. Kwon, W. Choi, G. Y. Jung, A. K. Au, A. Folch, and S. Jeon, *Sci. Rep.,* **5** (2015) 9701 (2015).
14. Y. Xu, F. Tsumori, H.G. Kang, and H. Miura, *J. Jpn. Soc. Powder Powder Metall.,* **58** (2011) 673.
15. Y. Xu, F. Tsumori, T. Toyooka, H. Kotera, and H. Miura, *Jpn. J. Appl. Phys.,* **50** (2011) 06GK11.
16. X. Yang, F. Tsumori, H. G. Kang and M. Hideshi, *Adv. Sci. Lett.,* **12** (2012) 170.
17. Y. Xu, F. Tsumori, S. Hashimoto, M. Takahashi, H. Kang, T. Osada and H. Miura, *Micro Nano Lett.,* **8** (2013) 571.
18. F. Tsumori, Y. Tanaka, X. Yang, T. Osada and H. Miura. *Jpn. J. Appl. Phys.,* **53** (2014) 06JK02.
19. F. Tsumori, K. Tokumaru, K. Kudo, T. Osada, and H. Miura, *J. Jpn. Soc. Powder Powder Metall.,* **63** (2016) 519.
20. K. Tokumaru, F. Tsumori, K. Kudo, T. Osada and K. Shinagawa, *Jpn. J. Appl. Phys.,* **56** (2017) 06GL04.
21. K. Yonekura, K. Tokumaru and F. Tsumori, *Jpn. J. Appl. Phys.,* **57** (2018) 06HG05.
22. K. Tokumaru, K. Yonekura, and F. Tsumori, *J. Photopolym. Sci. Tech.*, **32** (2019) 315.
23. T. Miyata, K. Tokumaru, and F. Tsumori, *Jpn. J. Appl. Phys.*, **59** (2020) sIIJ07.
24. T. Miyata, K. Tokumaru, and F. Tsumori, *J. Photopolymer Sci. Tech.*, **33** (2020) 199.
25. F. Tsumori, Y. Xu, H. Kang, T. Osada and H. Miura, *Proc. 12th Computational Plasticity,* (2013) 1267.
26. S. Nakashima, K. Tokumaru, and F. Tsumori, *Jpn. J. Appl. Phys.*, **57** (2018) 06HJ07.
27. S. Nakashima, K. Tokumaru, and F. Tsumori, *Proc. MicroTAS*, (2018) 535.

Communication

Journal of Photopolymer Science and Technology
Volume 34, Number 4 (2021) 385−392 ©2021SPST

Microstructure Formation on Poly (Methyl Methacrylate) Film Using Atmospheric Pressure Low-Temperature Plasma

Masashi Yamamoto[1*], Youichiro Mori[1], Takuya Kumagai[1], Atsushi Sekiguchi[2,3], Hiroko Minami[3], and Hideo Horibe[4]

[1] National Institute of Technology, Kagawa College, Department of Electrical and Computer Engineering, 335 Chokushi-cho, Takamatsu, Kagawa 761-8058, Japan
[2] Osaka Prefecture University, Department of Physics and Electronics, 1-1 Gakuen-cho, Naka-ku, Sakai, Osaka 599-8531, Japan
[3] Litho Tech Japan Corporation, 2-6-6 Namiki, Kawaguchi, Saitama 332-0034, Japan
[4] Osaka City University, Department of Physics and Electronics, 3-3-138 Sugimoto-cho, Sumiyoshi-ku, Osaka 558-8585, Japan
**m-yamamoto@t.kagawa-nct.ac.jp*

This study targets development of a biomimetic technique for mitigating endoscope surface antifouling. We specifically examined a snail's shuck, which has convexo-concave microstructures, to achieve an antifouling function. Unfortunately, fabricating microstructures on lens surfaces entails large costs because of technical difficulties. As one alternative method, we fabricated microstructures on films with different PMMA concentrations and examined their surface profiles using atmospheric pressure low-temperature plasma. Convex structures on a low (67.4 wt%) PMMA concentration film have a rounded tip at high RF power. When RF power is low, however, structures fabricated on a 67.4 wt% PMMA film surface were more incisive and orderly than those on a 84.4 wt% PMMA film. Microstructures with 200-nm pitch, like a snail's shuck, were fabricated on a 67.4 wt% PMMA film when irradiating plasma at 52 W for 40 s.

Keywords: Biomimetics, Snail's shuck, Super nanohydrophilia, Antifouling function

1. Introduction

For today's medical care, laparoscopic surgery is commonly used to reduce postoperative burdens on patients. During the operation, steam, blood, and body fluids adhere to the endoscope lens surface. Therefore, endoscope must be taken out of the patient's body frequently to wash the lens. Those interruptions not only extend the operation time: they increase burdens on the patient. These shortcomings can be resolved by fabricating microstructures on the lens surface to provide antifouling functionality.

We specifically examined a snail shuck surface to achieve an antifouling function. This surface has convexo-concave microstructures. When the surface is covered with water, a thin water film is formed on the surface. This water film can repel smears and provide superior antifouling functionality. This structure, designated as a super nanohydrophilic structure, has antifouling function for repelling oil-containing proteins. This super nanohydrophilic effect can be achieved by fabricating convexo-concave microstructures at 200 nm pitch, thereby mimicking the snail's shuck, on the lens surface [1]. This technique, called *biomimetics*, artificially mimics widely diverse functions possessed by living organisms in the natural world [2]. For this study, we used biomimetics to develop a surface antifouling function improvement for use with endoscopy.

The base lens material of the endoscopic instrument is glass. Because of the related technical difficulties, fabricating microstructures on its surface is costly. An alternative to methods for direct processing of glass is desired. We suggest a method of fabricating microstructures on the

Received March 31, 2021
Accepted April 28, 2021

polymer surface to coat a glass substrate because the polymer can be processed easily. Polymethylmethacrylate (PMMA) is an appropriate polymer for our suggested method because of its high transparency. We used an atmospheric pressure low-temperature plasma [3, 4] to fabricate microstructures. We irradiated the PMMA surface using plasma and examined the relation between the irradiation time and surface profile. We report results of the present study hereinafter.

2. Experimental

2.1. PMMA film preparation

Spin-coating and baking conditions were adjusted such that the initial PMMA film thickness was 4.00 ± 0.30 μm. Table 1 shows the PMMA film formation conditions. After the PMMA (Sigma-Aldrich Corp., LLC, M_W = 15,000) was dissolved in lactic acid ethyl (Wako first Grade; Fujifilm Wako Pure Chemical Corp.), the solution concentration was 30.0 wt%. The solution was spin-coated onto a glass substrate (1 mm thickness, 76×52 mm^2, S9111; Matsunami Glass Ind., Ltd.,) using a spin-coater (K-359 S-1; Kyowa Riken Co., Ltd.). After pre-baking of the substrate in an oven (CLO-2AH; Koyo Thermo Systems Co., Ltd.), the initial film thickness was measured using a surface profiler (Surfcom 480A; Tokyo Seimitsu Co., Ltd.). The PMMA film concentration was calculated by weighing the substrate before and after baking.

2.2. Plasma treatment

Each sample substrate was irradiated with plasma. Figure 1 portrays a plasma treatment equipment diagram. RF power supply (Pearl Kogyo Co., Ltd.) was used to generate an atmospheric pressure low-temperature plasma. The RF power was of two conditions: 52 W and 67 W. Its frequency was 13.56 MHz. The He gas (≥99.99%; Takamatsu Teisan Co.) flow rate was fixed at 1.40 slm using two mass flow controllers (SEC-400MK2; STEC Inc.). The O_2 gas (≥99.5%; Iwatani Sangyo Corp.) flow rate was fixed at 4.0 sccm using another mass flow controller (SEC-400MK3; STEC Inc.). The He/O_2 mixture was introduced into a glass

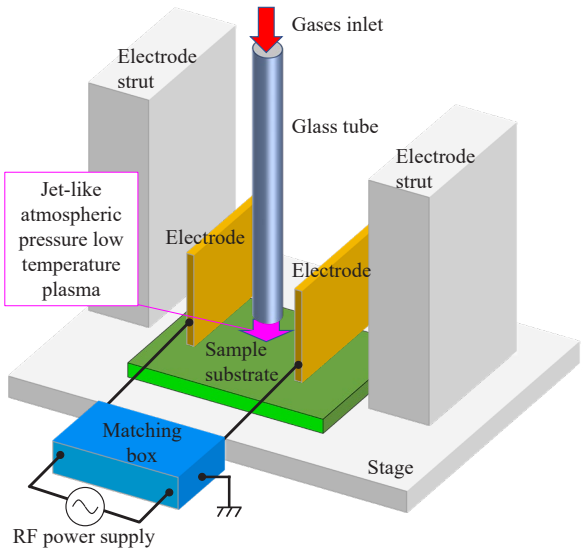

Fig. 1. Diagram of plasma treatment equipment.

tube with 2.5 mm inner diameter and 4.0 mm external diameter. The inter-electrode distance was 12.5 mm. The electrodes were separated from the stage by 7.0 mm. The distance between the glass tube tip and the stage was 5.0 mm. The plasma irradiation time per irradiation was 10 s. This was one set; it was repeated several times. A small thermocouple (ST-56 K-CA 0200 N-N; RKC Instrument Inc.) was used for surface temperature measurement during plasma irradiation. The surface profile after irradiation was examined using an atomic force microscope (AFM). The relation of the surface area to the surface roughness to the plasma irradiation condition was evaluated. The evaluation area of AFM was 5 × 5 μm^2. The surface coarseness and the surface area were analyzed from AFM results using WSxM [5].

3. Results and Discussion

3.1. Relation between plasma power and film thickness

Figure 2 shows the normalized PMMA film thickness dependence on the plasma irradiation time. For both RF power conditions, the normalized film thickness at 84.4 wt% was greater than that at 67.4

Table 1. Conditions for preparing films with different PMMA concentrations

PMMA concentration in solution [wt%]	Rotation rate in spin-coating [rpm]	Rotation time in spin-coating [s]	Baking temperature [°C]	Baking time [s]	PMMA concentration in film [wt%]
30.0	2400	20	100	60	67.4
30.0	1900	20	200	600	84.4

wt%. For RF power 67 W and irradiation time of 20–40 s, the etching rate of 67.4 wt% was 9.2 μm/min. That of 84.4 wt% was 10.3 μm/min. In both PMMA films, the film thickness became zero with irradiation time of approx. 50–60 s. The substrate surface temperature achieved during plasma irradiation was 102 °C. The temperature decreased to 47 °C within 15 s after plasma irradiation ceased. The glass-transition temperature, ceiling temperature, and pyrolytic temperature of PMMA were, respectively, 108 °C [6], 220 °C [7], and 327 °C [8]. The decomposition temperature by thermal oxidation is generally lower than the pyrolytic temperature [8]. Although a simple estimation, the temperature achieved during plasma irradiation increased by 23 °C at the second and subsequent times. Therefore, the surface temperature presumably reaches 150 °C after four plasma irradiation iterations. Because the pyrolysis and thermo-oxidative decomposition must be minor in this temperature range, film thickness is unlikely to decrease. This large etching rate might be ascribed to decomposition by O radicals produced by the Penning effect [9, 10]. The etching rate of approx. 10 μm/min is much higher than the removal rate for an organic film under dry processing [11–14]. At 67 W, the PMMA surface must be exposed to an intense reaction field.

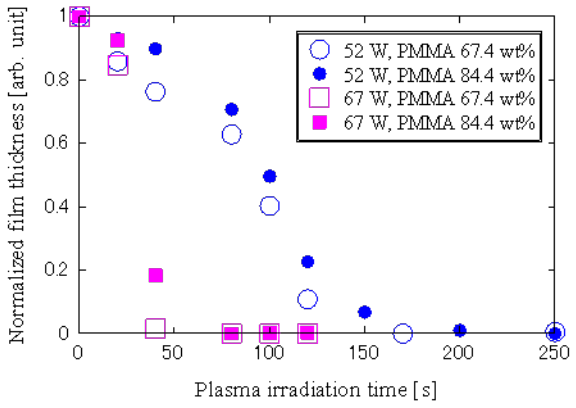

Fig. 2. Dependence of normalized PMMA film thickness on plasma power.

Table 2. Etching rate of each PMMA film at 52 W

PMMA concentration in film [wt%]	Plasma irradiation time [s]	Etching rate [μm/min]
67.4	20–40	1.19
67.4	80–120	3.3
84.4	20–40	0.40
84.4	80–120	3.0

At 52 W, a substrate surface temperature of 86 °C is presumably reached during plasma irradiation. The temperature decreased to 42 °C within 15 s after plasma irradiation ceased. This reaction field is less intense than the field at 67 W. Distinguishing the change of film thickness can be done easily by observing differences of PMMA contents. Results show that the film thickness with small PMMA content decreased compared with that of film with large contents.

Results presented in Fig. 2 indicate that the film thickness slope changed at irradiation times of 40–80 s. Table 2 shows the etching rates of PMMA films. The etching rate of 67.4 wt% PMMA film was three times higher than of 84.4 wt% PMMA film with irradiation time of 20–40 s. However, the different etching rates of the films were 10% with irradiation time of 80–120 s. The difference in etching rates by the irradiation time might be ascribed to increased substrate temperature through repeated exposure to plasma. At 52 W, the temperature achieved during plasma irradiation increases by 17 °C per iteration at second and subsequent times. When the plasma is irradiated more than five times, the surface temperature presumably reaches 150 °C. Even when the RF power is 52 W, O radicals must be produced by the Penning effect. Although the O-radical population is smaller at 52 W than at 67 W, the decomposition reaction proceeds at either RF power. The decomposition reaction by O radicals can be more active at 150 °C and higher temperatures. Therefore, the higher etching rate at 40–80 s is probably attributable to this active reaction. The 67.4 wt% PMMA film vanished during exposure to plasma within 130–150 s. The 84.4 wt% PMMA vanished within 160–170 s.

Figure 2 and Table 2 show that the film thickness changes that occur with respect to the plasma irradiation time differ depending on the PMMA concentration. Etching by plasma proceeds by active species produced in plasma [15, 16]. In this experiment system, O radicals must be among the main active species. This reaction is classified as a surface reaction. The reactant concentration is regarded as constant because etching constantly renews the surface. In this case, the etching rate increases concomitantly with increasing O-radical density. When the RF power is constant, its density is also constant. Under these conditions, the concentrations of the reactant PMMA differ. For a low PMMA concentration, the etching rate is

expected to be large. The etching rate of the 67.4 wt% PMMA film was higher than that of the 84.4 wt% PMMA film. Consequently, the results presented herein are inferred as reasonable.

3.2. Relation between plasma irradiation time and surface microstructure at 67 W

Figure 3 portrays surface morphologies and profiles of PMMA films irradiated by plasma at 67 W. Table 3 shows the full width at half maximum (FWHM) and height of a convex superior portion, the surface roughness, and the surface area. At both irradiation times, the nose shape of the convex structure on the 84.4 wt% PMMA film was more incisive than on the 67.4 wt% PMMA film. The height in the convex superior portion on the surface of each PMMA film was approx. 20–40 nm. For 20 s irradiation time, the FWHM of 67.4 wt% was 15 nm wider than that of 84.4 wt%; its variation was also 27 nm larger. The aspect ratio of the 67.4 wt% PMMA film was 0.12. That of the 84.4 wt% was 0.15. At 40 s irradiation time, the FWHM of 84.4

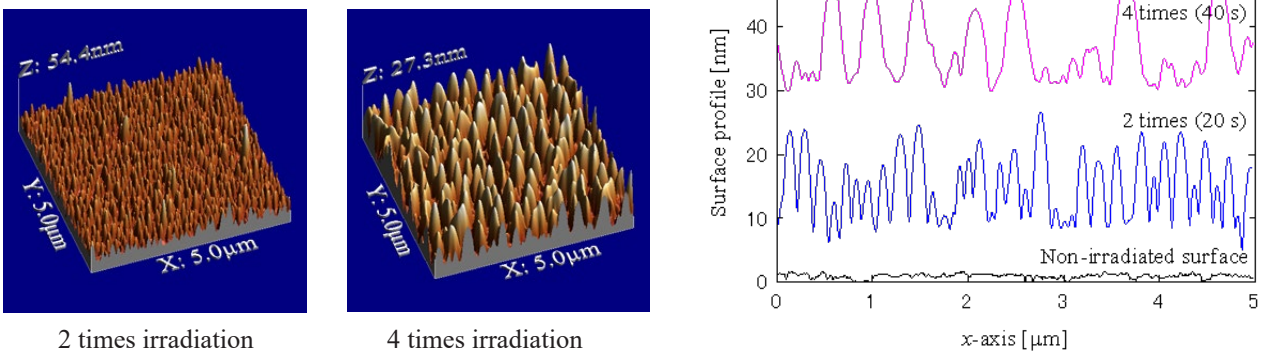

2 times irradiation (20 s) | 4 times irradiation (40 s) | Surface profile

(a) 67.4 wt% PMMA film

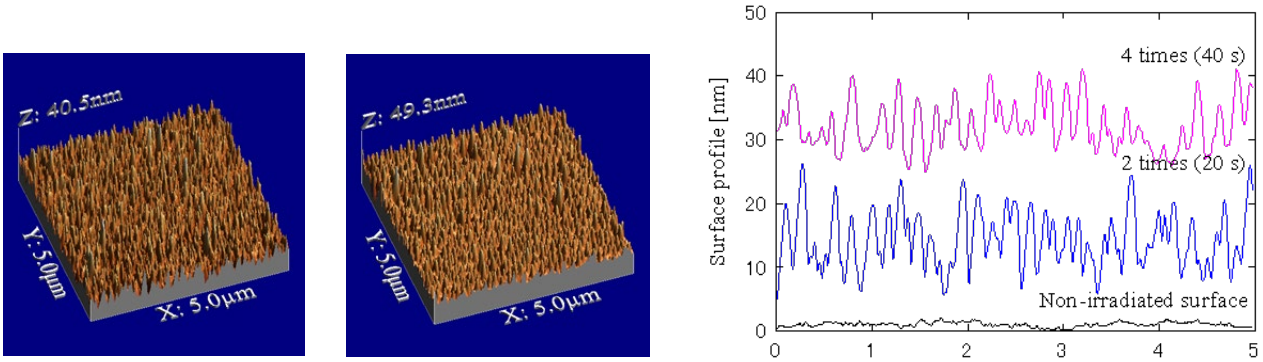

2 times irradiation (20 s) | 4 times irradiation (40 s) | Surface profile

(b) 84.4 wt% PMMA film

Fig. 3. Surface morphologies and profiles of PMMA films irradiated plasma at 67 W.

Table 3. Analysis of surface profiles of PMMA films irradiated plasma at 67 W

PMMA concentration in film [wt%]	Plasma irradiation time [s]	FWHM at convex structure [nm]	Height at convex structure [nm]	Surface roughness [nm]	Surface area [μm^2]
67.4	0	·	·	0.32 ± 0.06	25.03 ± 0.01
67.4	20	93 ± 43	11.4 ± 3.6	3.01 ± 1.25	25.37 ± 0.19
67.4	40	220 ± 24	14.1 ± 1.8	4.88 ± 0.41	25.31 ± 0.17
84.4	0	·	·	0.44 ± 0.20	25.04 ± 0.03
84.4	20	78 ± 16	11.9 ± 4.2	2.96 ± 0.45	25.60 ± 0.03
84.4	40	89 ± 16	10.9 ± 1.5	3.17 ± 0.02	25.39 ± 0.01

wt% film was 11 nm wider than that at 20 s. This aspect ratio was 0.12. However, the ratio of the 67.4 wt% PMMA film decreased to 0.07.

The surface roughness of the plasma unirradiated surface was small. Its surface was nearly equal to the projected area (25 μm^2). This is an optical flat surface. The 84.4 wt% PMMA film roughness changed little despite changes in the plasma irradiation time. At 20 s, the averaged roughness of the 67.4 wt% PMMA film was about equal to that of the 84.4 wt% film, but its variation was much greater. At 40 s, the roughness of the 67.4 wt% PMMA film was 1.5 times greater than that of the 84.4 wt% film. Even then, however, the surface area changed little.

The thickness of the 84.4 wt% PMMA film as about 20% when the irradiation time was 40 s (Fig. 2). However, the glass substrate becomes exposed on the 67.4 wt% PMMA film surface (Figs. 2 and 3). The reaction field of 67 W is intense. For that reason, the PMMA surface must be heated locally. In this situation, PMMA is heated to its melting temperature, which is around 160–220 °C [17–19]. It is probably softened. This large convex structure might be fabricated by mutually coalescing with some small convex structures. Consequently, large roughness is obtainable for 67.4 wt% PMMA films for 40 s irradiation time.

3.3. Relation between plasma irradiation time and surface microstructure at 52 W

Figure 4 portrays surface profiles and profiles of PMMA films irradiated by plasma at 52 W. Figure 5 portrays the relation between FWHM and the convex structure height portrayed in Fig. 4, in addition to the plasma irradiation time. When the irradiation time is 130 s, the 67.4 wt% PMMA film thickness vanished. The glass substrate was exposed. Even the 84.4 wt% PMMA film was very thin. In this situation, convex structures are heated to the melting temperature. They are probably softening. The neighboring convex structures might mutually coalesce. For that reason, results obtained at 130 s are excluded from Fig. 5. As shown in Figure 5(a), the convex structure width shows similar tendencies in both PMMA films. This width increases slightly

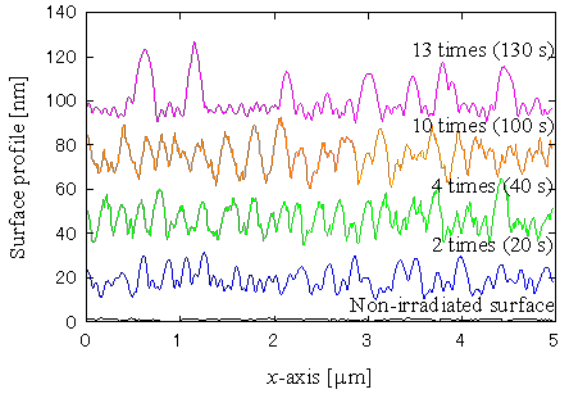

(a) 67.4 wt% PMMA film

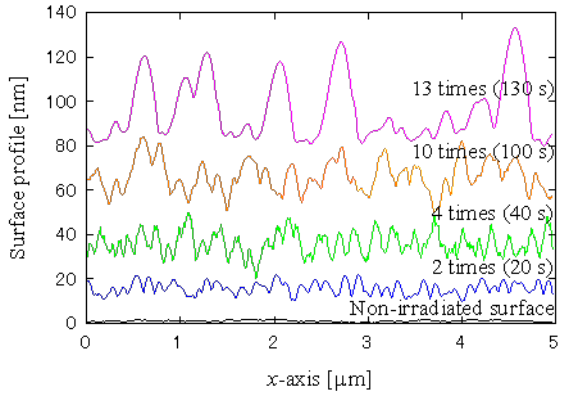

(b) 84.4 wt% PMMA film

Fig. 4. Surface profiles of PMMA films irradiated with plasma at 52 W.

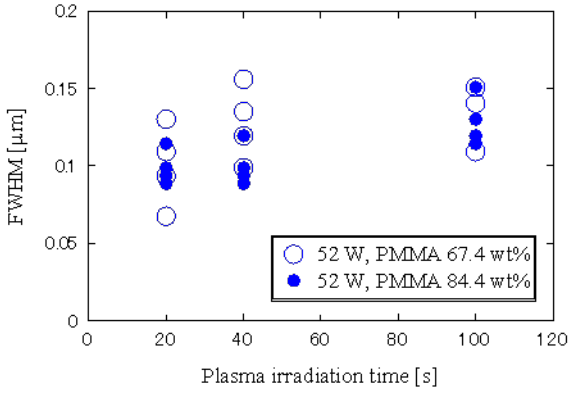

(a) FWHM at convex structure

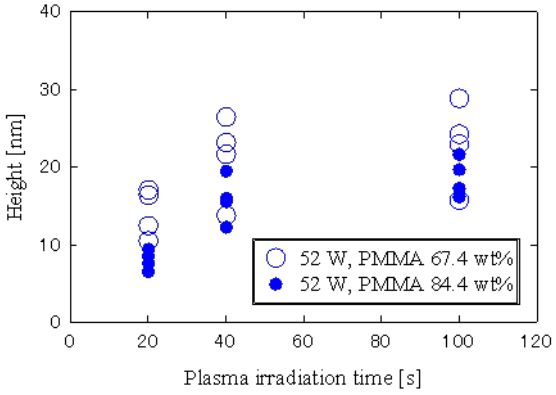

(b) Height at convex structure

Fig. 5. Dependence of the FWHM and the height on PMMA film surfaces on plasma irradiation time at 52 W.

with increasing irradiation time. As shown in Figs. 4 and 5(b), the convex structure height differed according to the PMMA concentration. Structures fabricated on the 67.4 wt% PMMA film surface were more orderly than those on the 84.4 wt% PMMA film. The 67.4 wt% PMMA film height was approx. 5–10 nm higher than the 84.4 wt% PMMA film height.

Figure 6 portrays the relation between the surface roughness, area, and irradiation time in a 5 × 5 μm^2 area. As depicted in Fig. 6(a), the 84.4 wt% PMMA film surface roughness increases in direct proportion to the irradiation time. However, for the 67.4 wt% PMMA film, its roughness increases at a high rate at 20 s; it subsequently increases gradually. At irradiation time of 100 s, the surface roughness of the 84.4 wt% PMMA film is greater than that of the 67.4 wt% PMMA film. The results shown in Fig. 6(b) suggest that the surface area is maximized at irradiation time of 40 s. That tendency is the same for both PMMA films. The area of the 67.4 wt% PMMA film was larger than that of 84.4 wt% PMMA film. At irradiation time of 100 s, the surface roughness of the 84.4 wt% PMMA film is large, but its surface area is rather small. Under these conditions, as portrayed in Fig. 4, the large convex structures increase, instead of decreasing in small structures. As presented in Fig. 5, FWHM increases concomitantly with increasing irradiation time. In principle, the surface area decreases concomitantly with decreasing convex structures, which show a high aspect ratio. Therefore, the surface area is considered to increase little as the surface roughness increases in the case of the 84.4 wt% PMMA film.

As Table 1 shows, films with different PMMA concentrations were fabricated by adjusting the preparation conditions. When baked in an oven, the PMMA film is heated from all directions. The solvent in a film volatilizes mainly from the film surface. The solvent on the substrate side moves to the surface side because a glass substrate exists at the bottom of the film. Some of the solvent cannot arrive at the surface: it remains in the film. Passages through which vaporized solvents moved in the polymer film, perhaps become open ceiling space. Micropores, which are exits, might form on the film surface. Figure 7 shows AFM images and surface profiles without plasma irradiation. The concave area can be confirmed on the surface, which is seemingly flat. The number of the concave areas on the 67.4 wt% PMMA film is greater than that on the 84.4 wt% PMMA film. In the 84.4 wt% film, large concave areas are formed, but they are few. Such large concave areas might be ascribed to bundling of the open ceiling space because of the high PMMA concentration. Generally, a solvent takes heat from the environment as it volatilizes. The vaporization heat of the solvent retained in the film might suppress the temperature increase, even when the surface is heated by plasma irradiation. The solvent is lactic acid ethyl, with a boiling point of 155 °C. The 67.4 wt% PMMA film is pre-baked at 100 °C for 60 s. However, the 84.4 wt% PMMA film is pre-baked at 200 °C for 600 s. Some small amount might be left in the solvent in the 84.4 wt% PMMA film. Therefore, as portrayed in Figs. 4–6, a more orderly convex structure might be fabricated on the 67.4 wt% PMMA film than on the 84.4 wt% PMMA film.

Convex structures with 200-nm pitch were fabricated on the 67.4 wt% PMMA film when irradiating plasma at 52 W for 40 s. The passages of volatilized solvents can play a role in fabricating microstructures. Because of different experiment conditions used for this study, direct comparison might be difficult, but at least two conditions, which are an approx. 0.1 μm/min etching rate and approx. 108 °C (T_g of PMMA [6]) temperature, have been

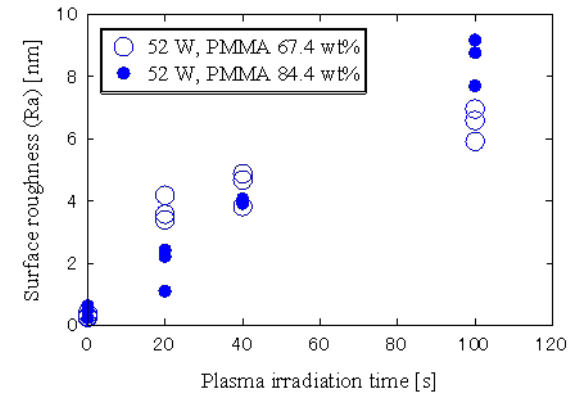

(a) Surface roughness

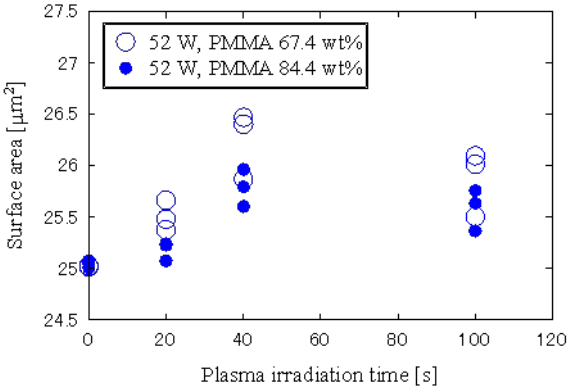

(b) Surface area

Fig. 6. Dependence of the surface roughness and the surface area on PMMA film surfaces on plasma irradiation time at 52 W.

reported as important for fabricating microstructures on PMMA [20]. Present conditions might not be desirable because etching rates are very high at any RF power. At least threefold improvement in the aspect ratio might be necessary to achieve good antifouling functionality [21–23]. As subjects for future study, we intend to clarify microstructure formation mechanisms and to develop techniques for their control.

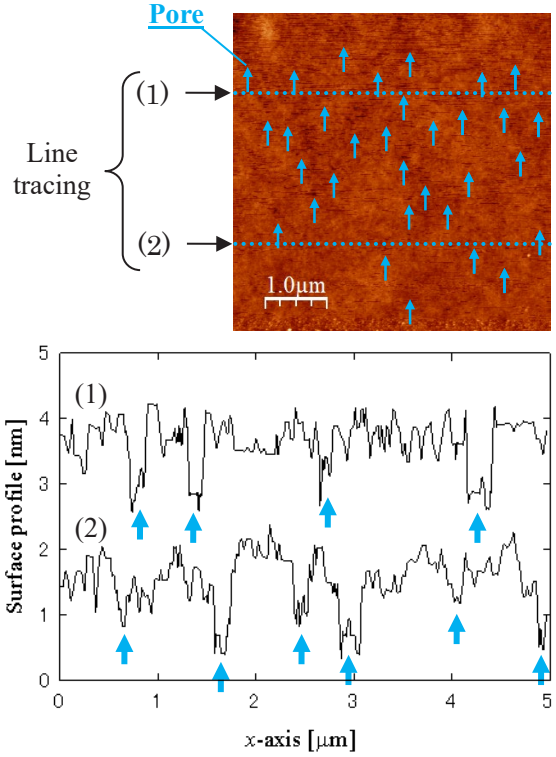

(a) 67.4 wt% PMMA film

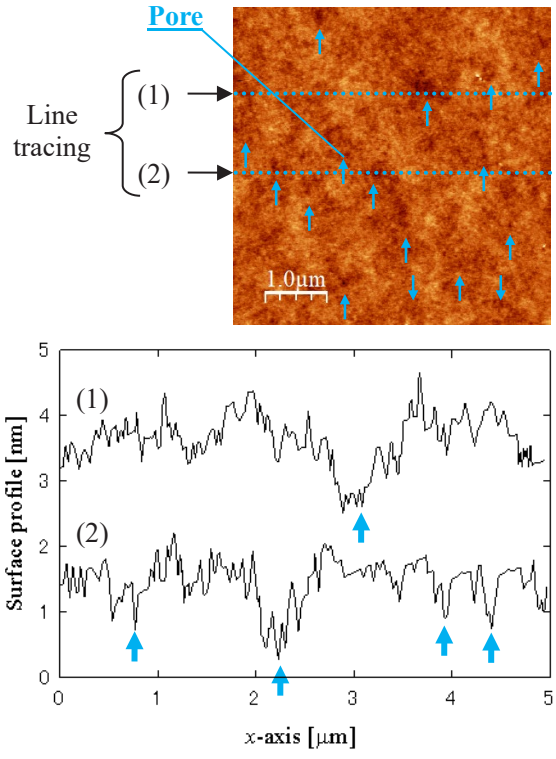

(b) 84.4 wt% PMMA film

Fig. 7. Surface morphologies and profiles of PMMA films without plasma irradiation.

4. Conclusion

For this study, after fabricating microstructures on films with different PMMA concentrations, we examined their surface profiles using atmospheric pressure low-temperature plasma.

Using RF power of 67 W, the etching rates of PMMA films were around 10 μm/min. The film surface must be exposed to intense reaction fields. The surface temperature reaches more than 150 °C by local heating. The convex structure on the film with low PMMA concentration (67.4 wt%) has a rounded tip. For the high concentration (84.4 wt%) film, the nose structure shape remains incisive.

For RF power of 52 W, the etching rate was a few micrometers per minute. This reaction field is milder than the field at 67 W, but the surface temperature exceeds 100 °C. Structures fabricated on the 67.4 wt% PMMA film surface were more incisive and orderly than those of the 84.4 wt% PMMA film.

References

1. M. Shimomura, "Biomimetics, National Science Museum 16", *Tokai University Press*, 2 (2016).
2. J. Knippers, K. G. Nickel, and T. Speck, "*Biomimetic Research for architecture and Building Construction, Biological Design and Integrative Structures, Biologically Inspired Systems Vol. 8*", Springer, (2016) 69.
3. C. Tendero, C. Tixier, P. Tristant, J. Desmaison, and P. Leprince, *Spectrochemica Acta*, **B61** (2006) 2.
4. C. Jen-shin, *J. Plasma Fusion Res.*, **82** (2006) 6288.
5. I. Horcas, R. Fernández, J. M. Gómez-Rodríguez, J. Colchero, J. Gómez-Herrero, and A. M. Baro, *Rev. Sci. Instrum.*, **78** (2007) 013705.
6. V. Sankar, T. Suresh Kumar, and K. Panduranga Rao, *Trends Biomater. Artif. Organs,* **17** (2004) 24.
7. Z. Osawa, *Materials Life*, **8** (1996) 165 (in Japanese).
8. H. Ohtani and S. Tsuge, *Polymer* (Kobunshi), **46** (1997) 394 (in Japanese).
9. M. Kogoma, *J. Surf. Finish. Soc. Jpn*. (Hyomen Gijutsu), **58** (2007) 779 (in Japanese).
10. T. Murakami, *J. Plasma Fusion Res.*, **92** (2016)

688 (in Japanese).
11. T. Ishijima, K. Nosaka, Y. Tanaka, Y. Uesugi, Y. Goto, and H. Horibe, *Appl. Phys. Lett.,* **103** (2013) 142101.
12. M. A. Worsley and S. F. Bent, N. C. M. Fuller and T. Dalton, *J. Appl. Phys.,* **100** (2006) 083301.
13. S.-G. Park, H.-Y. Song, and B.-H. O, *J. Vac. Sci. Technol. B*, **19** (2001) 1841.
14. C. K. Huynh and J. C. Mitchener, *J. Vac. Sci. Technol. B*, **9** (1991) 353.
15. K. Shinagawa, H. Shindo, K. Kusaba, T. Koromogawa, J. Yamamoto, and M. Furukawa, *Jpn. J. Appl. Phys.,* **40** (2001) 5856.
16. E. P. G. T. van der Ven and H. Kalter, *Electrochem. Soc. Ext. Abst.*, **76-1** (1976) 332.
17. N. Chand and S. R. Vashishtha, *Bull. Mater. Sci.,* **23** (2000) 103.
18. Xf. Wang and Zm. Huang, *Chin. J. Polym. Sci.,* **28** (2010) 45.
19. R. Gregorio Jr. and N. Chaves Pereira de Souza Nociti, *J. Phys. D: Appl. Phys.,* **28** (1995) 432
20. A. Matsuo, S. Takagi, T. Nishiyama, M. Yamamoto, E. Sato, and H. Horibe, *J. Photopolym. Sci. Technol.,* **31** (2018) 369.
21. T. Nishino, H. Tanigawa, and A. Sekiguchi, *J. Photopolym. Sci. Technol.,* **32** (2019) 661.
22. A. Sekiguchi, Y. Matsumoto, H. Minami, T. Nishino, H. Tanigawa, K. Tokumaru, and F. Tsumori, *J. Photopolym. Sci. Technol.,* **31** (2018) 121.
23. T. Nishino, H. Tanigawa, A. Sekiguchi, and H. Mayama, *J. Photopolym. Sci. Technol.,* **32** (2019) 383.

Journal of Photopolymer Science and Technology
Volume 34, Number 4 (2021) 393−399 ©2021SPST

Water-Repellency Model of the Water Strider, *Aquarius paludum paludum*, by the Curved Structure of Leg Micro-Hairs

Kaoru Uesugi

Department of Mechanical Systems Engineering,
Graduate School of Science and Engineering, Ibaraki University,
4-12-1, Nakanarusawa-cho, Hitachi-city, Ibaraki, 316-8511, Japan.
kaoru.uesugi.biomech@vc.ibaraki.ac.jp

Water-repellent surfaces that mimic various water-repellent surfaces of living things have been developed using photolithography technology. The water-repellency of water striders in particular has gotten a lot of attention. Micro-hairs on their legs are tilted and curved at the tip. These curving micro-hairs contribute to water-repellency properties and various reports have considered the property origins. However, the water-repellency function produced by the curved micro-hairs has not been compared with the dynamic situation (when water striders are rowing their legs), that is when there is a directly measured leg-rowing force. Therefore here, first we discussed water-repellent properties using the relationship between Laplace pressure and water pressure caused by rowing of the insect legs. In order to obtain the Laplace pressure when affected by the curved micro-hairs, a water-repellency model was proposed. To construct this new model, we measured the morphological information of micro-hairs on the tip of the middle leg (tarsus and pretarsus) and fit the curved properties of the micro-hairs to a log function. Then, the water-repellency model was constructed with the fitting curve. As a result, we derived the maximum value of Laplace pressure ΔP as 3.4 kPa. This maximum value was sufficiently larger than the water pressure (546 Pa) caused by the rowing motion of the water strider's middle leg. Thus, we concluded that the water-repellent function due to the curved micro-hairs worked when the water strider was rowing its legs.
Keywords: Laplace pressure, Micro-hair, Surface morphology, Surface tension, Water repellency, Water strider

1. Introduction

Hydrophobic-hydrophilic surfaces in engineering fields have been developed using photolithography technology. This technology allows nano- and micro-scale structures to be fabricated on the surfaces [1-6]. The micro-structures are fabricated on various surfaces to obtain hydrophobic-hydrophilic surfaces. The surfaces which are realized by photolithography technology have various applications. For example, the surfaces are applied for functions such as decreasing liquid friction and directionally controlling droplet slip [1], implementing the water harvest function via dewing [3], and implementing the self-cleaning function [6]. In order to control the surfaces more reliably, there is also a hierarchical structure that combines photolithography technology and emulsification [5].

Because photolithography technology can make micro-scale structure arrays, it has been used to produce surfaces mimicking surfaces of various living things. The water-repellency function of micro-structures is of interest in biomimetic approaches and engineering applications. Water striders have many micro-hairs on their leg surfaces (Fig. 1). The micro-hairs have a water-repellency function and the legs are not wetted by water [7-11]. This water-repellency function can be explained by the Cassie-Baxter state of wetting [7-9]. Micro-hair structure has been mimicked by various techniques in the development of water-repellent surfaces [12-17].

Received April 4, 2021
Accepted May 6, 2021

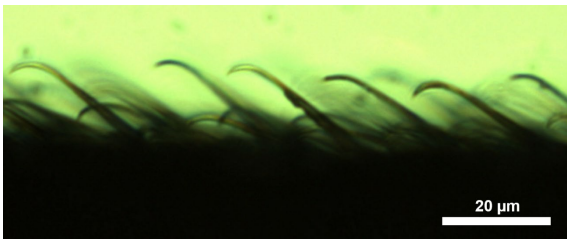

Fig. 1. Microscopic image showing the surface of a water strider's leg (around the tarsus and pretarsus). The micro-hairs are tilted on the leg surface, and the tip of each micro-hair is curved.

In order to develop more effective water-repellent surfaces, the relationship between the water strider's micro-structures and the water-repellency function needs to be better understood. Therefore, previously we proposed a water-repellency model of the water strider [18]. Micro-hairs present on the legs are tilted (Fig. 1) and tilted micro-hairs are recognized to enhance water-repellency [19]. Tilted micro-hairs interact with the free surface to generate directionally anisotropic adhesive forces that facilitate locomotion [20]. Additionally, the horizontal arrangement of micro-hairs provides better resistance than the simply tilted and randomly arranged micro-hairs [19]. In order to keep the horizontal arrangement, micro-hairs are bent over at the tip in a curve (Fig. 1) [21]. Because the micro-hairs are curved toward the tip of the legs with the tips of the distally tapered micro-hairs pointing downward, our previous model considered that the micro-hairs were cylindrical and in a parallel series. In our previous study [18], we focused on the water surface which contacts with the micro-hair surface (cylindrical curved surface) at the top of the micro-hair bend (where the hairs are horizontally laying). In that study, we also considered the dynamic situation in which the water strider was rowing its legs, and we compared Laplace pressure calculated by the previous model and the water pressure calculated from directly measured leg-rowing force. The leg-rowing force was measured directly with a special system [22].

For the next stage, in this study, we have looked at the relationship between the water surface and the curved tip of the micro-hairs. We assumed that this curve enhanced the water-repellency function in the dynamic situation because tilted micro-hairs were effective for enhancing water-repellency. However, the water-repellency function produced by the curved micro-hairs was not compared with the dynamic situation (i.e., when the water strider is rowing its legs) with the directly measured leg-rowing force. When water striders move on water surfaces, water is not pushed into the space between the micro-hairs by the water pressure caused by the leg-rowing motion. If the excess pressure outside the space is larger than the maximum Laplace pressure, the water surface is forced into the space between the hairs. This means that the water-repellency properties of the legs are lost.

In this study, we measured morphological information of the micro-hairs and proposed a water-repellency model. Then, we compared Laplace pressure calculated by our new model to the water pressure derived from the directly measured leg-rowing force. By using the new model, we showed the deformation condition of the water surface contacting with the micro-hairs when the pressure changed.

2. Observation of water strider micro-hairs

2.1. Insect specimen

Water striders (*Aquarius paludum paludum*) were collected from a pond on the Suita campus of Osaka University (Suita, Osaka, Japan). After the initial collection, they were fed and propagated in an aquarium (at room temperature, from 20 to 25 °C) until they became adults. Microscope observations were made for one adult female insect.

2.2. Observation of micro-hairs

Micro-hairs on the surface of a middle leg tip (tarsus and pretarsus) of one adult female insect were observed through a microscope (ECLIPSE Ti2-E, Nikon Corporation, Tokyo, Japan) under 30x magnification (Plan APO 20x/0.75 DIC N2 with 1.5x magnification function of the microscope). The observation was carried out in the atmosphere. Microscopic images were captured with a CCD camera (DFK21AU618.AS, The Imaging Source Asia Co., Ltd., Taipei, Taiwan).

2.3. Measurement of morphological information of micro-hairs

Image analyzing software (ImageJ 1.53a) was used for all the morphological information measurements of micro-hairs. Coordinate data of the upper outline (blue dotted line of Fig. 2-a) of the micro-hairs were obtained by the "Multi-point" tool. Coordinate data of points were obtained from the tip of the micro-hair to the end point of the curved portion. We selected one micro-hair from each of five microscopic images obtained for the tip of a

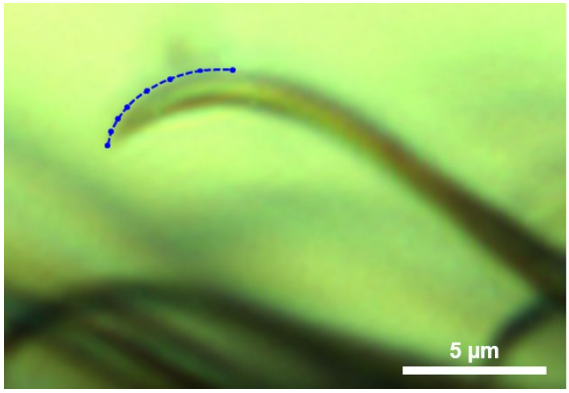

(a)

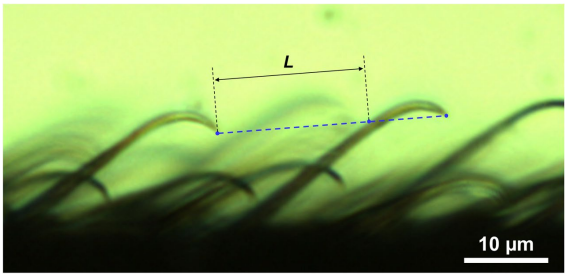

(b)

Fig. 2. Morphological information is acquired from microscopic images. Coordinate data of points are obtained from the tip of the micro-hair to the end point of the curved portion (a). Distance L between the tips of two micro-hairs is obtained (b).

middle leg of one adult female and analyzed five to seven points along the hair in each image.

Distance between two selected micro-hairs "L" was measured. To do this, the tip of one micro-hair and that of another were connected by a line drawn by the "Straight" tool (Fig. 2-b). Then, the length of a line which connected the tip of one micro-hair and an intersecting point of the line and the outline of the other micro-hair was measured. We analyzed 20 different distances in each of the five microscopic images (the same images used for measuring coordinate data of points).

2.4. Curve fitting of the micro-hair outline

Because the profile was similar to a log function, the outline curves of the tip of the micro-hair (blue dotted line; Fig. 3) were fitted by Eq. 1.

$$f(x) = a \times \exp\left(-\frac{x}{b}\right) \qquad (1)$$

Here "a" and "b" are constants. We assumed that the coordinate of the tip of a micro-hair was the zero point. In order to calculate the constants, the "solver"

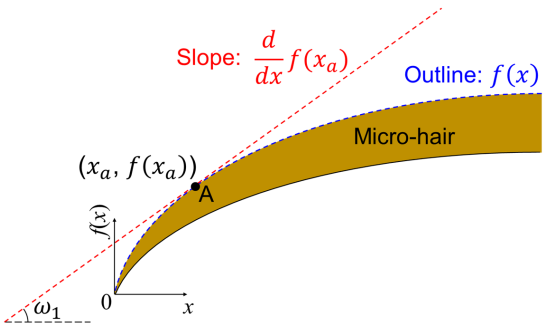

Fig. 3. Tangential line at point A where the outline of a micro-hair and the water surface are contacting. The slope of the tangential line (ω_1) is derived from the differential of the fitting curve.

which was an add-in of Excel (Microsoft Office 2019, Microsoft Corporation, WA, USA) was used. All measured coordinate data of points (in each of five microscopic images) were coupled and fitted in one fitting curve.

3. Water-repellency model of curved micro-hairs

We considered a relationship between the water pressure around the micro-hairs and the intersection of the surface of the micro-hairs and the water surface. For simplification, we did not consider the shape of the micro-hair tip or the behavior of the water surface on the micro-hair tip. Additionally, we did not consider micro-hair deformation by the water surface.

First, we explain the relationship between the morphology of the curved micro-hairs and that of the water surface. Figure 4 shows a cross-sectional image for the micro-hairs contacting with a deformed water surface. The morphology of the water surface between micro-hairs was assumed to be a simple sphere (each curvature is the same) (center, O; radius, R). The water surface contacts at point A, and the contact angle between the water surface and the surface of the micro-hairs is φ at point A. The angle between the water surface and the horizontal line is θ at point A. The angle between a tangential line of the outline of the micro-hair and the horizontal line at point A is ω_1. The angle between the tangential line of the outline of the micro-hair and the vertical line is ω_2 at point A. The distance between the micro-hairs is L. The distance between the center of two neighboring micro-hairs and point A is l. The angle ω_1 is shown as Eq. 2 (Fig. 3).

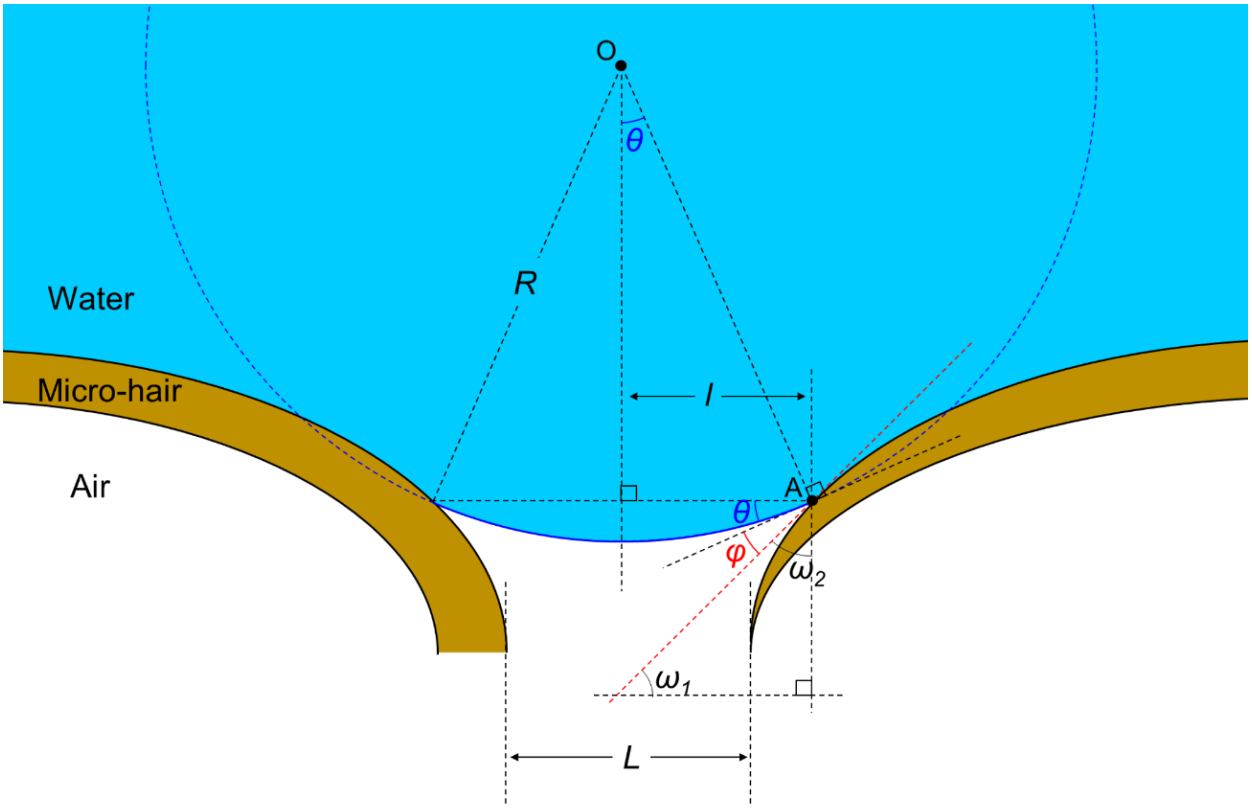

Fig. 4. Cross-sectional image of the deformed shape of the water surface that contacts with the curved micro-hairs. Brown areas are the micro-hairs, the blue area represents water, and the white area is the air layer.

$$\omega_1 = \tan^{-1}\frac{d}{dx}f(x) \qquad (2)$$

The angle θ is shown as Eq. 3.

$$\theta = 90° - \varphi - \omega_2 = \omega_1 - \varphi \qquad (3)$$

The radius R is shown as Eq. 4.

$$R = \frac{l}{\sin\theta} = \frac{\frac{L}{2}+x}{\sin\theta} \qquad (4)$$

Then, we explain the relationship between the water pressure around the micro-hairs and the radius R. By taking account of the surface geometry of the water surface, the water pressure can be given by the Laplace pressure. The Laplace pressure ΔP is shown as Eq. 5.

$$\Delta P = \gamma\left(\frac{1}{R}+\frac{1}{R\prime}\right) \qquad (5)$$

Here R and R' are the curvatures of the water surface, and γ is surface tension of water. Because the geometry of the water surface is assumed to be the simple sphere and R and R' are the same value, Eq. 6 is gotten.

$$\Delta P = \frac{2\gamma}{R} \qquad (6)$$

By substituting Eq. 2, Eq. 3 and Eq. 4 into Eq. 6, we get the water pressure (Laplace pressure ΔP).

4. Results

4.1. Morphological information of water strider's micro-hairs

Figure 5 shows the coordinate data of the upper outline of the micro-hairs and the fitting line. By fitting coordinate data of points of the micro-hair tip to Eq. 1, we obtained the constants "*a*" and "*b*". The fitting curve is shown as Eq. 7.

$$f(x) = 1.8597 \times \exp\left(-\frac{x}{0.9132}\right) \qquad (7)$$

The distance between micro-hairs "*L*" was 12.9 ± 6.6 μm (mean ± SD).

4.2. Relationship between the water pressure around the micro-hairs and the intersection of the surface of the micro-hairs and the water surface

By using Eq. 2, Eq. 3 and Eq. 4 in Eq. 6, we can get the relationship between the water pressure

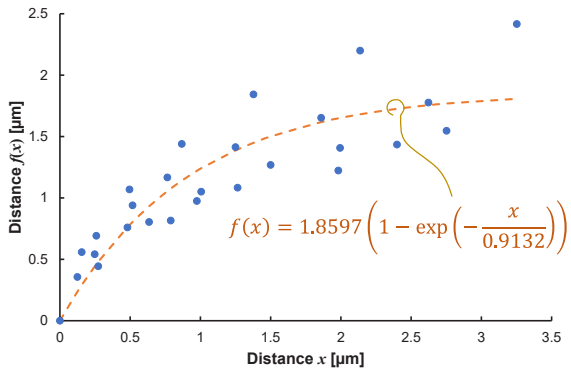

Fig. 5. Fitting curve (orange dotted line) and coordinate information of the surface of the micro-hairs (blue points). Five micro-hairs are used to get coordinate information.

(Laplace pressure ΔP) around the micro-hairs and the intersection of the surface of the micro-hairs and the water surface. By assuming the surface tension of water γ as 72.75 μm and the contact angle between water and micro-hair θ as 124.8 ° [23], Fig. 6 is gotten. When x is below 2.62 μm, ΔP increases as x decreases (l decreases). When x is zero, ΔP is 3.4 kPa and this value is the maximum Laplace pressure (R = 42.8 μm). When ΔP is zero, x is about 0.32 μm.

5. Discussion

Micro-hairs found on water strider legs are tilted and bent over at the tip. These curved micro-hairs are observed on surfaces of various insects and contribute to water-repellency properties and pressures (plastron pressure and Laplace pressure) which contribute to respiration [21,24]. However, most reports have considered the water-repellency model of curved micro-hairs in a static situation. The water-repellency function has not been compared with a dynamic situation (when the water strider is rowing its legs) with directly measured leg-rowing force. Therefore, we discuss water-repellent properties using the relationship between Laplace pressure which is derived from the newly proposed model of curved micro-hairs and water pressure caused by rowing of the insect middle legs.

Figure 6 shows the relationship between the Laplace pressure ΔP and distance x when the water surface contacts at the micro-hair tip. When x is below 0.32 μm, ΔP becomes positive. This means that the water surface contact point A moves toward the micro-hair tip, and the shape of the water surface becomes a convex curve (Fig. 6-a). On the other hand, when ΔP becomes negative, the shape of the water surface becomes a concave curve (Fig. 6-b). When x is below 2.62 μm, ΔP increases with a negative correlation and the maximum value is 3.4 kPa (x = 0 μm). When ΔP exceeds the maximum Laplace pressure, the water surface contact point A is on the tip of the micro-hair, and the micro-hair pierces the water surface, putting the tip in the water. Then the water-repellency function of the micro-hairs may be lost. The above discussion shows that the micro-hair tips of the water strider provide the water-repellency function by their curved shape. In fact, one study has reported that the curved micro-hairs of insects contribute to water-repellency [21].

The maximum Laplace pressure derived by this study is smaller than the Laplace pressure (35.2 kPa) derived from the model considering the horizontal arrangement of micro-hairs (as cylinders) [18]. Additionally, the maximum pressure is considered in this study as under a static situation (micro-hairs touch on the water surface statically). Regarding the question: "Does the water-repellency function of the curved micro-hairs work in the dynamic situation when the water strider is rowing its legs?" we see that the value derived in this study is sufficiently larger than the water pressure (546 Pa) caused by the rowing motion of the water strider's middle leg and calculated from directly measured leg-rowing force [18]. The water pressure was calculated from directly measured leg-rowing force. Therefore, we consider that the curved micro-hairs can contribute to the water-repellency function in rowing motion of the insect.

Because our new model considers only the curved micro-hair structure, a more accurate model is needed. However, even comparison at the order level of ΔP derived by the new model and the water pressure derived by leg-rowing force shows that the water-repellent function of the curved micro-hairs is also effective for a dynamic situation such as when the water strider is rowing its legs. In the future, we will propose a model the fuses morphological information such as the curved tip shape and the cylindrical surface of the micro-hairs and discuss their water-repellency properties in more detail.

6. Conclusion

In this study, we looked at the water-repellent properties resulting from the curved micro-hairs of water striders. First, we measured morphological information of the micro-hairs and the curved shape of the micro-hairs was fit to the log function. Then, the water-repellency model was constructed with

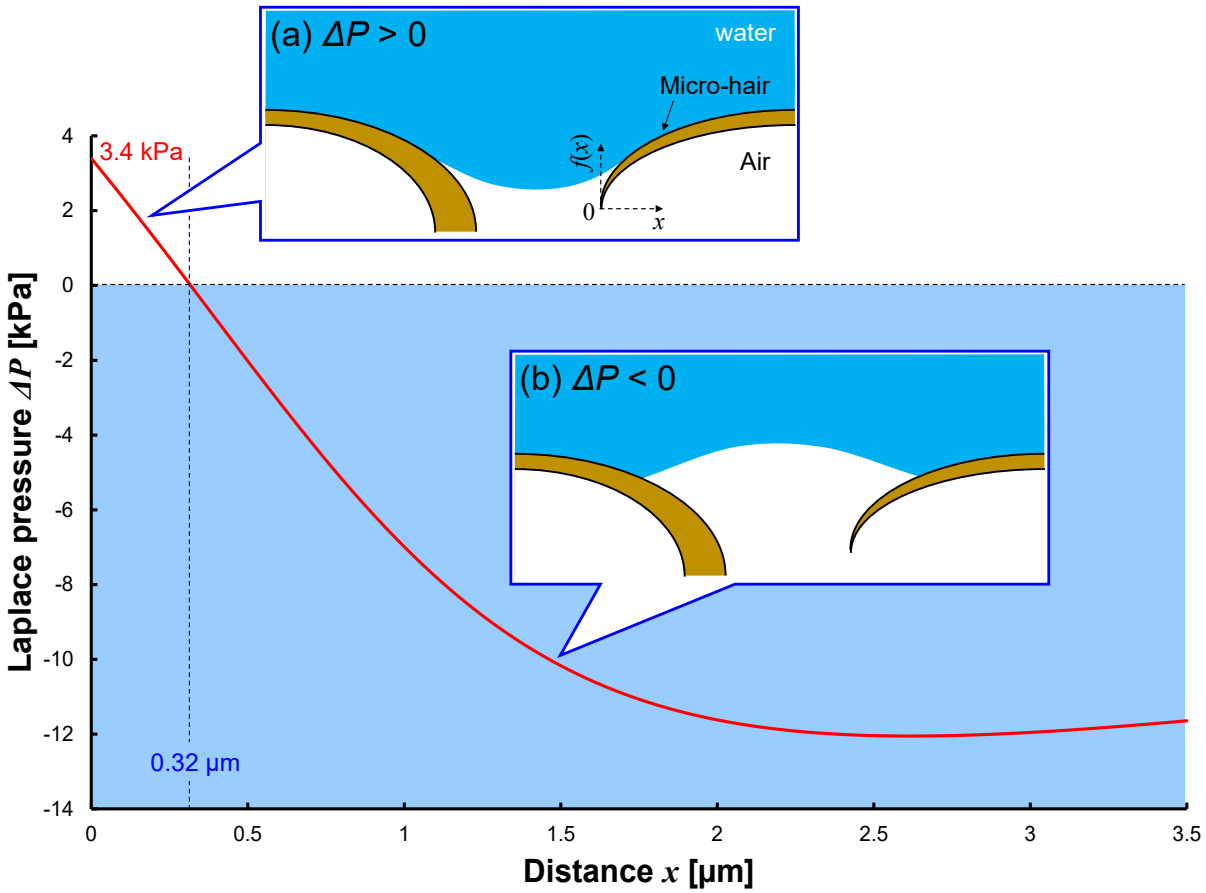

Fig. 6. The relationship between the water pressure around the micro-hairs and the position of intersection point of the surface of the micro-hairs and the water surface. The maximum Laplace pressure is obtained as 3.4 kPa.

the fitting curve. As a result, maximum value of Laplace pressure ΔP is derived as 3.4 kPa from the model when the water surface contact at the tip of the micro-hair. The maximum value was considered in statically situation (without the rowing of insect's legs). However, the maximum value is sufficiently larger than the water pressure (546 Pa) caused by the rowing motion of the water strider's middle leg. Thus, it is considered that the water-repellent function by bending micro-hairs works when water strider rowing its legs.

References

1. C. H. Choi, U. Ulmanella, J. Kim, C. M. Ho, and C. J. Kim, *Phys. Fluids*, **18** (2006) 087105.
2. X. Zhang, J. Zhang, Z. Ren, X. Zhang, T. Tian, Y. Wang, F. Dong, and B. Yang, *Nanoscale*, **2** (2010) 277.
3. A. Lee, M. W. Moon, H. Lim, W. D. Kim, and H. Y. Kim, *Langmuir*, **28** (2012) 10183.
4. K. Tadanaga, *J. Ceram. Soc. Japan*, **121** (2013) 819.
5. T. Li, M. Paliy, X. Wang, B. Kobe, W. M. Lau, and J. Yang, *ACS Appl. Mater. Interfaces*, **7** (2015) 10988.
6. A. Fernández, A. Francone, L. H. Thamdrup, A. Johansson, B. Bilenberg, T. Nielsen, M. Guttmann, C. M. S. Torres, and N. Kehagias, *J. Micromech. Microeng.*, **27** (2017) 045020.
7. X. Gao and L. Jiang, *Nature*, **432** (2004) 36.
8. X. Q. Feng, X. Gao, Z. Wu, L. Jiang, and Q. S. Zheng, *Langmuir*, **23** (2007) 4892.
9. G. S. Watson, B. W. Cribb, and J. A. Watson, *Acta Biomater.*, **6** (2010) 4060.
10. D. L. Hu and J. W. M. Bush, *J. Fluid Mech.*, **644** (2010) 5.
11. Y. Xue, H. Yuan, W. Su, Y. Shi, and H. Duan, *Proc. R. Soc. A Math. Phys. Eng. Sci.*, **470** (2014) 10.1098/rspa.2013.0832.
12. F. Shi, Z. Wang, and X. Zhang, *Adv. Mater.*, **17**

(2005) 1005.
13. X. Wu and G. Shi, *J. Phys. Chem. B*, **110** (2006) 11247.
14. H. Wu, R. Zhang, Y. Sun, D. Lin, Z. Sun, W. Pan, and P. Downs, *Soft Matter*, **4** (2008) 2429.
15. X. Yao, Q. Chen, L. Xu, Q. Li, Y. Song, X. Gao, D. Quéré, and L. Jiang, *Adv. Funct. Mater.*, **20** (2010) 656.
16. X. Liu, J. Gao, Z. Xue, L. Chen, L. Lin, L. Jiang, and S. Wang, *ACS Nano*, **6** (2012) 5614.
17. F. Bai, J. Wu, G. Gong, and L. Guo, *ACS Appl. Mater. Interfaces*, **6** (2014) 16237.
18. K. Uesugi, H. Mayama, and K. Morishima, *J. Photopolym. Sci. Technol.*, **33** (2020) 185.
19. J. W. M. Bush, D. L. Hu, and M. Prakash, Adv. In Insect Phys., **34** (2007) 117.
20. M. Prakash and J. W. M. Bush, *Int. J. Non. Linear. Mech.*, **46** (2011) 607.
21. D. J. Crisp and W. H. Thorpe, Discuss. Farady Soc., 3 (1948) 210.
22. K. Uesugi, H. Mayama, and K. Morishima, Manuscript in preparation.
23. P. J. Wei, S. C. Chen, and J. F. Lin, *Langmuir*, **25** (2009) 1526.
24. P. P. Goodwyn, *Springer Science & Business Media*, S. N. Gorb, Ed., 1st ed. (2009).

Journal of Photopolymer Science and Technology
Volume 34, Number 4 (2021) 401−410 ©2021SPST

Development of Bile Direct Stent Having Antifouling Properties by Atmospheric Pressure Low-Temperature Plasma

Atsushi Sekiguchi[1*, 3, 5], Masashi Yamamoto[2], Takuya Kumagai[2], Youichiro Mori[2], Hiroko Minami[3], Masayasu Aikawa[4], and Hideo Horibe[5]

[1] Osaka Prefecture University, Department of Physics and Electronics
11-1 Gakuen-cho, Naka-ku, Sakai, Osaka 599-8531, Japan
[2] National Institute of Technology, Kagawa College,
Department of Electrical and Computer Engineering
335 Chokushi-cho, Takamatsu, Kagawa 761-8058, Japan
[3] Litho Tech Japan corporation
2-6-6 Namiki, Kawaguchi, Saitama 332-0034, Japan
[4] Saitama Medical University, International Medical Center
1397-1, Yamane, Hidaka, Saitama 350-1298, Japan
[5] Osaka City University, Department of Physics and Electronics
3-3-138 Sugimoto-cho, Sumiyoshi-ku, Osaka 558-8585, Japan
**tas35035@osakafu-u.ac.jp*

Biomimetics (or biomimicry) is a field of technologies based on imitating various functions and properties of organisms. Waterproof products, which are inspired by lotus leaves with super-water-repellent fine structures, are a well-known example of biomimetics. The present study examined the surface structure of snail shells, which exhibit oil repellency (oleophobic property). Snail shells have nanoporous structures with nanoholes on the scale of 200–400 nm. When water enters these nanoholes, the surface is covered by thin water films. The oil can be repelled by the water film. These structures are known as superhydrophilic nanostructures. An earlier report discussed our efforts to create such nanostructures using a nanoimprinting method and assessed the feasibility of application to the inner walls of biliary stents. This involves a labor-consuming two-stage process involving creating nanostructures on a film surface, then rolling the film into a tube. In addition, the nanoimprinting mold made via electron beam lithography is costly and unsuitable for mass production.

To overcome these issues, we sought to develop elemental technologies for providing antifouling properties to biliary stents, which are made of polyethylenes (PEs), by forming nanostructures directly on the inner surface, using atmospheric pressure low-temperature plasma. We formed nanostructures on the inner walls of PE tubes of varying diameters under varying plasma conditions. We then examined the resulting structures and effects of the antifouling properties thus imparted.

Keywords: Biomimetics, Snail shell structure, Super-nanohydrophilic (structure), Bile duct cancer, Biliary obstruction, Biliary stent, Atmospheric pressure low-temperature plasma

1. Introduction

Applying biomimetics, we sought to develop technologies to improve the antifouling properties of a substrate surface independent of substrate shape. Biomimetics seeks to create artificial structures that imitate diverse functions exhibited by living

Received March 28, 2021
Accepted April 28, 2021

organisms [1–3]. As the saying goes, *There are no dirty snails*, snail shells have long been known to exhibit superior antifouling performance. Snail shells feature nanoporous surface structures on the scale of 200 nm–400 nm (Fig. 1).

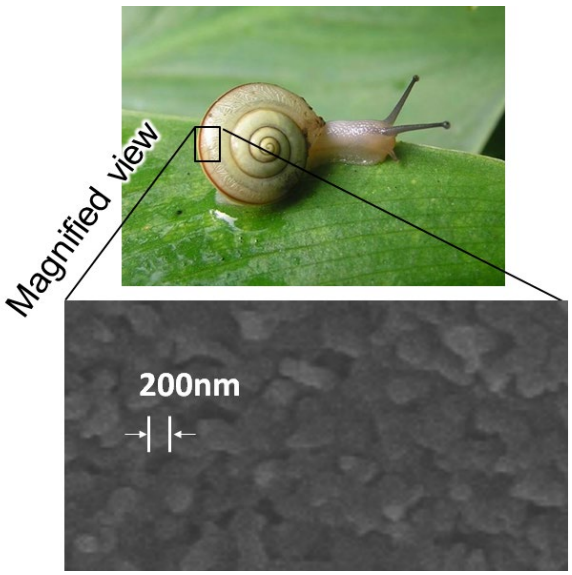

Fig. 1. Snail shell structure.

Water entering these nanoholes forms a thin film of water on the surface, which repels oil and other fouling substances. Referred to as superhydrophilic nanostructures, these films exhibit antifouling properties, repelling oils containing proteins, etc. (Fig. 2).

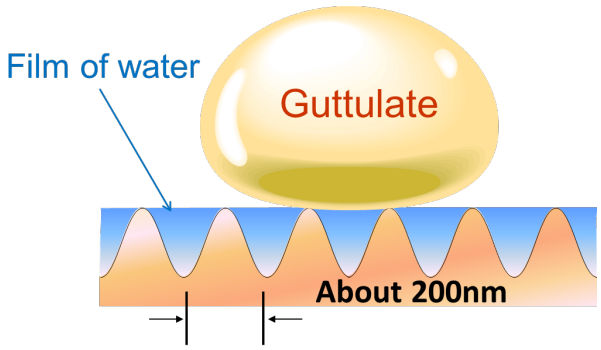

Fig. 2. Mechanism of the production of antifouling properties by superhydrophilic nanostructures.

Thus, we might expect to produce antifouling properties (super-nanohydrophilic effects) by forming such convex-concave nanoscale structures replicating snail shells on polymer surfaces. An earlier report discussed our efforts to form nanostructures on the surface of an acrylic polymer substrate by nanoimprinting, after which the polymer sheet was rolled into a tube to produce prototypes of biliary stents with antifouling properties [4, 5]. However, this approach involved creating a nano-mold using electron beam lithography and forming nanostructures using a nanoimprinting method. Lithography requires special facilities and equipment and entails high costs. Additionally, current nanoimprinting and lithographic technologies are generally suitable only for flat substrates; they are not designed to create nanostructures directly on the inner walls of a tubular substrate. In the present study, we used the atmospheric pressure low-temperature plasma method [6, 7] to develop a technology for imparting enhanced antifouling performance to the surfaces of tubular materials, regardless of substrate shape.

2. Biliary Stents with Antifouling Properties

Figure 3 shows the relative positions of the liver, gall bladder, and bile duct. Bile is a fluid secreted by the liver that activates lipase, a digestive enzyme that facilitates the dissolution of oils in water and assists in the digestion and absorption of lipids. The main constituents of bile are bilirubin (an end product of red-blood cell breakdown), cholesterol, and bile acid [8]. Bile is temporarily stored in the gall bladder before being excreted to the duodenum. Biliary strictures attributable to bile duct cancer [9] or bile duct obstructions inhibit the flow of bile from the gall bladder to the duodenum, bile may flow back into the liver, resulting in icterus or, if left untreated, even fatal hepatic failure. Treatment to secure a passage for bile flow often involves a surgical procedure called endoscopic biliary stenting (EBS) [10, 11].

Two types of biliary stents are currently available: metallic stents and plastic stents [11]. Most EBS procedures involve plastic stents. Figure 4 is a photograph of a straight plastic stent. Each end has a flap, and each section of the tube beneath the flap has an opening.

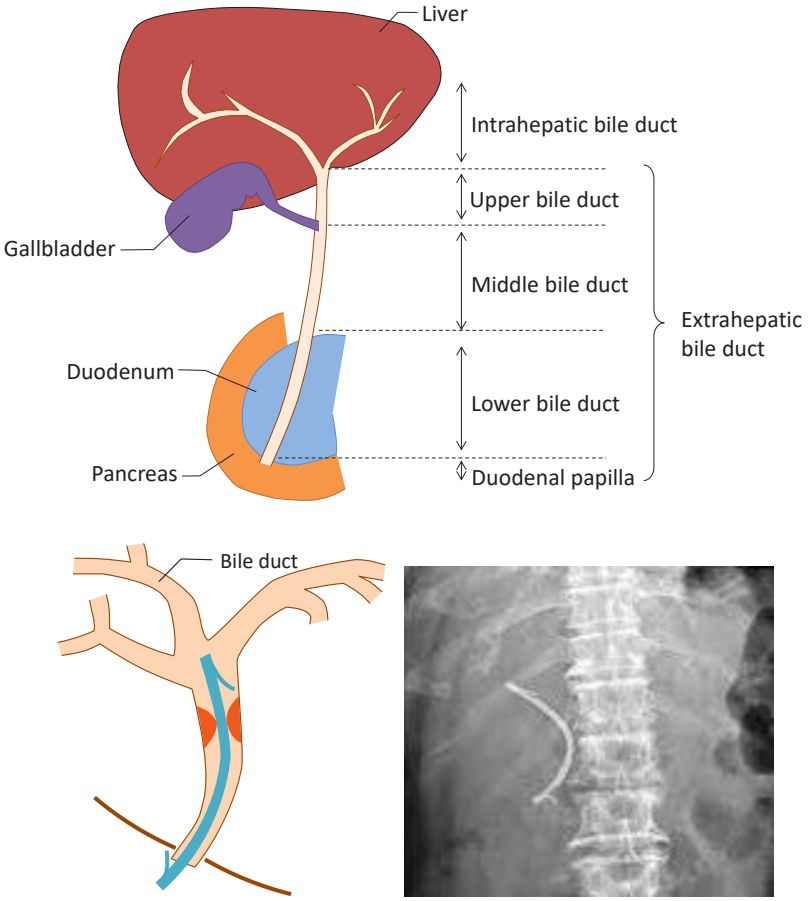

Fig. 3. Biliary tract structure and example of endoscopic biliary stenting procedure.

Fig. 4. Plastic stent (straight type, Boston Scientific Corporation).

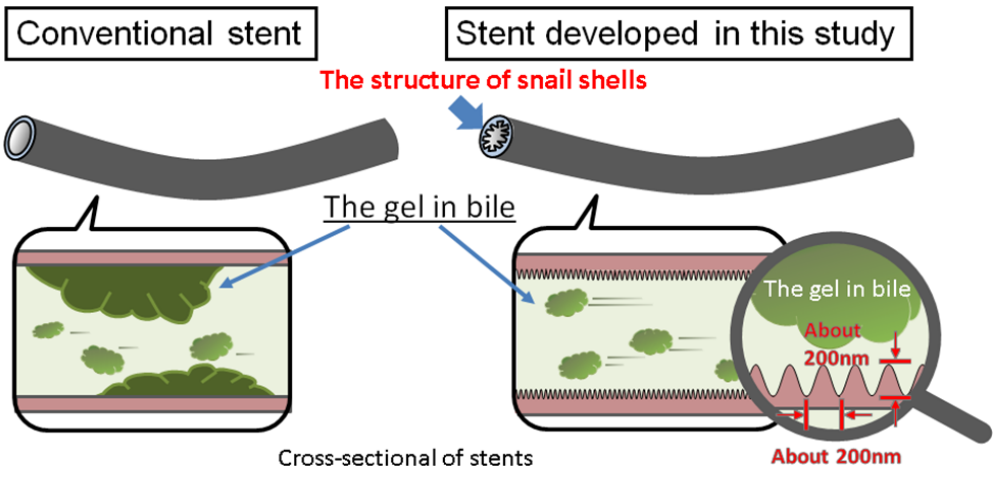

Fig. 5. Comparison of conventional stent and antifouling stent (schematic image).

Figure 5 is a schematic image comparing an antifouling stent to a conventional stent. In efforts to produce a surface that repels fluids containing oils, such as bile, we believed the structures found on snail shells, which exhibit super-nanohydrophilic effects in the presence of water, appeared likely to prove effective in creating an occlusion-resistant biliary stent.

We sought to develop elemental technologies for imparting antifouling properties to the inner walls of PE biliary stents by forming nanostructures directly onto the inner surface of polyethylene (PE) biliary stents with atmospheric pressure low-temperature plasma. We formed nanostructures on the inner walls of PE tubes of varying diameters under varying plasma conditions and examined the resulting structures and effects of the antifouling properties thus imparted.

3. Processing of Inner Walls of PE Tubes by the Atmospheric pressure low-temperature plasma Method

Atmospheric pressure low-temperature plasma can generally be categorized into two types: thermal equilibrium plasma (hot plasma) and nonequilibrium plasma (cold plasma) [12, 13]. A representative example of the former is arc discharge, in which the plasma is at high temperature, with both electron temperature and gas temperature on the order of 10,000 K. The latter is represented by glow discharge. Although the electron temperature of the plasma is 10,000 K or more, the gas temperature is around room temperature. Given the high gas pressure (the high number of molecules in the gas state) at atmospheric pressure, the number of collisions between electrons and gas molecules is also high, tending to result in plasma in a state of thermal equilibrium. While PE biliary stents cannot be exposed to hot thermal plasma, we believe cold plasma that can be sustained near room temperature is suitable.

Two well-known examples of atmospheric pressure low-temperature plasma are streamer discharge and dielectric barrier discharge. Since a uniform spatial distribution of discharge inside the biliary stent is required, we chose to use an RF power supply as the power source and helium as the dielectric barrier discharge gas. This combination suppresses electron density and is sufficient to form atmospheric pressure plasma of uniform distribution at low temperatures [12]. The diagram in Figure 6 illustrates the principle of this apparatus. The basic components are the power source, electrodes, and a glass tube through which helium gas flows. Two electrodes are placed on the opposite sides of the glass tube facing each other at some distance from the glass tube. High-frequency power is applied to the electrodes to generate atmospheric pressure low-temperature plasma inside the glass tube. As shown in Figure

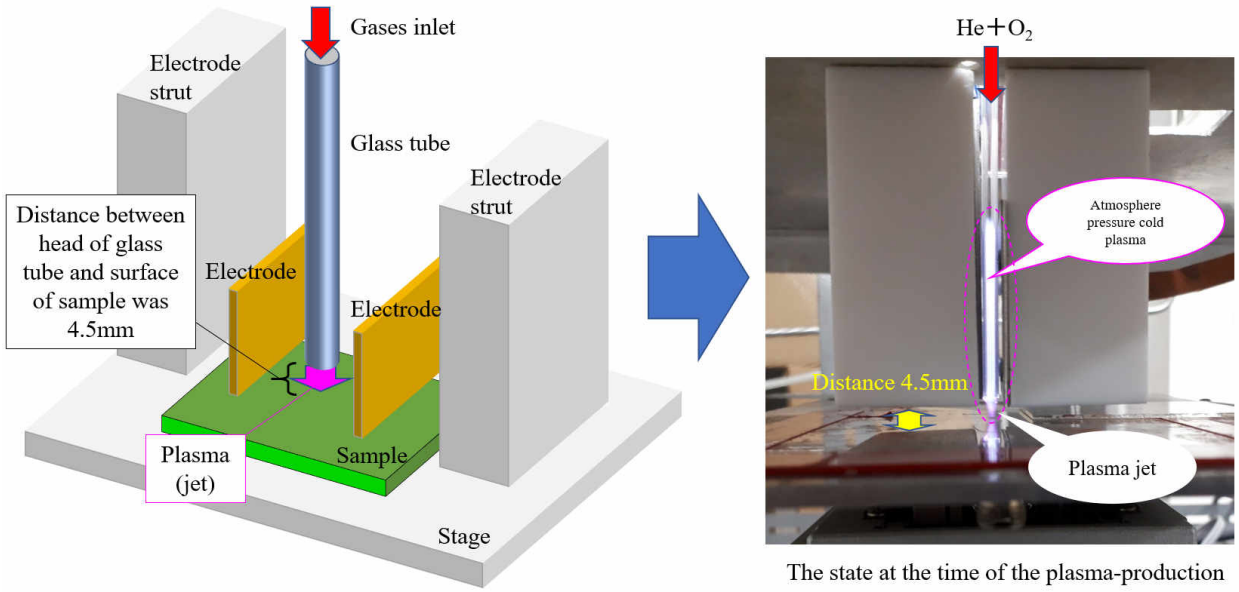

Fig. 6. Overview of the atmosphericc pressure low-temperature plasma generation unit and plasma being generated.

7, a PE tube is set in place of the glass tube. Plasma is generated inside the PE tube to form nanostructures directly onto the inner wall of the biliary stent.

When small amounts of oxygen are mixed into the He plasma, the dissociation of oxygen molecules generates atomic oxygen. Since the excitation level of atomic oxygen is the same as the metastable level of helium, previous studies suggest the Penning ionization reaction shown in the reaction formula below will occur. The oxidation reaction attributable to the atomic oxygen generated (O*) holds the promise of various applications for material surface processing technologies [13-20]. Mixing N_2 or NH_3 at concentrations of around 1 % in place of oxygen generates N radical (N*), amino radical (NH_2*), or imino radical (NH*), which can then be used to induce nitridation or amination of material surfaces [14, 15].

$$\mathrm{He} + \mathrm{electron} \rightarrow \mathrm{He}^* + \mathrm{electron} \quad (1)$$

$$\mathrm{He}^* + \mathrm{O}_2 \rightarrow \mathrm{He} + \mathrm{O}^* + \mathrm{O}^+ + \mathrm{electron} \quad (2)$$

4. Experimental

4.1. Examining plasma generation conditions

We observed the state of plasma generation inside the tube for varied He and O_2 flow rates (Figure 8). The results showed a stable glow discharge can be formed at an He flow rate of 1.4 slm and O_2 flow rate of 2–10 sccm. We then adjusted the power to determine the conditions at which stable plasma can be achieved.

Figure 9 shows the dependency of glow discharge inception power on O_2 flow rate. The He flow rate was fixed at 1.4 slm. We found that at O_2 flow rates of 0–6 sccm, a glow discharge can be stably formed at a power of 20–100 W. This power range may be regarded as the process window for glow

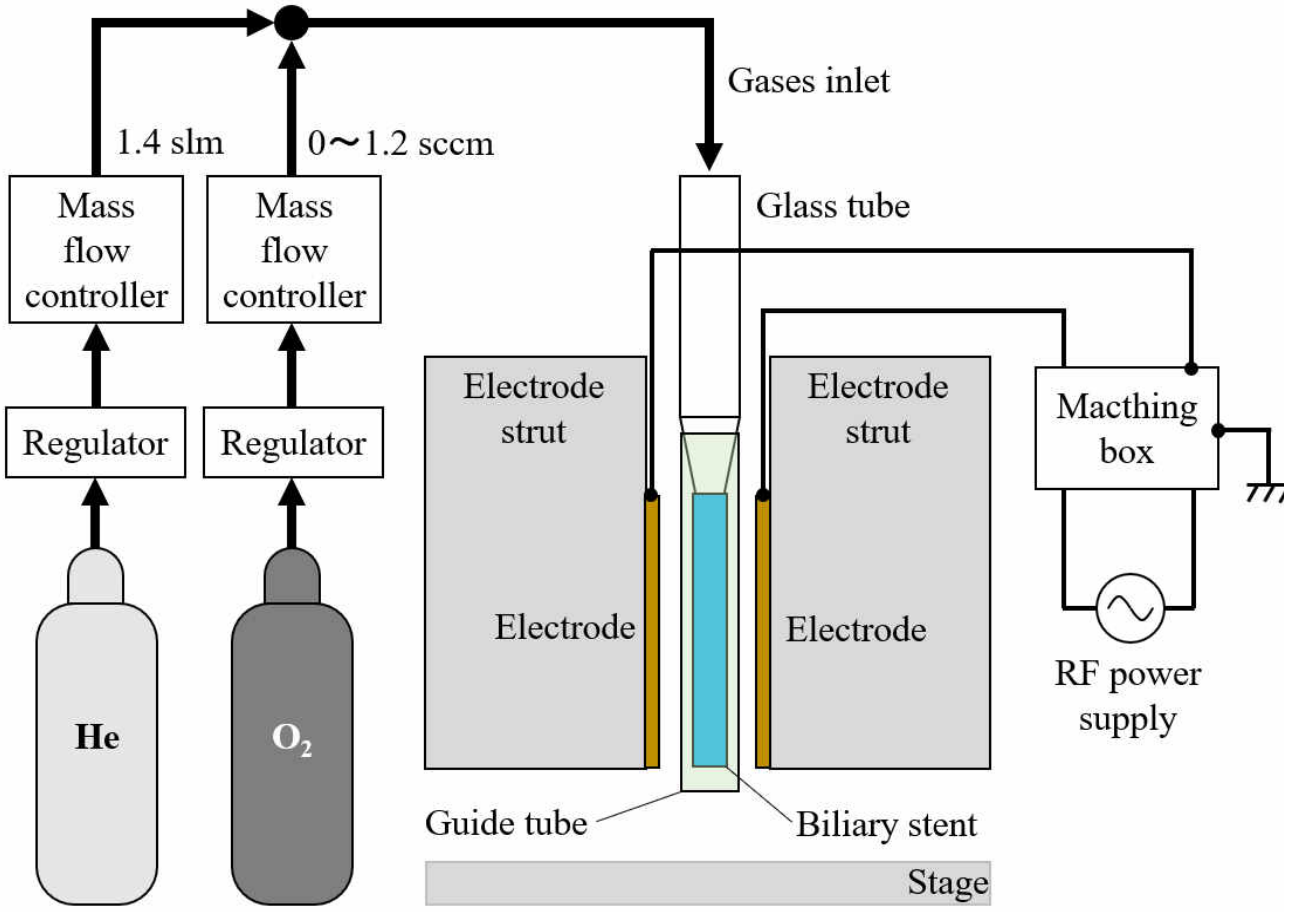

Fig. 7. Biliary stent plasma processing unit.

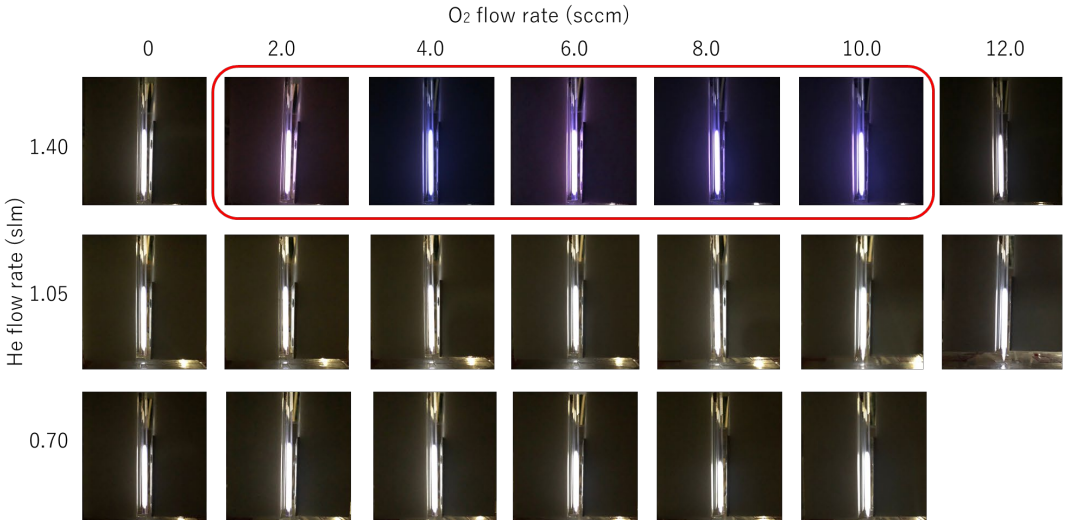

Fig. 8. State of plasma generation at various He and O_2 flow rates.

discharge inception. We surmised that stably forming a plasma inside the stent within this process window would allow processing of nanoporous structures on the inner wall of the stent.

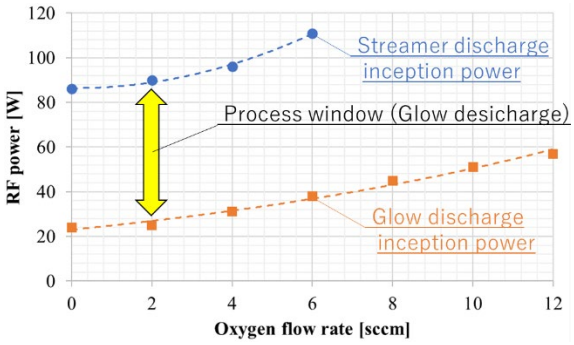

Fig. 9. Dependency of glow discharge inception power on O_2 flow rate (process window) at a fixed He flow rate of 1.4 slm.

Figure 10 shows photographs of the state of plasma formation within PE tubes of varying inner diameters. We achieved stable plasma formation with inner diameters of 2–4 mm.

4.2. Observations of plasma processed surfaces

To observe nanostructures on the inner walls of the PE tube, we rolled a piece of PE sheet into a tube and inserted it into a guide tube to simulate a PE biliary stent with an inner diameter of 2 mm, then exposed it to plasma processing. We observed the structures on the inner wall of the PE sheet via AFM (Figs. 11 and 12). We made observations for power settings of 45 W and 60 W. To prevent tube overheating due to plasma exposure, we limited the duration of a single plasma irradiation to 5 seconds and allowed cooling intervals of 30 seconds before subsequent irradiation. This irradiation cycle was repeated multiple times.

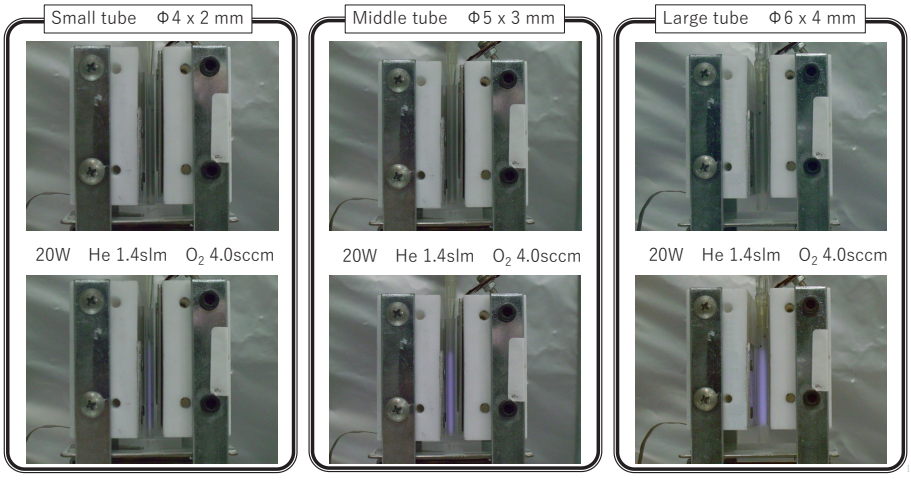

Fig. 10. State of plasma generation for different PE tube sizes.

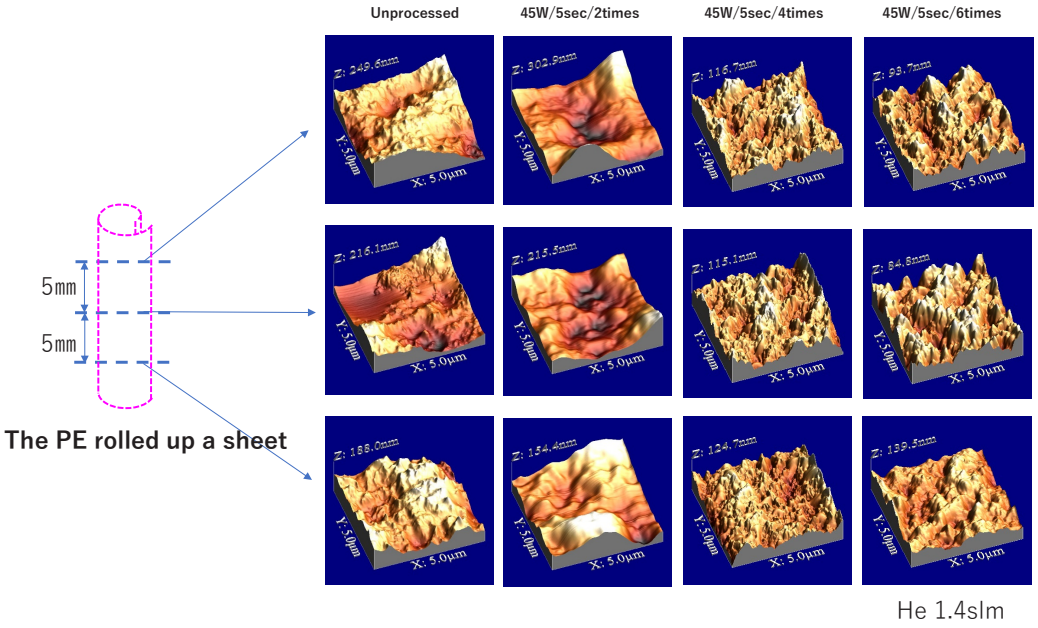

Fig. 11. Relationship between irradiation time and surface structures at 45 W and He flow rate of 1.4 slm.

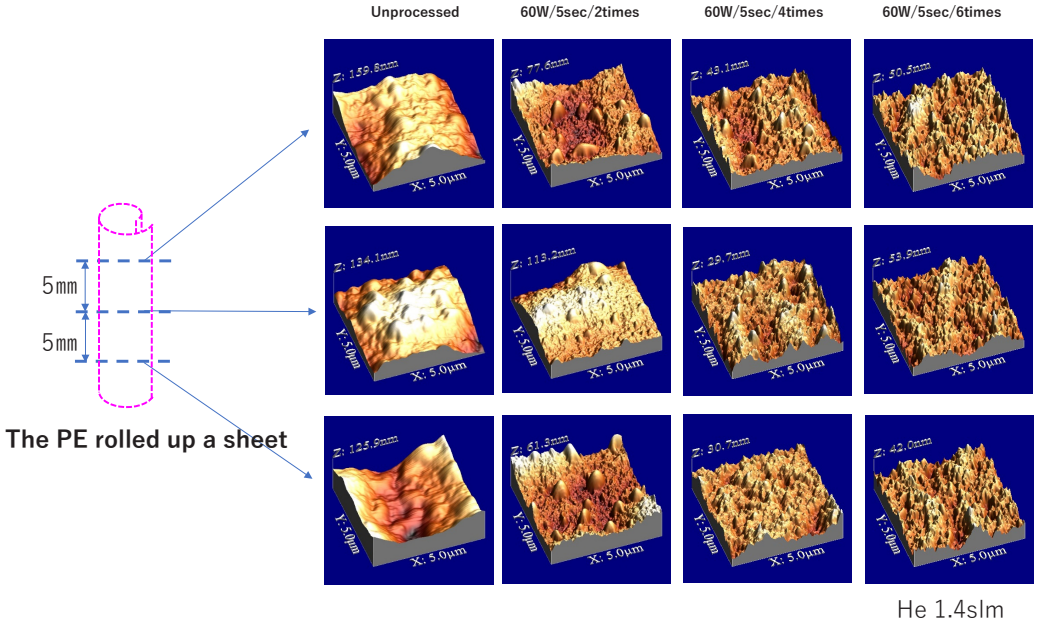

Fig. 12. Relationship between irradiation time and surface structures at 60 W and He flow rate of 1.4 slm.

Figure 11 shows the results of examination for irradiation at 45 W. Two irradiation cycles reduced surface roughness. Four to six irradiation cycles resulted in surfaces with satisfactory convex-concave nanoscale structures.

Figure 12 presents the results of examination for irradiation at 60 W. As with a power of 45 W, the nanostructures achieved after two irradiation cycles were insufficient. However, we could confirm that four to six irradiation cycles created surfaces with satisfactory convex-concave nanoscale structures.

These results indicated it was possible to form nanostructures on the inner wall of a stent by exposing it to plasma at a power of 45–60 W for four to six cycles for a duration of 5 seconds per cycle.

We examined the oil repellency of the inner wall of a PE tube of 2 mm in diameter processed with four cycles at an applied voltage of 45 W (Figure 13). According to the results, the contact angle was 107.7 degrees for unprocessed surfaces and

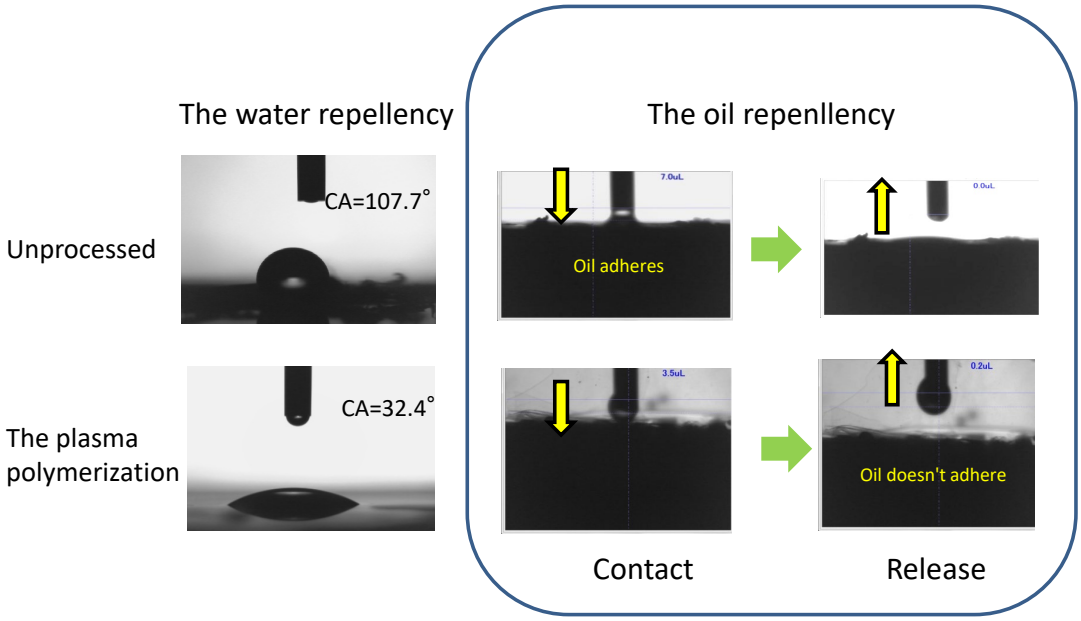

Fig. 13. Confirmation of water and oil repellency of inner stent walls.

32.4 degrees for plasma processed surfaces, which rendered them hydrophilic. We evaluated oil repellency in water and found that oil bound strongly to the unprocessed surfaces, while oil droplets failed to adhere to the plasma processed surfaces, confirming the oil repellent effects of the processed surfaces. We confirmed antifouling effects can be achieved through plasma processing.

4.3. Liquid passage test for PE stents

To evaluate the antifouling performance of PE tubes with nanostructures, we prepared an artificial bile solution from bovine bile powder and oil. The solution was prepared by dissolving a powder of bovine bile in pure water to achieve a concentration of 10 wt.%, adding lard to this solution at a concentration of 10 wt.%, and then heating to 40 °C. We used a pump to feed this artificial bile solution into PE tubes for observations of liquid passage. (Figure 14(a) is a photo of the apparatus used for the liquid passage test.) We allowed the bile solution to pass through the tube for 5 seconds at a flow rate of 6 mL/min, followed for 5 seconds by water. Then, once again, we passed the bile solution for 5 seconds, followed by water for 5 seconds. We observed the inner wall of the tube when water passed for the second time. For comparison, the photos show the tubes as the bile solution passes and as the water passes. We performed tests for tubes of three diameters: 2 mm, 3 mm, and 4 mm. The plasma processing conditions were four cycles of 10 seconds of irradiation and 10 cycles of 10 seconds of irradiation at 20 W and four cycles of 10 seconds of irradiation at 50 W. Under all processing conditions, we allowed a 30-second cooling interval after each 10-second plasma irradiation. Figure 14(b) presents the results of the liquid passage test.

The results confirmed that for unprocessed tubes of 2 or 3 mm in diameter, bile adhering to the inner wall of the tube was rinsed out with water. We observed no turbidity of the bile solution for surfaces processed by plasma for 10 cycles of 10 seconds of irradiation at 20 W and four cycles of 10 seconds of irradiation at 50 W; the surfaces were judged to have antifouling properties. For tubes of 4 mm in diameter, the amount of bile adhering to the inner wall was excessive, and the bile solution was confirmed to be turbid for all conditions.

5. Summary

We sought to develop elemental technologies for imparting antifouling properties to the inner walls of PE biliary stents by forming nanostructures directly onto the inner surface with atmospheric pressure low-temperature plasma. Nanostructures were formed on the inner walls of PE tubes having different diameters under varied plasma conditions, and the resulting structures and effects of the imparted antifouling properties were examined. The results show that plasma processing at an He flow rate of 1.4 slm, an O_2 flow rate of 0–6 sccm, and a power of 20–60 W forms satisfactory nanostructures on the inner walls of PE tubes that allow them to exhibit antifouling properties, especially oil repellency in water. In future studies, we plan to form nanostructures directly onto the

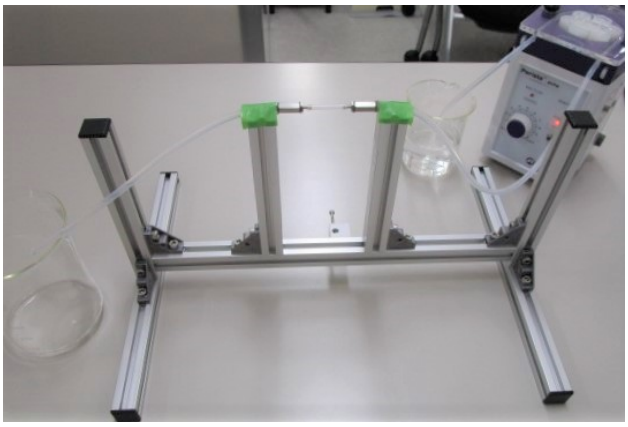

(a) External view of liquid passage test apparatus

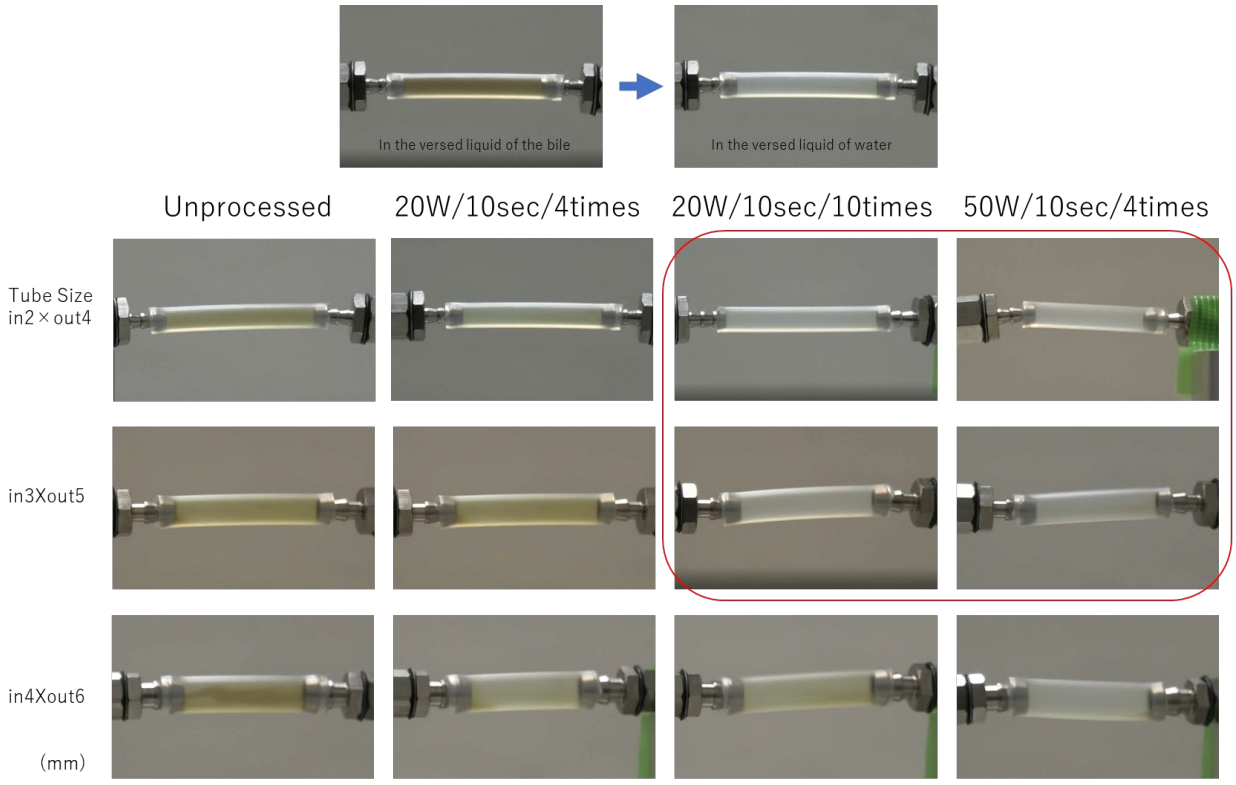

(b) Results of liquid passage test

Fig. 14. Apparatus and results of liquid passage test for mixed solution of bile + oil (lard).

inner surface of PE biliary stents with atmospheric pressure low-temperature plasma and confirm the imparted antifouling effects by performing animal experiments.

Acknowledgement

We wish to thank Mr. Hirano at HANACO Medical Corporation for supplying the PE biliary stents. This research was funded by 2018 revision manufacturing, commerce, service productivity improvement promotion subsidy.

References

1. M. Shimomura, "*Biomimetics, National Science Museum16*", *Tokai University Press*, **2** (2016).
2. J. Knippers, K. G. Nickel, and T. Speck, "*Biomimetic Research for architecture and Building Construction, Biological Design and Integrative Structures, Biologically Inspired System Vol.9*", Springer, (2016) 69.
3. M. Kato, *J. Print. Sci. Technol.*, **48** (2011) 186.
4. A. Sekiguchi, Y. Matsumoto, H. Minami, T. Nishino, H. Tanigawa, K. Tokumaru, and F.

Tsumori, *J. Pohotopolym. Sci. Technol.*, **31** (2018) 121.
5. A. Sekiguchi, T. Nishino, M. Aikawa, Y. Matsumoto, H. Minami, K. Tokumaru, F. Tsumori, and H. Tanigawa, *J. Pohotopolym. Sci. Technol.*, **32** (2019) 373.
6. C. Tendero, C. Tixier, P. Tristant, J. desmaison, and P. Leprince, *Specctrochemica Acta*, **B61** (2006) 2.
7. C. Jen-shin, *J. Plasma Fusion Res.*, **82** (2006) 682.
8. G. Masselli, R. Manfredi, A. Vecchioli, and G. Gualdi, *Eur. Radiol.*, **18** (2008) 2213.
9. T. Tsuyuguchi, T. Takada, Y. Kawarada, Y. Nimura, K. Wada, M. Nagino, T. Mayumi, M. Yoshida, F. Miura, A. Tanaka, Y. Yamashita, M. Hirota, K. Hirata, H. Yasuda, Y. Kimura, S. Strasberg, H. Pitt, M. W. Büchler, H. Neuhaus, J. Belghiti, E. Santibanes, S-T. Fan, K-H. Liau, and V. Sachakul, *J. Hepatobiliary Pancreat Surg.*, **14** (2007) 35.
10. http://www.shimadahp.jp/section.php?x-vew=4&from=section&navi=3&sin=6. By Shimada hospital HP.
11. A. C. Smith, J. F. Dowsett, R. C. Rassell, A. R. Hartfield, and P. B. Cotton, *Lancet*, **344** (1994) 1655.
12. S. Kanazawa, M. Kogoma, T. Moriwaki, and S. Okazaki, *J. Phys. D: Appl. Phys.*, **21** (1988) 838.
13. T. Murakami, *J. Plasma Fusion Res.*, **92** (2016) 688.
14. M. Kogoma, *Faculty of science and Techno.*, **58** (2007) 779.
15. M. Kogoma, *J. Vac. Soc. Jpn.*, **51** (2008) 2.
16. T. Tsunoda, *Jitsumu Hyomen Gijutsu*, **34** (1987) 415.
17. T. Matsuoka, K. Sakaguchi, and C. Hata, *J. Soc. Mat. Sci., Jpn*, **51** (2002) 1038.
18. T. Ohiwa, K. Sumiya, S. Ogawa, and K. Takiguchi, *Vaccum*, (1981) 214.
19. G. W. Collins, S. A. Letts, E. M. Fearon, R. L. McEachern, and T. P. Bernat, *Phys. Rev. Lett.*, **73** (1994) 708.
20. U. Cvelbar, S. Pejovnik, M. Mozetie, and A. Zalar, *Applied Surface Science*, **210** (2003) 255.

Journal of Photopolymer Science and Technology
Volume 34, Number 4 (2021) 411−415 ©2021SPST

Finite Element Analysis of Advanced Imprint Process to Multilayered Material

Kazuki Tokumaru[1], Tsuyoshi Miyata[2], and Fujio Tsumori[1*]

[1] *Department of Aeronautics and Astronautics, Kyushu University, 744 Motooka, Nishi-ku, Fukuoka 819-0395, Japan*
[2] *Department of Mechanical Engineering, Kyushu University, 744 Motooka, Nishi-ku, Fukuoka 819-0395, Japan*
**tsumori@aero.kyushu-u.ac.jp*

Biomimetic functional surfaces have been attracted industrial fields. The surface of a lotus leaf is a popular example of this bio-mimic surface which realize super-hydrophobicity. The key of this functional surface is a nano-patterned surface. Especially, double-roughness structure, which means rough and fine patterns on the same surface, is important. To fabricate biomimetic surfaces, nano imprint lithography (NIL) is an effective tool. NIL a low-cost lithographic method with simple thermal pressing process. Conventional NIL can form precise structures with high-resolution. We have proposed and developed some new fabrication methods based on NIL; multilayer imprinting (MLI) and in-plain compression imprinting (IPI). MLI starts with a multilayered sheet material for imprinting and results a more complex structure on the interface of the layers. IPI adds in-plane compression to NIL process to obtain structures with higher aspect ratio. There is difference between conventional NIL and these new processes. For the conventional NIL, obtained surface pattern is determined by the mold pattern. On the other hand, we could not know the interface pattern obtained by MLI or the pattern after IPI. We employed finite element analysis in this work. We used the generalized Maxwell model for the finite element analysis of our newly developed NIL. The simulation system could be a design tool for our new processes.
Keywords: Multilayer Imprinting, In-plain compression imprinting, Finite element analysis, Biomimetic

1. Introduction

Nano imprint lithography (NIL) is a promising process to realize biomimetic surface. NIL has some advantages such as a high-throughput and low-cost processes, which is suitable especially for fabricating biomimetic surfaces [1,2]. Conventional NIL can only fabricate simple structures [3,4]. Recently, authors developed some new fabrication methods based on NIL to fabricate more complex structures. Our newly proposed processing methods are named multi-layer imprinting (MLI) [5-16] and in-plain compression imprinting (IPI) [17-19].

Figure 1 shows the processing flow of MLI. The flow is same as the thermal NIL except using a multi-layered sheet as a work material. Fine patterns are transferred by pressing the mold against the heated multilayer material. By simultaneously deforming not only the surface of the multilayer material but also the interface of the layers during pressing, the interface pattern can be produced.

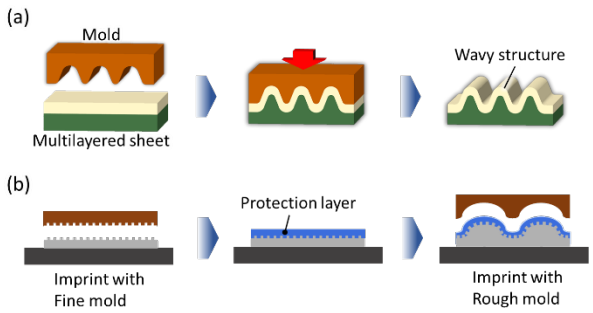

Fig. 1. Schematic illustration of multilayer imprinting process (a), and with micro-patterning for hierarchical pattern (b).

Received April 5, 2021
Accepted April 22, 2021

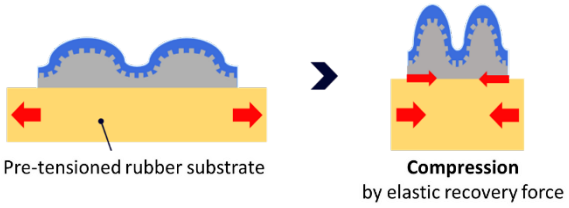

Fig. 2. Schematic illustration of in-plain compression imprinting (IPI).

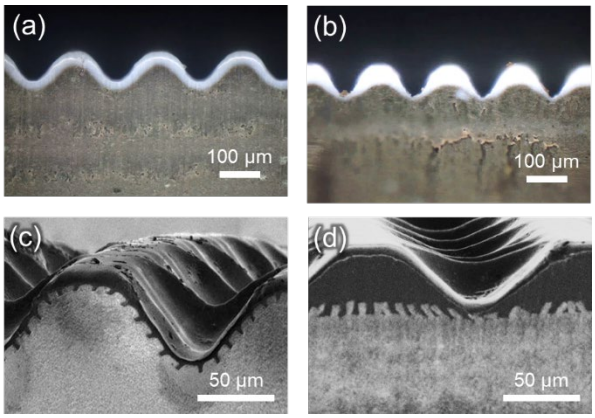

Fig. 3. Difference in interface shape due to processing conditions. Cross-sectional patterns of simple MLI process, (a) and (b), and with micro-patterning (c) and (d).

More complicated patterns that were difficult to form by the conventional NIL have been successfully formed by MLI.

Our second process is IPI. Figure 2 shows the processing flow of IPI. IPI adds in-plane compression to the MLI process to realize more complex structures by using not only vertical but also horizontal deformation. We use elastic recovery force of the rubber substrate as the in-plane compression. This process makes it possible to fabricate protruding structures that grow horizontally.

There is an issue of MLI and IPI; that is controlling the interface shape. The mold pattern is transcribed similarly to the material, on the other hand, the interface shape would depend on physical properties of each layer. Also, the pressing conditions can affect the interface shape. Figure 3 shows examples of the difference in interface shape due to processing conditions. Figures 3 (a) and (b) show deformation patterns of samples by MLI, which corresponds a process shown in Fig. 1 (a). Figures 3 (c) and (d) show results of MLI, which is shown in Fig. 1 (b). In our previous studies, we repeated trial to obtain the target interface shape, however it was not clever, and a more efficient designing system would be needed.

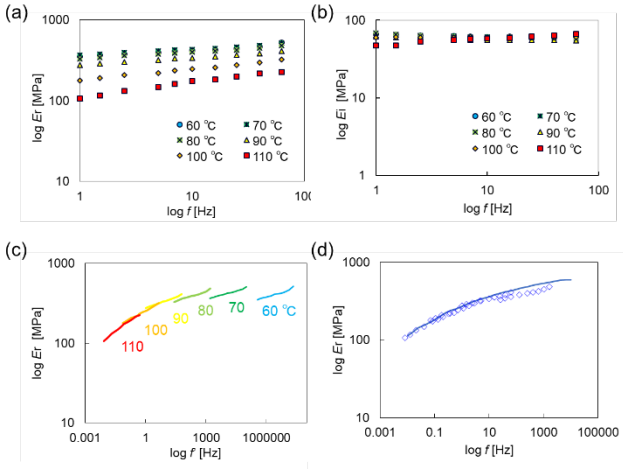

Fig. 4. Conditions of FE-analysis. (a) Elastic component of material, and (b) viscous component. (c) WLF shifted elastic component, and (d) obtained master curve.

In order to overcome this issue, we have tried a computational approach with a simple model [20]. In this paper, we carried out a processing simulation of MLI using finite element analysis. We performed 2D analysis adopted with a generalized Maxwell model. A commercial FEA software, ANSYS, was used for this simulation.

2. Analysis for MLI

Finite element analysis has been sometimes used for conventional FEA. In these cases, the hyper elastic model was often used. The hyper elastic model is known as an effective model for a single material.

In MLI, multilayer materials are used. There is difference in elastic modulus between the layers, which affects significantly on the interface shape. Here, we should consider viscoelasticity. In the previous experimental studies, we employed layered compound sheets with a mixture of ceramic powder and a polyvinyl alcohol-based binder. We took material properties of the same materials for the present simulation. Due to the viscoelasticity of the materials, response of each layer depends on the processing speed. Therefore, it is essential to use a viscoelastic model for finite element analysis of MLI. In this study, we used a generalized Maxwell model.

Viscoelastic properties of the compound sheets were determined by a uniaxial viscoelastic test. Figures 4 (a) and (b) show elastic and viscous components, respectively. The viscoelastic characteristics were measured in the temperature range of 60 to 110 °C with the frequency set to 1 to 63 Hz. A master curve could be obtained using WLF

Table 1. Constants of the generalized Maxwell model for the master curve shown in Fig. 4 (d).

n	α	G(MPa)	τ
∞	0.01	3	-
1	0.33	99	1000
2	0.33	99	100
3	0.33	99	10

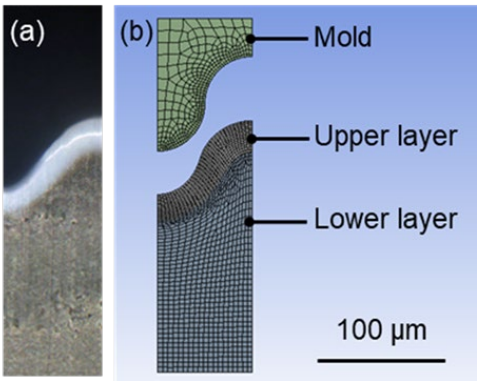

Fig. 5. Cross-sectional image of experimental data (a) and that obtained from the simulation (b).

formula from these results. The time-temperature conversion rule can be applied to the viscoelastic material. By creating a master curve, a wide range of frequency characteristics could be implemented in the simulation. Figure 4 (c) shows WLF shifted elastic component of lower compound sheet, and Fig. 4 (d) shows a master curve obtained by fitting. For the viscoelastic model, a generalized Maxwell model with four elements in parallel was used. The parameters for the generalized Maxwell model are shown in Table 1.

Figure 5 shows the cross-sectional shapes obtained from the experiment (a) and simulation (b). The simulated result using the generalized Maxwell model showed a good agreement with the experimental data. It would be useful to obtain the optimal imprinting conditions in virtual before performing the real process. It is found that the difference in elastic modulus changed the interface shape by finite element analysis.

Next, we show an example using some virtual materials. Three materials M1, M2, and M3 with different viscoelastic moduli shown in Table 2 were used. Figure 6 (a) shows the relaxation modulus of each material. In this model, as in the model shown in Fig. 4, a generalized Maxwell model with four parallel elements was used, and the relaxation times

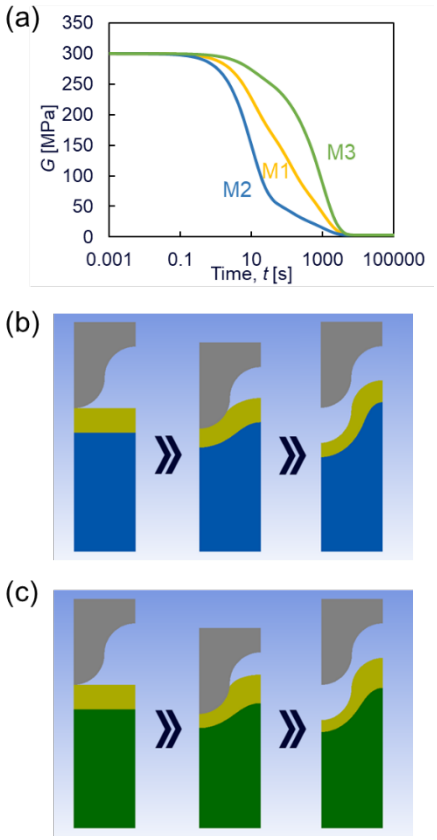

Fig. 6. Time dependence of relaxation modulus of each material (a), and snapshots of FE analysis using M1 as upper material. M2 was used as lower material (b) and M3 as lower material (c), respectively.

Table 2. Constants of the generalized Maxwell model for analysis shown in Fig. 6.

		τ_1	τ_2	τ_3
		1000	100	10
	G_∞ (MPa)	G_1	G_2	G_3
M1	3	99	99	99
M2	3	33	33	221
M3	3	221	33	33

τ for each of the three viscous elements were τ_1 = 1000, τ_2 = 100, and τ_3 = 10. The viscoelastic behavior of a material was determined by the elastic components of the three viscoelastic elements.

The simulated geometry changes are shown in Figs. 6(b) and 6(c). In both cases, material M1 was used as the upper layer material, while material M2 and M3 were used as the lower layer material in Fig. 6(b) and Fig. 6(c), respectively. These results show that the viscoelastic property resulted difference thickness distribution in the upper layer. This result

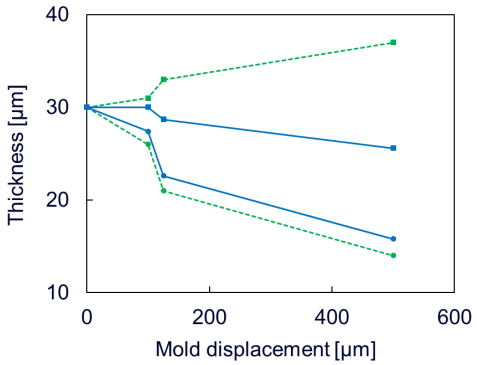

Fig. 7. Relationships between mold displacement and thickness of upper layer at the peak and valley points.

was caused by the dynamic modulus of the material M1 was larger than that of M2, and smaller than that of M3.

Figure 7 shows relationships between the mold displacement and the thickness of upper layer at the peak and the valley points of upper layer in each case. At the valley point, the thickness of the upper layer decreased with pressing distance in both cases. On the other hand, upper layer shows different deformations at the peak point. In case of M2, the thickness of the mountains decreased as that of the valleys, but in case of M3, the thickness at the peak increased. The elastic modulus of the lower layer was larger than that of the upper layer in the case of M3, the pressure applied to the upper layer was larger, and the material around the valley point flowed up toward the peak points, and this flow increased the thickness of the mountains. In case of M2, higher elastic modulus of the upper layer than that of the lower layer caused easier deformation of the lower layer so that the horizontal flow of the upper layer was suppressed, resulting in a decrease in thickness at all points.

Thus, different distribution of upper-layer thickness, or the shape of the interface, was obtained by changing the materials of the upper layer. The thickness at the peak and the valley points could be controlled by selecting proper elastic modulus.

3. Analysis for IPI

Similar analysis as described in the previous section for MLI could be used also for IPI. The in-plane compaction of multilayered compound sheets was performed in a previous study. In this experimental study, the aspect ratio of wavy shape of the layer interface increased by 15 times at a compression rate of 50 %. We tried FE-analysis of IPI using the same condition with this experiment.

Figure 8 shows the result. The experimental data and the FEA results are shown in left and right,

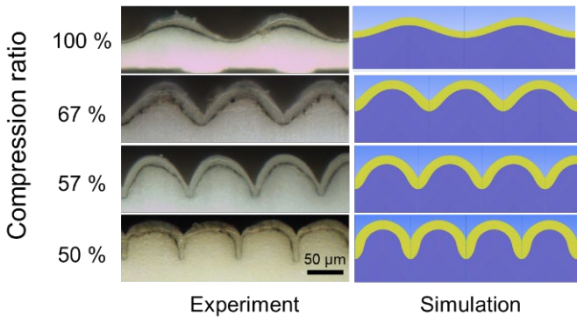

Fig. 8. Cross-sectional view of IPI sample (left) and result obtained by FE analysis (right).

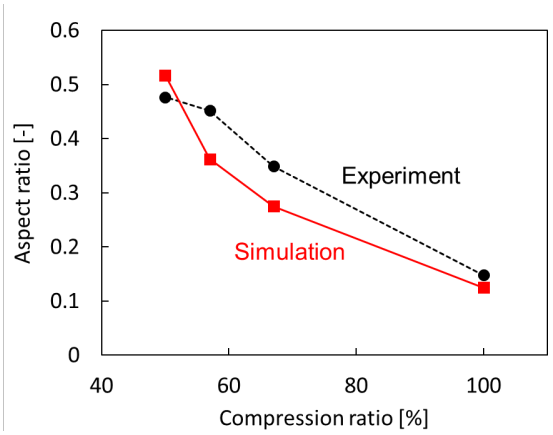

Fig. 9. Relationship between in-plain compression ratio and aspect ratio of the interface.

respectively, and they look similar. Figure 9 shows the aspect ratio of the interface at different compression ratios. The both results show the same trend. The aspect ratio of the interface increasing as the compression.

We also simulated IPI with micro-patterning on the interface. Figure 10 shows the result. By multilayer imprinting, we fabricate a molded body with a rough pattern on the surface and a finer pattern at the interface. By applying in-plane compression to it, the interface is bent along the surface pattern. As shown in Fig. 10, the simulated pattern shows a good agreement with the experimental pattern.

There has been an issue to form a hierarchical pattern with high aspect ratio [21, 22]. We have not successfully carried out IPI if higher compression ratio was needed. However, we can try the process in a virtual case. Figure 11 shows the result with larger compression ratio. We can expect the state after large compression.

4. Conclusion

Finite element analysis was performed for newly developed nanoimprint processes using the generalized Maxwell model. Simulations on

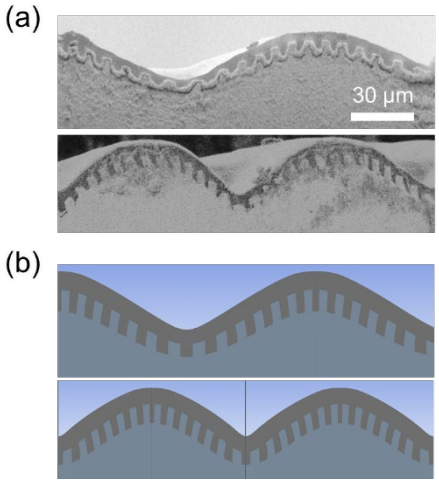

Fig. 10. Relationship between in-plain compression ratio and aspect ratio of the interface.

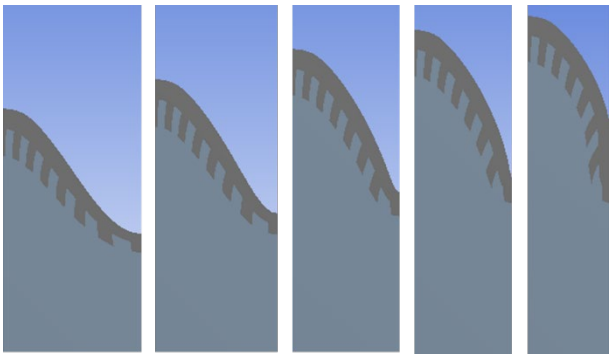

Fig. 11. Simulated results with larger in-plain compression ratio which has been difficult to achieve in experimental work.

multilayer imprinting (MLI) and in-plain compression imprinting (IPI) were carried out, and the simulated data were compared to experimental results. The obtained deformation showed a good agreement with the experimental results. This FEM simulation would be a powerful tool to design variable patterns on the surface and the interface. The designing of the interface would be also useful for microchannel formation process [23-25].

References

1. A. Sekiguchi, Y. Matsumoto, H. Minami, T. Nishino, H. Tanigawa, K. Tokumaru, and F. Tsumori, *J. Photopolymer. Sci. Tech.*, **31** (2018) 121.
2. A. Sekiguchi, T. Nishino, M. Aikawa, Y. Matsumoto, H. Minami, K. Tokumaru, F. Tsumori, and H. Tanigawa, *J. Photopolymer. Sci. Tech.*, **32** (2019) 315.S. Y. Chou, P. R. Krauss, and P. J. Renstrom, *Appl. Phys. Lett.*, **67** (1995) 3114.
3. S. Y. Chou, P. R. Krauss, and P. J. Renstrom, *Science*, **272** (1996) 85.
4. S. Y. Chou, P. R. Krauss, and P. J. Renstrom, *J. Vac. Sci. Technol. B*, **14** (1996) 4129.
5. Y. Xu, F. Tsumori, H.G. Kang, and H. Miura, *J. Jpn. Soc. Powder Powder Metall.,* **58** (2011) 673.
6. Y. Xu, F. Tsumori, T. Toyooka, H. Kotera, and H. Miura, *Jpn. J. Appl. phys.,* **50** (2011) 06GK11.
7. X. Yang, F. Tsumori, H. G. Kang and M. Hideshi, *Adv. Sci. Lett.,* **12** (2012) 170.
8. F. Tsumori, S. Hashimoto, M. Takahashi, Y. Xu, H. Kang, O. Osada, and H. Miura, *Proc. Powder Metallurgy World Congress*, (2013) P-T6-72.
9. Y. Xu, F. Tsumori, S. Hashimoto, M. Takahashi, H. Kang, T. Osada, and H. Miura, *Proc. IEEE-NEMS*, (2013) 887.
10. Y. Xu, F. Tsumori, S. Hashimoto, M. Takahashi, H. Kang, T. Osada and H. Miura, *Micro Nano Lett.,* **8** (2013) 571.
11. F. Tsumori, X. Yang, Y. Tanaka, T. Osada and H. Miura, *Proc. Eng.,* **81** (2014) 1433.
12. F. Tsumori, Y. Tanaka, X. Yang, T. Osada and H. Miura. *Jpn. J. Appl. Phys.,* **53** (2014) 06JK02.
13. F. Tsumori, *J. Jpn. Soc. Technol. Plasticity*, **56** (2015) 265.
14. F. Tsumori, K. Tokumaru, K. Kudo, T. Osada, and H. Miura, *J. Jpn. Soc. Powder Powder Metall.,* **63** (2016) 519.
15. K. Tokumaru, F. Tsumori, K. Kudo, T. Osada and K. Shinagawa, *Jpn. J. Appl. Phys.,* **56** (2017) 06GL04.
16. K. Yonekura, K. Tokumaru and F. Tsumori, *Jpn. J. Appl. Phys.,* **57** (2018) 06HG05.
17. K. Tokumaru, K. Yonekura, and F. Tsumori, *J. Photopolymer Sci. Tech.*, **32** (2019), 315.
18. T. Miyata, K. Tokumaru, and F. Tsumori, *Jpn. J. Applied Phys.*, **59** (2020) sIIJ07.
19. T. Miyata, K. Tokumaru, and F. Tsumori, *J. Photopolymer Sci. Tech.*, **33** (2020) 199.
20. F. Tsumori, Y. Xu, H. Kang, T. Osada and H. Miura, *Proc. 12th Computational Plasticity,* (2013) 1267.
21. F. Tsumori, L. Shen, T. Osada, and H. Miura, *Manuf. Rev.,* **2** (2015) 10.
22. L. SHEN, F. Tsumori, X. Yang, T. Osada, H. Miura, *7th Asia Workshop Micro/Nano Forming Technol.,* (2014).
23. F. Tsumori, S. Hunt, T. Osada and H. Miura, *Jpn. J. Appl. Phys.,* **54** (2015) 06FM03.
24. F. Tsumori, S. Hunt, K. Kudo, T. Osada and H. Miura, *J. Jpn. Soc. Powder Powder Metall.,* **63** (2016) 511.
25. K. Tokumaru, S. Hunt, and F. Tsumori, *Proc. MicroTAS*, (2018) 522.

Communication

Journal of Photopolymer Science and Technology
Volume 34, Number 4 (2021) 417−421 ©2021SPST

Petal-like Microstructures Formed from Sterically Crowded Chromophores

Yoshiaki Tokumura[1] and Mina Han[1,2]*

[1] *Department of Chemistry and Biotechnology, Tottori University, 4-101 Koyama Minami, Tottori 680-8552, Japan*
[2] *Department of Chemistry Education, Kongju National University, 56 Gongjudaehak-ro, Gongju, Chungnam 32588, Korea*
**hanmin@kongju.ac.kr*

A sterically crowded triangular molecule (3PhA) was synthesized with three terminal triphenylamine (TPA) wings connected to the central ring structure via a diethylphenyl group. In contrast to the tendency of conventional triangular molecules to assemble into one-dimensional fibrous structures, the nonplanar distorted 3PhA formed micrometer-sized petal-like aggregates. When excited with ultraviolet (UV, 340-360 nm) and green (510 nm) light, 3PhA in organic solutions exhibited two fluorescence bands maximized at ~380-400 and ≥650 nm, respectively. The fluorescence properties did not change significantly even after the formation of flat petal-like structures. These experimental results are likely due to the distorted molecular structure of sterically crowded 3PhA, which can cause suppression of intramolecular rotation and weakening of intermolecular interactions.

Keywords: Fluorescence, petal-like structure, self-assembly, sterically crowded chromophore

1. Introduction

Fluorescent organic materials have attracted much attention because of their intriguing functions and potential applications in sensors, switches, and optical information storage [1-8]. Self-assembled structures have a variety of unexpected functions that are different from component molecules. Because external stimuli such as light, pressure, and heat may induce changes in intermolecular interactions, spatial arrangements and morphology, and/or conformational changes in the individual component molecules, such nano/microstructured materials serve a variety of functions. Many studies have reported on fluorescent materials with different shapes, sizes and functions [2-14]. Nevertheless, it is still challenging to understand the rational molecular design of component molecules and to investigate the absorption and fluorescence properties of their assembled structures.

Azobenzene is a representative photochromic compound, but is generally known to not fluoresce at ambient temperature [15-18]. This is because the energy in the excited state is highly consumed through non-radiative conformational changes, thus causing a significant reduction in the fluorescence intensity. To address this issue and to obtain fluorescent azo-containing chromophore, we designed sterically crowded 2,4,6-tris{(*E*)-(4'-(diphenylamino)-3,5-diethyl-[1,1'-biphenyl]-4-yl)diazenyl}benzene-1,3,5-triol (3PhA, Scheme 1) which has an azo-containing aromatic core and three nonplanar triphenylamine (TPA) wings [19-20]. Such *o*-hydroxy compounds can show fluorescence due to the presence of the tautomeric hydrazone form [21-25]. Due to the steric effect and substantial distortion of 3PhA chromophore, we expected that intramolecular rotation and intermolecular interactions would be considerably limited in an aggregated state. Absorption and fluorescence characteristics in organic solutions as well as in assembled states were investigated.

2. Experimental

2.1. Synthesis

Received April 1, 2021
Accepted April 30, 2021

2,4,6-tris{(*E*)-(4'-(diphenylamino)-3,5-diethyl-[1,1'-biphenyl]-4-yl)diazenyl}benzene-1,3,5-triol (3PhA)

3PhA was synthesized from the Suzuki-Miyaura coupling reaction of the 2,4,6-tris{(E)-(4-bromo-2,6-diethylphenyl)diazenyl}benzene-1,3,5-triol (1) in the presence of tetrakis(triphenylphosphine)-palladium(0) [$Pd(PPh_3)_4$] catalyst [24,25]. In a 200 mL three-neck round-bottom flask, the precursor (1, 0.50 g, 0.59 mmol) and a catalytic amount of $Pd(PPh_3)_4$, 4-(diphenylamino)phenylboronic Acid (Tokyo Chemical Industry Co., LTD, 0.69 g, 2.38 mmol) were dissolved in toluene (20 mL) under nitrogen atmosphere. A water solution of $NaHCO_3$ (1N, 60 mL) were added to the reaction mixture. The reaction mixture was stirred vigorously under refluxing condition for 18 hours. After cooling the mixture to room temperature, water and chloroform were added and stirred at room temperature for 30 minutes. The organic portion was washed several times with water and then dried over anhydrous $MgSO_4$. The crude compound was purified by repeated column chromatography (chloroform:n-hexane = 3:1, v/v) and recrystallization to obtain dark purple solid (0.35 g, yield 45%).

^{1}H NMR (500 MHz, $CDCl_3$) δ 7.51 (d, 6H, aromatic, J = 8.59 Hz), 7.35 (s, 6H, aromatic), 7.29-7.26 (m, 18H, aromatic), 7.15 (d, 18H, J =7.45 Hz), 7.06 (t, 6H, aromatic, J = 7.45 Hz), 2.95 (q, 12H, $ArCH_2CH_3$, J = 7.45 Hz), 1.34 (t, 18H, $ArCH_2CH_3$). Anal. Calcd: C, 80.87%; H, 6.11%; N, 9.43%. Found C, 80.37%; H, 6.16%; N, 9.37%. HR-ESI-MS (m/z): Found, 1336.6510 (= M+H), Calcd for $C_{90}H_{82}N_9O_3$ = 1336.6541.

2.2. Materials and Characterization

Spectroscopic grade tetrahydrofuran (THF), *n*-hexane (hexane) dichloromethane (DCM), methanol (MeOH) and ethanol (EtOH), which were purchased from KANTO chemical Co., Inc., Japan, were used to dissolve 3PhA molecule. Ultrapure water (which was purified to reach a minimum resistivity of 18.0 MΩ·cm (25°C) using a μPure HIQ water purification system, Romax, South Korea) was used for all experiments. After a 20-sec nitrogen purge, a screw-cap quartz cuvette containing 3PhA solution was sealed with Parafilm. ^{1}H NMR, ultraviolet-visible (UV-vis) absorption and fluorescence spectra were obtained using a JEOL JNM-ECP500 (500 MHz), Shimadzu UV-2600 UV-vis spectrophotometer and a Horiba FluoroMax-4 spectrofluorometer, respectively.

X-ray diffraction (XRD) data were collected using a Rigaku MiniFlex 600 diffractometer with Cu radiation. Optical microscopy (OM) and fluorescence optical microscopy (FOM, λ_{ex} = 520–550 nm) images were obtained using an Olympus BX53 microscope after placing ~3 drops of the 3PhA sample onto a clean glass substrate. FE-SEM (field-emission scanning electron microscopy, TESKAN-MIRA3-LM) samples were coated with approximately 5-10 nm thick platinum layer using a Cressington 108 auto sputter coater, Ted Pella, Inc.

3. Results and discussion

Whereas many triangular molecules have a tendency to form long fibrous structures, 3PhA with three terminal TPA wings at the periphery tends to assemble into micrometer-sized flat petal-like

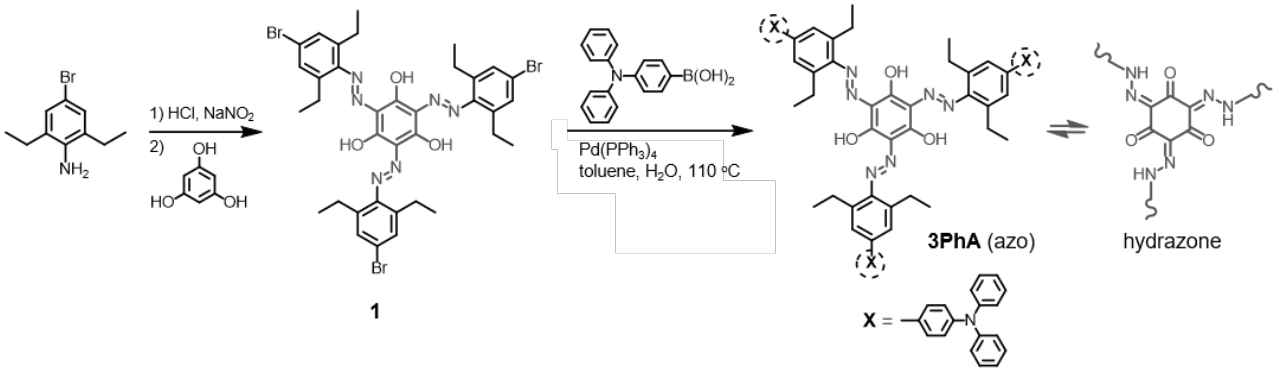

Scheme 1

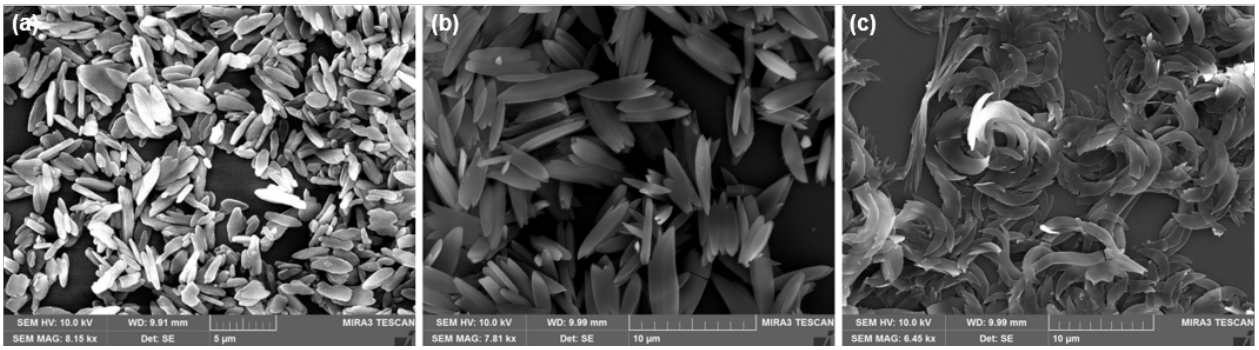

Fig. 1. SEM images of 3PhA petal-like aggregates obtained from (a) 4×10^{-5} M THF-hexane (1:1, v/v), (b) 4×10^{-5} M THF-MeOH (1:1, v/v), and (c) 4×10^{-5} M DCM-MeOH (1:1, v/v) mixed solutions.

structures. For instance, when hexane was added dropwise as a poor solvent to a 3PhA THF solution, the resulting well-dispersed suspension [4×10^{-5} M THF-hexane (1:1, v/v) mixture] contained flat petal-like aggregates with the length and width of 2-5 μm and 0.5-2 μm, respectively (Fig. 1a). If MeOH was added instead of hexane, thin petals less than ~8 μm long were frequently observed from a 4×10^{-5} M THF-MeOH (1:1, v/v) mixed suspension (Fig. 1b).

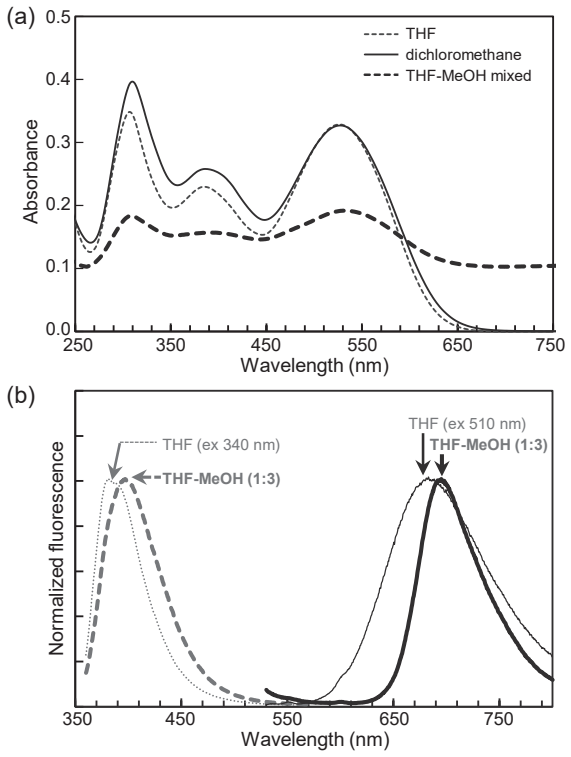

Fig. 2. (a) UV-vis absorption and (b) fluorescence spectral changes before and after the formation of petal-like aggregates.

By comparison, as MeOH (or EtOH as a poor solvent) was added to a 3PhA DCM solution, the mixed solution became opaque in the early stage, and then precipitation occurred slowly. Scanning electron microscopy (SEM) and optical microscopy (OM) images taken from such opaque samples display relatively larger, curved petal-like structures that are approximately 10 micrometers long (Fig. 1c). Such flat microstructures sometimes got tangled together to form more complex structures, as the assembly progressed sufficiently.

The self-assembly of 3PhA into flat petal-like structures instead of long fibrous structures appears to be associated with the highly distorted molecular structure containing three terminal TPAs and their stacking modes. We next employed absorption and fluorescence spectroscopic and XRD measurements to obtain such information.

Fig. 2a shows that 3PhA has three intense absorption bands at around 310, 390, and 530 nm. Considering that the short axis ϕ–ϕ^* transition [26] of conventional azobenzene unit emerges at approximately 250-270 nm, the strong absorption band appearing in the shortest wavelength region seems to arise from TPA being linked to the central ring structure via a phenyl ring. The absorption band at around 530 nm is likely due to the energetic proximity of the (π,π^*) and (n,π^*) states and intramolecular proton-transfer reactions (keto-

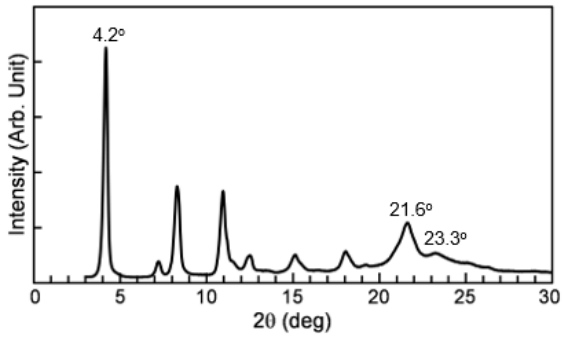

Fig. 3. X-ray diffraction pattern of 3PhA aggregates

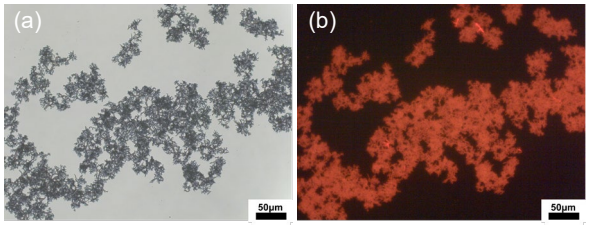

Fig. 5. (a) OM and corresponding (b) FOM images of 3PhA aggregates obtained from 6.7×10^{-5} M DCM-MeOH (1:2, v/v) mixed solution.

hydrazone form) [21-23].

Interestingly, the positions of the maximum absorption bands were not significantly affected by the solvents used in this study (THF and DCM) and aggregation (Fig. 2a). For example, as MeOH was added to 3PhA THF solution, self-assembly proceeded and the mixed solution became opaque. As a result, its turbidity (shown by the absorbance at >700 nm) increased prominently, but the obtained maximum absorption positions were hardly changed. In addition, the XRD pattern exhibited a strong peak at $2\theta = 4.2^{o}$ ($d = 21.0$ Å), which roughly corresponds to the molecular size. Two peaks appearing at $2\theta = 21.6^{o}$ and 23.3^{o} ($d = \sim4.1$ and 3.8 Å, respectively) are longer than frequently observed π-π stacking interaction distances [27,28]. These results can be interpreted as follows. The introduction of three propeller-shaped TPA wings into the distorted triangular structure appears to cause serious distortion of all phenyl rings in the molecule, consequently weakening π–π stacking interactions. For this reason, it appears that small and thin petal-like aggregates are formed preferentially.

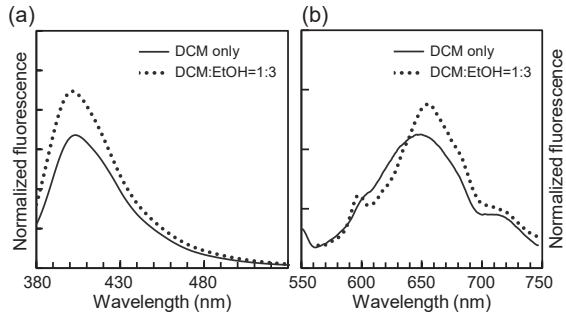

Fig. 4. Fluorescence spectra when excited at (a) 360 nm and (b) 510 nm.

When excited with UV (340-360 nm) and green (510 nm) light (Figs 2b and 4), 3PhA in organic (THF and DCM) solutions showed two fluorescence bands at ~380-400 nm and ≥650 nm, respectively. The two bands may be due to TPA being linked to the central ring structure via a diethylphenyl group and keto-hydrazone form [21-23], respectively.

Notably, regardless of the solvent nature, the assembly into micrometer-sized flat petal-like aggregates rarely resulted in a reduction in fluorescence intensity, but rather increased it slightly. The red fluorescence from a bunch of petals was thus confirmed with FOM (Fig. 5). The fluorescence quantum yield was found to be ~10^{-3}. The restriction of free intramolecular rotation in the sterically crowded 3PhA molecule is likely responsible for maintaining fluorescence intensity even after the formation of aggregates.

4. Conclusion

We designed a highly distorted triangular chromophore with three nonplanar TPA wings being connected to the central ring structure via a phenyl ring. The triangular molecule have a tendency to assemble into fluorescent petal-like structures rather than long fibers. Compared to the corresponding solution, the assembly did not significantly change the maximum absorption bands and fluorescence properties. That is, the introduction of three TPA wings leads to serious distortion of all phenyl rings in the molecule, resulting in weakening of free intramolecular rotation and π–π stacking interactions. These results

may provide an efficient way to produce various fluorescent nano- and microstructures.

Acknowledgements

This work was supported by grants from the National Research Foundation (NRF) of Korea (2018R1A2B6009315) and the framework of bilateral international cooperation program managed by the NRF Japan Society for the Promotion of Science (2018K2A9A2A08000191). We are grateful to Mr Yeong-Jun Lee (Department of Chemistry Education, KNU) for his assistance with FE-SEM measurements.

References

1. S. Babu, K. Kartha, and A. Ajayaghosh, *J. Phys. Chem. Lett*., **1** (2010) 3413.
2. Y. Hong, J. W. Y. Lam, and B. Z. Tang, *Chem. Soc. Rev*., **40** (2011) 5361.
3. B. An, J. Gierschner, and S. Y. Park, *Acc. Chem. Res*., **45** (2012) 544.
4. Y. Sagara and T. Kato, *Angew. Chem. Int. Ed*., **50** (2011) 9128.
5. Z. Chi, X. Zhang, B. Xu, X. Zhou, C. Ma, Y. Zhang, S. Liu, and J. Xu, *Chem. Soc. Rev*., **41** (2012) 3878.
6. P. Gopikrishna, N. Meher, and P. K. Iyer, *ACS Appl. Mater. Interfaces*, **10** (2018) 12081.
7. G. Huang, Y. Jiang, S. Yang, B. S. Li, and B. Z. Tang, *Adv. Mater*., **29** (2019) 1900516.
8. R. Kumar, H. Aggarwal, and A. Srivastava, *Chem. Eur. J*., **26** (2020) 10653.
9. Y. Sagara, T. Mutai, I. Yoshikawa, and K. Araki, *J. Am. Chem. Soc*., **129** (2007) 1520.
10. T. Kato and Y. Sagara, *Nat. Chem*., **1** (2009) 605.
11. S.-J. Yoon, J. Chung, J. Gierschner, K. Kim, M. Choi, D. Kim, and S. Y. Park, *J. Am. Chem. Soc*., **132** (2010) 13675.
12. Y. Q. Dong, J. W. Y. Lam, and B. Z. Tang, *J. Phys. Chem. Lett*., **6** (2015) 3429.
13. S. Ito, T. Yamada, T. Taguchi, Y. Yamaguchi, and M. Asami, *Chem. Asian J*., **11** (2016) 1963.
14. W. Yang, C. Liu, S. Lu, J. Du, Q. Gao, R. Zhang, Y. Liu, and C.Yang, *Chemistry Select*, **2** (2017) 9215.
15. Photoreactive Organic Thin Films, ed. Z. Sekkat and W. Knoll, Academic Press, Elsevier Science (2002).
16. H. Rau, *Angew. Chem. Int. Ed. Engl*., **12** (1973) 224.
17. C. G. Morgante and W. S. Struve, *Chem. Phys. Lett*., **68** (1979) 267.
18. J. Azuma, N. Tamai, A. Shishido, and T. Ikeda, *Chem. Phys. Lett*., **288** (1998) 77.
19. Y. Shirota, K. Moriwaki, S. Yoshikawa, T. Ujike, and H. Nakano, *J. Mater. Chem*. **8** (1998) 2579.
20. K. Kreger, M. Bäte, C. Neuber, H.-W. Schmidt, and P. Strohriegl, *Adv. Funct. Mater*., **17** (2007) 3456.
21. G. Gabor, Y. Frei, D. Gegiou, M. Kaganowich, and E. Fisher, *Isr. J. Chem*., **5** (1967) 193.
22. H. Rau, *Ber. Bunsen-Ges. Phys. Chem*., **72** (1968) 1068.
23. L. Racané, Z. Mihalić, H. Cerić, J. Popović, and V. Tralić-Kulenović, *Dyes Pigm*., **96** (2013) 672.
24. M. Han, S. J. Cho, Y. Norikane, M. Shimizu, and T. Seki, *Chem. Eur. J*., **22**, (2016) 3971.
25. I. Abe, M. Hara, T. Seki, S. J. Cho, M. Shimizu, K. Matsuura, H. Cheong, J. Y. Kim, J. Oh, J. Jung, and M. Han, *J. Mater. Chem. C*, **7** (2019) 2276.
26. M. Han and K. Ichimura, *Macromolecules*, **34** (2001) 90.
27. C. A. Hunter, K. R. Lawson, J. Perkins, and C. J. Urch, *J. Chem. Soc. Perkin Trans. 2*, (2001) 651.
28. J. P. Hill, W. Jin, A. Kosaka, T. Fukushima, H. Ichihara, T. Shimomura, K. Ito, T. Hashizume, N. Ishii, and T. Aida, *Science*, **304** (2004) 1481.

JOURNAL OF PHOTOPOLYMER SCIENCE AND TECHNOLOGY
Volume 34, Number 4, 2021